Oligodimethylsiloxanes with Charged Chain Ends:

Synthesis, Characterization, and Properties

A Dissertation Presented for the

Doctor of Philosophy

Degree

The University of Tennessee, Knoxville

Tianyu Li

May 2022

ACKNOWLEDGEMENTS

First and foremost, I gratefully thank my advisor, Prof. Kunlun Hong, for his support, kindness, mentorship, and encouragement in every aspect from research to life. When my previous advisor left the University of Tennessee, Dr. Kunlun Hong provided me the opportunity to continue my research. It is my great fortune to be his first Ph.D. student. As a sincere friend and excellent scientist, I learned a lot from him, including but not limited to his patience, attitude to life and science, and wisdom in interpersonal skills.

I would like to thank all my committee members: Prof. Bamin Khomami, Prof. Takeshi Egami, and Prof. Kevin M. Kit, for their time, guidance, help, and valuable suggestions, especially for presenting a coherent story in the dissertation.

I also thank my collaborators, BoKai Wang, Dr. Yu-Xian Lin, Dr. C.-H. Lin, and Prof. Hsin-Lung Chen, for their help on characterizations with SAXS, and Prof. Masashi Osa for viscosity data analysis.

I present my thanks to Dr. Yangyang Wang for instrument training, liquid nitrogen refilling, and advice on data analysis, Dr. Peter Bonnesen for discussions of NMR spectra and many other logistics help especially ordering of chemicals, Dr. Jihua Chen for TEM imaging, and Dr. Mark A Arnould for MALDI-TOF MS experiments, data analysis, and proofreading of this dissertation. Also, I would like to thank Dr. Lin Lu, Dr. Benjamin L Doughty, and Dr. Charles Patrick P Collier for training and guidance in SFG experiments. Dr. Hui Li guided me on star polymer synthesis and DLS measurements, as well as my life. Wish everything is going well in his new career.

I am also lucky to work with many talented and helpful students, post-docs, and staff at the University of Tennessee and Oak Ridge National Laboratory. With their patient helps, I can work smoothly and efficiently. I would like to thank Dr. Wei-Ren Chen and Dr. Changwoo Do for

discussions on small-angle neutron scattering, Dr. Wei Lu for GPC training, Dr. Yingdong Luo for suggestions on synthesis, Dr. Lengwan Li for helps in experiments and daily life, Dr. Caili Huang and Dr. Huiqun Wang for the teaching of glass blowing used in anionic polymerizations, Polyxeni P. Angelopoulou for help in the synthesis of polystyrene precursors, and Zhiqiang Cao for discussions and collaborations. Before I joined the research group of Prof. Kunlun Hong, lab members in the previous group, Dr. Jinbo Dou and Dr. Hui Zou, encouraged me a lot during the hard time when we had no advisor. I wish them the best of success in their careers. I am truly thankful that CNMS managers (Dr. Karren L More, Dr. Hans M Christen, Dr. Bobby G Sumpter, Dr. Scott T Retterer, Dr. Rigoberto Advincula) for their supporting.

I must also thank my friends: Mengqian Luo, Qi Zhang, and Ruifu Wang. Although we cannot meet conveniently because of distances between countries, their support never changes. I hope Mengqian finishes her Ph.D. study successfully and wish Qi and Ruifu all the best in their works.

Finally, I would like to thank my family for their love and sacrifices, which make today possible. My father, Ning Li, and my mother, Donglian Qin, encouraged and supported me to pursue my dream with their best efforts. Before sharing my happiness of success, my father and grandmother passed away after I came to UTK. To my father and grandmother, may they rest in peace. Thanks to my family members for taking care of my mother, and I wish my mother good health and happiness. Especially, I would like to thank my girlfriend, Xinyi Wang, for her years of accompanying and care. Thank her for being there for me no matter what happened.

ABSTRACT

Charged polymers have been intensively studied because of their scientific and industrial importance. In certain cases, a single charged group in the chain end can alter the structure and properties of a polymer dramatically. On the other hand, oligomers, which are different from both discrete small molecules and higher molecular weight polymers, have become an emergent class of materials. There are several charged chain-end functionalized oligomers reported, but this area has been largely unexplored. The work described in this dissertation is aimed at using well-characterized end-group functionalized oligodimethylsiloxane (oDMS) as model materials to understand the effects of charged end groups on the structural organization of amphiphilic oligomers in bulk and across the interface, which aides in designing novel amphiphilic materials with desirable properties for certain applications, such as the mimicked lipidic memcapacitor for neuromorphic computing.

The first part of this work focuses on the synthesis of chain-end functionalized oDMS. Mono-ionic/zwitterionic chain ends were introduced from the hydroxyl terminal groups of oDMS. Cations and anions influenced their thermal degradation temperatures (T_d) of the resultant products with most chain ends increasing the T_ds, except morpholinium bromide, which decreased.

The second part includes the phase behavior of amphiphilic oDMS. These oligomers self-assembled into well-defined morphologies including lamella and hexagonally packed cylinders as revealed by small-angle x-ray scattering measurements. The domain spacings ranged from 6.04 to 8.34 nm with different order-disorder transition temperatures. To further understand the phase behaviors during the heating/cooling processes, ion conductivities were measured by dielectric spectroscopy and the data shows that increased conductivity suggests a more strongly connected domain.

The third part studies the molecular organization of amphiphilic oDMS on oil/aqueous interfaces using sum frequency generation (SFG) spectroscopy. SFG revealed that charged chain ends significantly impact the orientation of the hydrophobic oDMS tails in hexadecane/aqueous interfaces. Moreover, by spectral fitting, the changes of the oDMS conformations at the interface can be elucidated.

Finally, we also offer a summary and an outlook in this exciting area.

TABLE OF CONTENTS

LIST OF TABLES

LIST OF FIGURES

LIST OF SCHEMES

CHAPTER 1 INTRODUCTION TO OLIGOMERS WITH CHARGED CHAIN ENDS

1.1 The Unique Features and Applications of Oligomers with Ionic Liquids as Chain Ends

With the growing demand for the replacement of hazardous solvents in both industry and academia, salts in liquid forms emerged as extensions to the available solvents for synthetic chemistry. However, instead of using molten salts as solvents heated to hundreds of degrees, ionic liquids (IL), organic salts entirely formed by ions with freezing points below 100 ˚C, were developed and widely used in research laboratories or industry.[1] In 1914, Walden and coworkers reported ethylammonium nitrate (melting point of 12 ˚C) as the first room-temperature ionic liquid.[2] After almost one century, as the enrichment of chemical diversity for ILs, numerous cations and anions were combined to yield ILs with diverse characteristics broadening their applications. Furthermore, with the combination of organic and polymer chemistry, new ILs with unique and attractive properties were developed. Based on their molecular weights and the chemical positions of the ionic groups, three categories have been developed: (1) Molecular ionic liquid. (2) Polymeric ionic liquids. (3) Oligomeric ionic liquids. Examples of each category are shown in Figure 1.1.

1.1.1 Molecular Ionic Liquids

As mentioned above, molecular ionic liquids are formed entirely by large ions. They have high thermal stability with a workable viscosity (< 100 cP) and a good specific conductivity (< 10 mS/cm).[3] When used as solvent, ILs are better than common organic solvents in several ways: (1) both organic and inorganic compounds can be dissolved in ILs, which are in one phase. (2) ILs are highly polar solvents that are non-coordinating due to the poor coordination ability of ions. (3) Some organic solvents are immiscible with ILs, and ILs can replace the aqueous phase in a two-phase system as the polar alternative. (4) The Vapor pressure of ILs is negligible and can be applied in high-vacuum systems.[4] Not only a pure solvent but also a good solvent for catalysis, several ILs

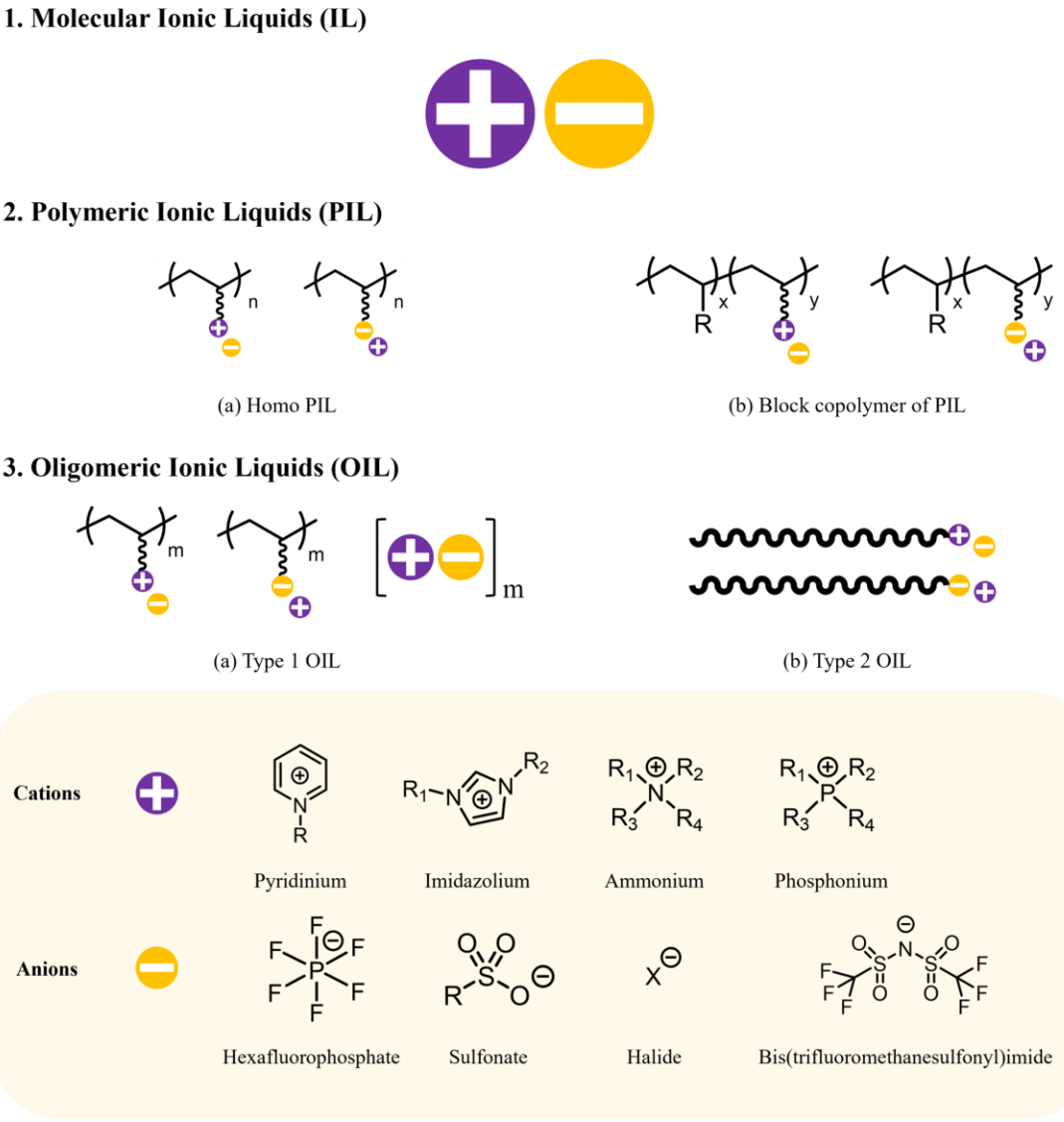

Figure 1.1 Structures of molecular ionic liquids, polymeric ionic liquids, and oligomeric ionic liquids.

were found to give high regioselectivity of O-alkylation reaction for sodium 2-naphthoxide.[5] Furthermore, some cations/anions on ILs are useful pharmaceutical ions, and ILs may be more easily administered to patients due to their liquid form. Finally, mixtures of ILs with long alkyl-chain cations can be used as lubricants.[6] These very diverse applications are closely related to the structures of ILs, including the bulk structure and the structure of the solid-ionic liquid interface. Atkin and coworkers have extensively reviewed the relationship between the structure and nanostructures of ILs.[7] The structure-property relationship of polymeric ionic liquids and oligomeric ionic liquids is discussed in the following sections.

1.1.2 Polymeric Ionic Liquids

Polymeric ionic liquids (PILs) have ionic pendant groups on each repeat unit connecting with the polymeric backbone. The incorporation of ILs into polymers expands the families and applications of polyelectrolytes. Compared with polyelectrolytes or charged polymers, which typically contain inorganic salts, ion pairs of PILs are weaker leading to a reduced intermolecular interaction between PILs. Thus, ionic groups of PILs have less influence on the properties of polymers than these of polyelectrolytes or charged polymers consisting of inorganic salts. In terms of corresponding ILs, the ionic conductivity of PILs is significantly decreased because of the reduced ion mobility.[8]

One unique feature of PILs and their block copolymers is their microphase separation behaviors. PILs and PIL block copolymers can provide an ideal well-defined model system. For typical block copolymers, a library of block copolymers with similar compositions but different molecular weight for each block is needed to change their domain sizes. By simply changing anions, Garcia and coworkers were able to tune the domain sizes of charged poly(styrene-b-2-vinylpyridine) (PS-b-P2VP) from 34 to 73 nm within the same morphology (Figure 1.2).[9] For IL

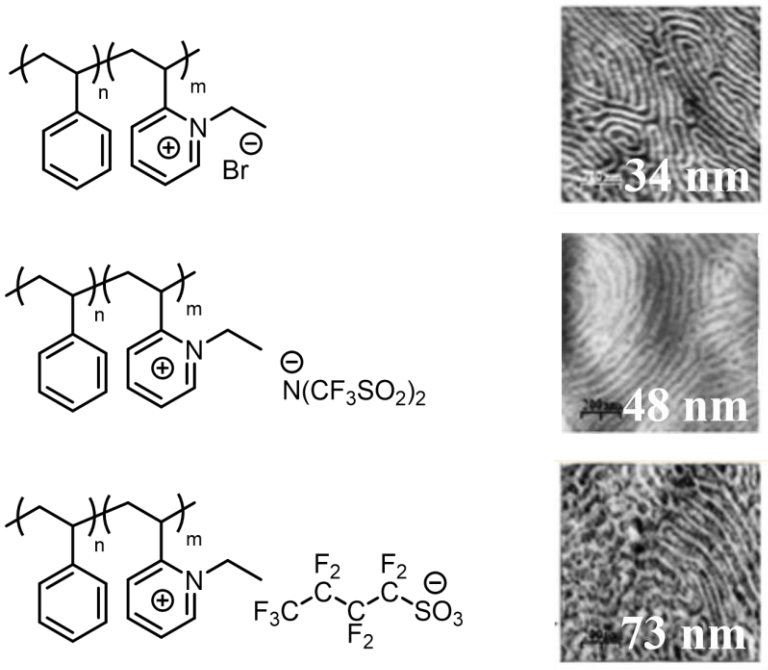

Figure 1.2 Tuning of domain spacings with anion exchange. Adapted with permission from Reference [9]. Copyright 2011 American Chemical Society.

homopolymers, phase separation can also be achieved due to the incompatibility between hydrophobic polymer and hydrophilic charged groups. Yuan and coworkers synthesized poly(3-*n*-dodecyl-1-vinylimidazolium bromide) with different lengths of *n*-alkyl chains (*n* = 11, 13, 15, and 17), and these IL homopolymers were able to form prepared onion-like vesicles with multilamellar morphology in water and shown in Figure 1.3.[10] Other applications of PILs include thermoresponsive materials with the lower and upper critical solution temperature-type phase transitions and carbon dioxide capture/separation.[11-14]

1.1.3 Oligomeric Ionic Liquids

Oligomeric ionic liquids (OILs), which engage an intermediate position between molecular and polymeric analogs of ionic liquids, exhibit combined properties of both ionic liquids and oligomers. There are two kinds of oligomeric ionic liquids (OILs): the first one (named as type 1 OIL in this dissertation) has the same structures as PILs, while the molecular weights of these OILs are lower, typically below 1500 g/mol. Type 1 OILs are applied in specific applications, which require a liquid state. For example, Iwasa, Aida, and coworkers developed hexafluorophosphate salts of imidazolium ion tetramer as the new class of electrolytes for electric double layer capacitors.[15] Another type of OILs (named as type 2 OIL in this dissertation) are oligomers that have ionic groups at the chain ends. Compared with PILs, which are often solids below 100 ˚C, OILs can exist in a liquid state or gel state due to the nature of oligomers.[16] Like ILs and PILS, OILs can also serve as the reaction medium for synthesis and catalysis.[17, 18]

For type 2 OILs, the number of ionic groups on type 2 OILs are less than that of ILs, PILs, and type 1 OILs. However, type 2 OILs can still exhibit the similar properties to ILs. Furthermore, like polymers, where a significant chain-end effect on their properties has been found in certain cases, the properties of type 2 OILs can also be tuned by the single chain end, which will be

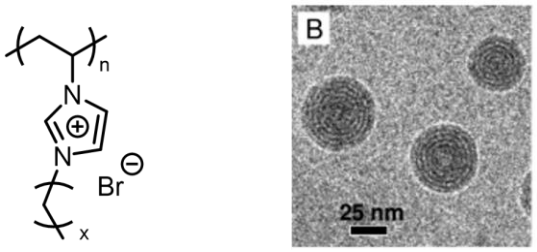

Figure 1.3 Phase separation of homo PIL. Adapted with permission from Reference [10]. Copyright 2011 American Chemical Society.

discussed more in Section 1.3. Furthermore, by the combination of incompatible oligomer chains and end groups, the self-assembly behavior of the amphiphilic oligomers makes the materials potential candidates for lipid-based memcapacitor for neuromorphic computing, which will be discussed in the following section 1.3.3. It was the exciting features and potential applications that motivated us focused this work on type 2 OILs instead of type 1.

1.2 The Nature-Inspired Materials: Oligomers with Zwitterionic Chain Ends

Although there have been intensive studies of ILs, there are only limited reports of ILs produced in nature. In 2014, Davis Jr and coworkers found an IL formed when ants S. invicta confronted N. fulva. To detoxify the alkaloid-based S. invicta venom, N. fulva groomed it with its own formic acid venom. The mixture formed the amino formic acid-base IL with long alkyl chains, which was explained in Figure 1.4, and it has a similar structure as a type 2 OILs.[19] Unlike ILs, zwitterionic liquid (ZL) or zwitterions have been found widely in nature.

1.2.1 Zwitterionic Biomolecules: Lipids

Zwitterions are molecules that contain functional groups with equal numbers of positive and negative charges. Different from ILs, whose ions are separated, ions of ZLs are bonded covalently, illustrated in Figure 1.5.[20] The noteworthy difference in structure incurs their characteristically different properties. From an environmental aspect, ZLs are less ecotoxic than ionic analogs.[21] Nature offers a variety of ZLs. One example is the lipids in cell membranes which are critical to a variety of biological activities. The structures of lipids, shown in Figure 1.6, usually contain a long hydrophobic alkyl tail and a hydrophilic zwitterionic head, which is similar to the structure of type 2 OILs.

1.2.2 Oligomeric Zwitterionic Liquids

Here oligomeric zwitterionic liquids are defined as the oligomers with zwitterionic chain

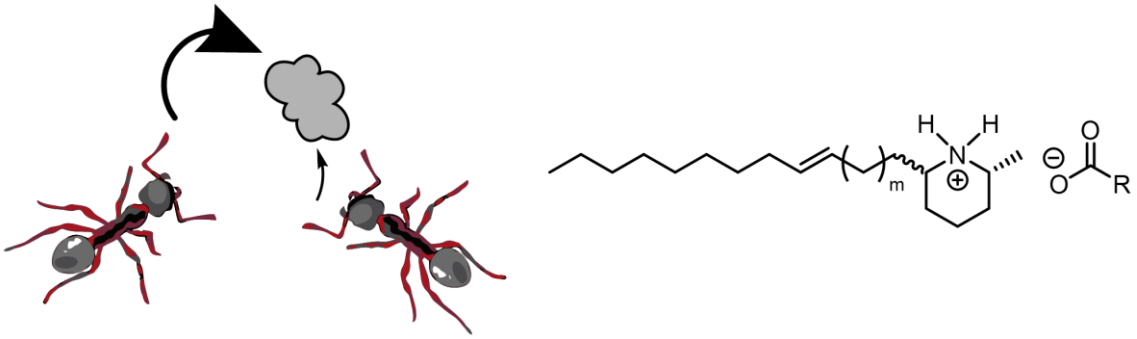

Figure 1.4 Nature produced OIL.

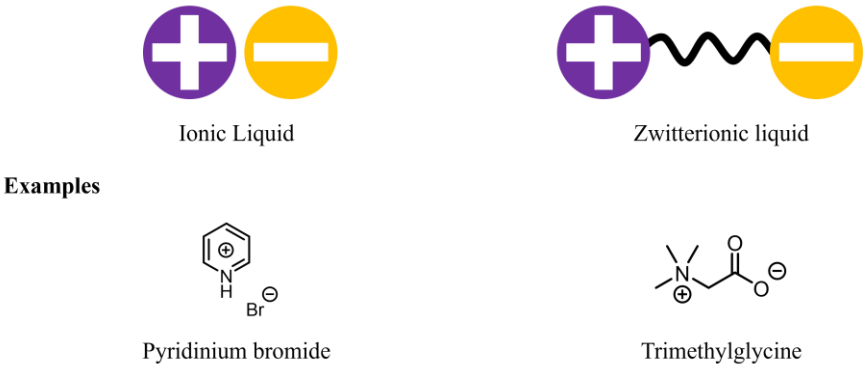

Figure 1.5 Comparison of IL or ZL.

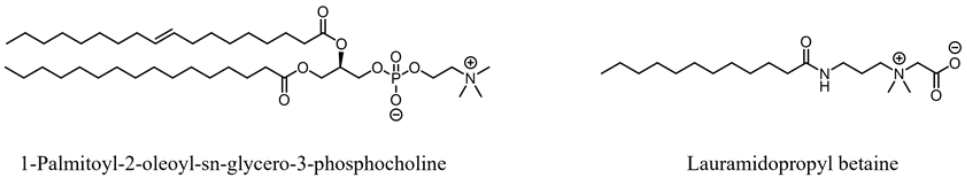

Figure 1.6 Structures of lipids.

ends as compared to oligomers with ionic end groups. A cursory review of the literature reveals that most papers focus on OZLs in the area of biomaterials and antifouling materials.[22, 23] Hadjichristidis and coworkers developed polystyrene-b-polyisoprene (PS-b-PI) block copolymers with one zwitterionic chain end and the triblock copolymer of polystyrene and polyisoprene (PI-b-PS-b-PI) with both end groups modified as zwitterions. With the introduction of zwitterionic end groups, mono-functionalized block copolymers were found to be aggregated in carbon tetrachloride, which is a good solvent for both polystyrene and polyisoprene. Furthermore, the difunctionalized triblock copolymer formed a gel below critical overlap concentration.[24] The zwitterionic chain ends significantly affected the properties of polymers, and they were expected to play a more critical role in OZLs because the lower molecular weights, the higher number of functionalized chain ends per mole.

1.3 End-group Effects on Properties of Oligomeric Ionic and Zwitterionic Liquids

Chain end is a critical structural parameter of polymers and oligomers that dominates their properties, including thermal properties, conformational properties, self-assembly behavior, surface properties, ion transportation properties, and phase transition behaviors.[25-29] For ILs and ZLs, the charged functionalities changed the original properties of unfunctionalized materials. Based on the applications of ILs and ZLs, the following properties were discussed in this work: (1) thermal properties, which result in different physical states of ILs, such as room or low temperature ILs for specific tasks. (2) Phase separation behavior. The charged chain ends induced nanostructures in bulk make themselves potential candidates for the next generation of nanopatterning, lubricants, and antiwear materials.[30] (3) Ion conductivity because of the application of polyelectrolytes. (4) Molecular organization at interfaces. Inspired by the natural lipids, the hydrophilic charged ends with designed hydrophobic chains mimic the amphiphilic

nature of lipids to form membranes at interfaces, which is a powerful model for the study of medium transfer between interfaces and charge transfer and is the potential lipid-based memcapacitor for neuromorphic computing.[31, 32]

1.3.1 Thermal Properties

The various combinations of cations and anions offer different thermal properties. For ILs, thermal stability (thermal degradation temperature, T_d) and melting points (T_m) are the key points to applications. After the introduction of polymers and oligomers into ILs, glass transition temperature (T_g) is also included.

Brennecke and coworkers studied the thermal stability of imidazolium-based and pyridinium ILs. For the counterions of imidazolium with n-alkyl chains, the thermal stability followed the order of bis(trifluoromethanesulfonyl)imide (Tf_2N) > tris(trifluoromethanesulfonyl)methide (methide) > triflate > tetrafluoroborate (BF_4) > dicyanamide (DCA) > bromide (Br). In terms of pyridinium type cations, the counterions followed the order of bis(trifluoromethanesulfonyl)imide (Tf_2N) > tetrafluoroborate (BF_4) > bromide (Br). They concluded that cations had a small effect on T_d, while anions primarily dominated $T_{d,}$ which was dedicated by their coordination ability and size. However, this conclusion for cations needs more studies because the studied cations were different only in positions and lengths of alkyl chains, while the chemical properties of cations were still similar.[33, 34] Furthermore, the effect of anions and cations of charged chain ends on the thermal properties of OILs and OZLs is still not clear.

For T_g, Meng and coworkers developed a library of star-shaped ionic liquids with different anions, where 2,2′-bis((isonicotinoyloxy)methyl)propane-1,3-diyl diisonicotinate (IPD) and cyclohexane-1,4-diyl diisonicotinate (HI) were the core and arm, separately. Core and arm were connected by *n*-alkyl dibromides (n = 4 and 10), and the charged groups are at the terminals of the

4-arm stars. T_gs of these ionic stars were closed but shown the order of Br > BF_4 > dodecylbenzenesulphonate (A-SO_3) > (+)-10-camphorsulphonate (D-SO_3).[35] If the ILs based materials were liquid crystals, they would have a T_m.

1.3.2 Phase Separation Behavior and Ionic Conductivity

Chain end was a powerful tool to tune many properties in polymers and oligomers. Park and coworkers synthesized the block copolymer of polystyrene and poly(ethylene glycol) (PS-b-PEG), which showed a relatively poorly defined morphology. After the hydroxyl chain ends of PS-b-PEG were converted to sulfonate end groups then charged chain ends, the morphology was changed from well-defined lamellar to hexagonal cylindrical phases. Furthermore, compared with hydroxyl-terminated PS-b-PEG, ion conductivity was doubled for sulfonate-terminated PS-b-PEG. Their work has demonstrated that a single chain end modification may be enough to tune the morphology and conductivity of polymer electrolytes, as illustrated in Figure 1.7.[36]

For OILs, Meng and coworkers prepared the low molecular weight star ionic liquids described in section 1.3.1. Their morphology and ion conductivity were able to be tuned by changing of different anions, which was explained in Figure 1.8. Morphologies were changed from lamellar to bicontinuous cubic to hexagonal columnar phase with the exchange of anions from Br to A-SO_3 to D-SO_3. Furthermore, the ion conductivity of anions followed the order of A-SO_3 > D-SO_3 > BF_4 > Br.[35] However, the effect of cations on the morphology and ion conductivity is unknown (also, the alkyl chain was pretty short).

In terms of zwitterions, Xu and coworkers synthesized a triblock copolymer of poly(butyl methacrylate) with POSS pendant groups, poly(2-diethylaminoethyl methacrylate), and poly(3-dimethyl(methacryloyloxyethyl) ammonium propanesulfonate) which formed nano micelles in water.[26] Currently, there is no report based on oligomers with zwitterionic chain ends for phase

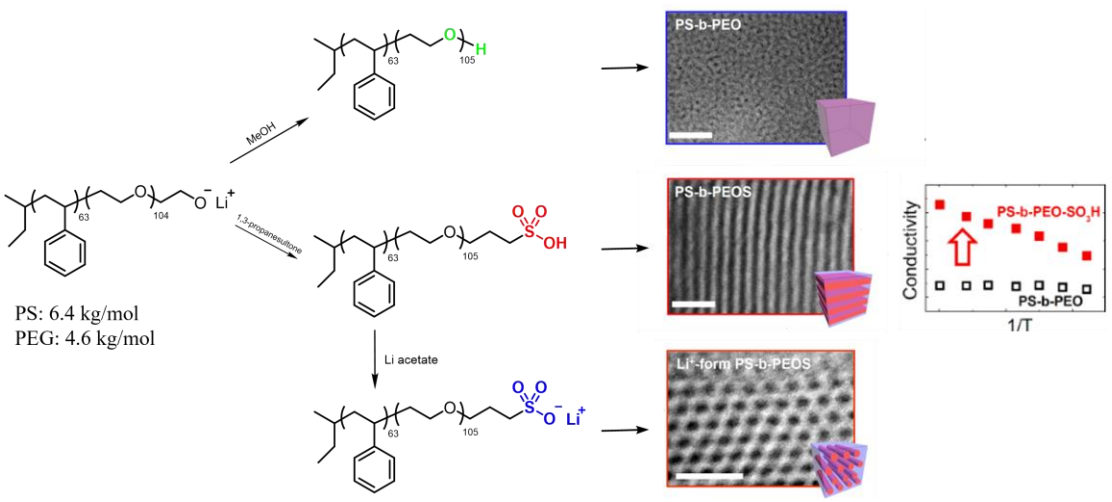

Figure 1.7 Tuning of morphology and conductivity with the introduction of charged chain ends. Adapted with permission from Reference [36]. Copyright 2013 American Chemical Society.

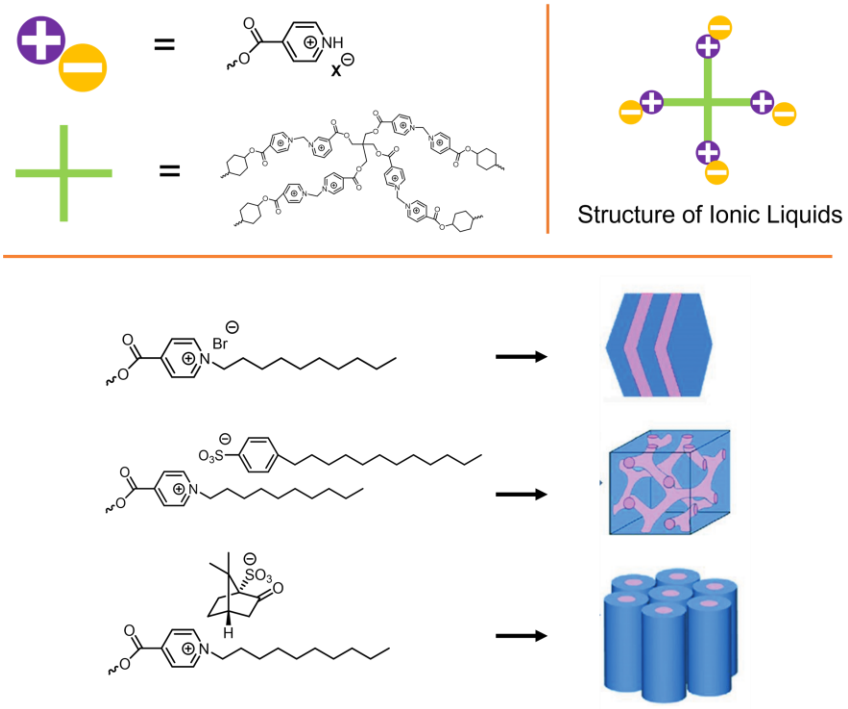

Figure 1.8 Tuning of morphology and conductivity of OIL by changing of anions. Adapted with permission from Reference [35]. Copyright 2021 Taylor & Francis.

separation behaviors in bulk. Different phase behaviors are expected to the ionic and zwitterionic chain ends because the connection of zwitterions limited the movement of ions compared with ion liquids.

1.3.3 Molecular Organization at Interfaces

Liquid/Liquid interfaces are omnipresent in our daily life and play significant roles in many fields, including ion exchange, separation and extraction, electrochemical processes, assembly of nanoparticles, phase-transfer catalysis, and biological activities.[32, 37-40] In a dynamic environment, the interface formed by two immiscible liquids, such as oil and aqueous solution, provided the inherent asymmetry of the chemical and physical circumstance.[41] Different from single-phase bulk media, this unique asymmetry feature was able to drive the ordering and assembly of functional supramolecular components.[42, 43] For example, droplet interface bilayers (DIBs), which are used in studies of membrane proteins and as platforms for functional devices, formed between two or more aqueous droplets coated with monolayers in the oil phase, which is shown in Figure 1.9.[44] One of the most famous examples of DIBs is phospholipid bilayer membranes. As the foundation of all biomembranes, phospholipid bilayer membranes play a central role in both activities of cells and model membranes mimicking the living biosystem to sense and respond to the signals. However, phospholipid bilayer membranes are weak and fragile, which limits the extension of their applications, especially in the case of biomolecular memristors to form large enough neuromorphic networks.[31]

To obtain stable DIBs with similar sizes and functionalities, our group has developed a charged oligomer with hydrophobic oDMS and ionic liquid end group of methylimidazolium cation ($MIM^{(+)}$). For the anion of chloride ($Cl^{(-)}$), the amphiphilic oligomer formed bilayers at low ionic strength, while an external voltage was required to form bilayers at high ionic strength. The

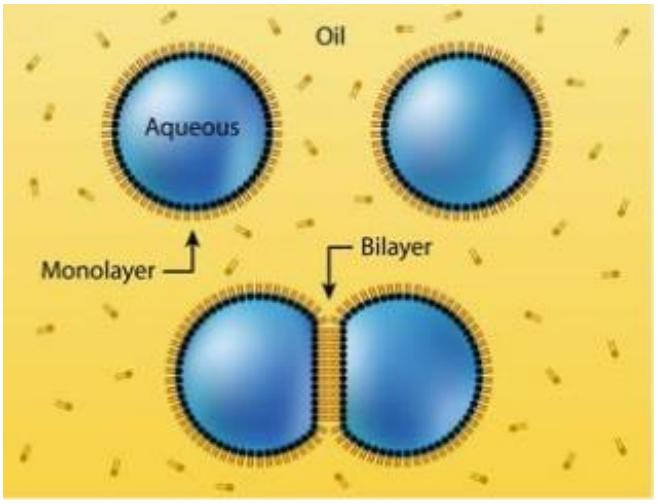

Figure 1.9 Droplet interface bilayers. Reprinted with permission from Reference [44]. Copyright 2013 European Biophysical Societies' Association (EBSA).

increased ion strength caused a stronger chain overlap which led to the increase of repulsive disjoining pressures. With applying the external voltage, the attractive electrocompressive stress was provided to overcome the repulsion, then forming the bilayers. Furthermore, the assembly process at high ionic strength was irreversible, which suggested that the formed membrane was more stable.[45] Based on effects of concentration of $Cl^{(-)}$ in our previous findings, the diverse conditions in neighboring bulk phases could tune the ability of interfaces and the assembly behavior. To further understand the intermolecular and interphase interactions at interfaces, we introduced different ions and ion-paring interactions into the same oDMS-$MIM^{(+)}$ system by changing the anions and their concentrations in aqueous phases, which manipulated the densities and structures of amphiphilic oligomer at the oil/aqueous interface. Figure 1.10 explains the oligomer structure at the interface with various anions and different concentrations. Figure 1.10 (a) shows the oDMS chains in dilute thiocyanate ($SCN^{(-)}$) aqueous solution, where ion pairs improved the packing of oDMS chains. Compared with $SCN^{(-)}$, $F^{(-)}$ was less interacted with $MIM^{(+}$ chain ends, which is illustrated in Figure 1.10 (b). Thus, a low concentration of $F^{(-)}$ does not greatly influence the properties of oligomers at the interface, which contained a lower density of oligomer chains, and their conformations were more parallel to the interface. When increasing the ion strength, even hard anions, such as $F^{(-)}$, would improve the packing of oDMS tails while they cannot be packed as densely as soft anions, like $SCN^{(-)}$, which are shown in Figure 1.10 (c) and (d).[46]

Based on our previous study, the ion pairs could mediate molecular organization across the oil/aqueous interface. However, the anions that were present were introduced from the external environments. As the natural of oDMS with charged chain ends, ion pairs always existed at the chain ends, although the concentrations of anions from chain ends are much less than the

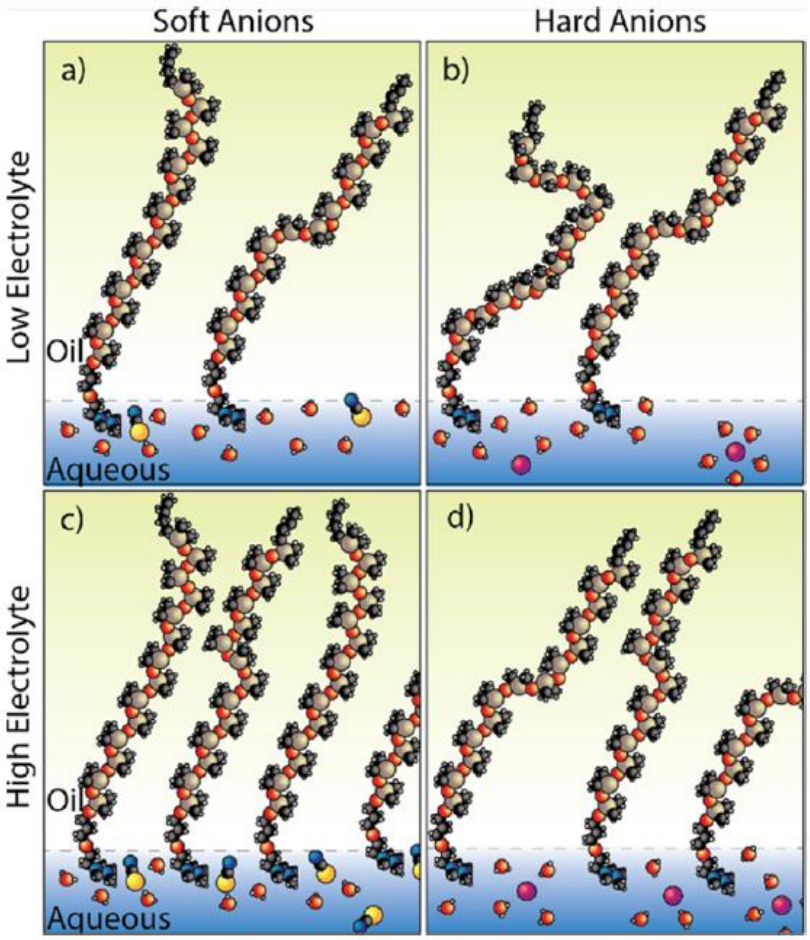

Figure 1.10 Structures of oDMS at oil/aqueous interface. Reprinted with permission from Reference [46]. Copyright 2021 American Chemical Society.

introduced external anions. The influence of these inherent ion pairs on the packing of oDMS chains is unknown. On the other hand, ion pairs are formed by both cations and anions. The characteristics of cations should also affect the properties of formed ion pairs. Thus, the effect of cations on the chain packing of oDMS needs to be explored. Moreover, compared with ion pairs, zwitterions are covalently bonded, which limits the pairing of external ions with the zwitterions. The packing of oDMS chains with zwitterionic and ionic chain ends is expected to be different but could offer new structural information, thus experiments are needed to confirm their packing density and conformation of oDMS chains at the oil/aqueous interface. This information is essential in guiding us to design mimicking lipid materials with desirable properties and stability.

1.4 Motivations

In this work, four objectives were focused to provide a symmetrical and fundamental understanding on the effects of charged chain ends on the critical properties of charged amphiphilic oligomers. The studied properties were closely related to their potential applications. Thus, a theoretical approach could be built based on this work to design and apply the materials for the next generations. Here are the four objectives:

1.4.1 Effects of Charged Chain Ends on Thermal Properties of Charged Amphiphilic Oligomers

As indispensable parameters for the design of laboratory measurement conditions and guidance of practical applications, the thermal properties of ILs were intensively studied. However, the effect of cations with different chemical natures on thermal properties was still far from clear for both ILs and OILs. Furthermore, both OILs and OZLs have charged chain ends but are distinct in the connection methods of ions. More efforts are needed to understand the influence of different connecting styles, including ion pairs and covalently bonded ions.

1.4.2 Impacts of Charged End Groups on Phase Separation Behavior and Ion Conductivity

Phase separation behavior and ion conductivity are important features for PILs and OILs. However, the effect of cations on these two properties of OILs has not been explored. The characteristics of ions can not only impact ion conductivities of OILs but also affect their structures. The stronger connected domains led to an increase in conductivity.[7] Cations/anions influenced the morphologies and degrees of the internal order by their characteristics, including coordination ability, size, charge density, electronegativity, and other possible parameters. Simultaneously, one or more of these parameters also affected the ion conductivity. It could be the situation that one cation or anion would suppress the degree of the internal order while improving their ion conductivity. To fully understand the effect of cations and anions on phase separation behavior and ion conductivity, a carefully designed system containing a library of samples was required, and it will be discussed in the following section 1.4.4.

1.4.3 Influences of Cations and Anions on Molecular Organization at Oil/Aqueous Interface

The ability of interfaces to respond to the changing of environments in their neighboring phases provides interfaces a diversity of functions and applications. As discussed in section 1.3.3, the effects of environmental changes on the properties of charged amphiphilic oligomers at interfaces have been studied. However, the influence of internal structure, including characteristics of cations/anions at chain ends and the ion connection methods, on the packing density and conformation at the oil/aqueous is still unknown. This work would fulfill this part.

1.4.4 System Design for The Objectives

Based on these scientific objectives, a system with the ability of phase separation to have morphologies and organization at the oil/aqueous interface is needed. Inspired by the natural lipids and high-χ block copolymers, amphiphilic oligomers are perfectly suitable for this mission. To

simplify the system, instead of using block co-oligomers, homo-oligomers are employed. Because of the hydrophilic chain ends, the hydrophobic oligomer chains are necessary. Among the hydrophobic oligomeric candidates, oDMS was selected in this study due to its unique properties: (1) Excellent hydrophobicity and incompatibility with charged chain ends. (2) Good solubility in organic solvents for synthesis and process. (3) Different chemical shifts in NMR spectra of backbones and chain ends made it convenient to monitor the progress of end group modification and confirm the final products. (4) A possible etch mask offers these products the potential applications in semiconductor industry such as nanopatterning.[47]

In summary, oDMS with various mono charged chain ends were developed in this work. The cations of end groups contained imidazolium, pyridinium, and morpholinium, which were different in nucleophilicities (*MMP* > *Py* > *MIM*) and basicity (*MMP* > *MIM* > *Py*) of corresponding amines.[48-50] For anions, mesylate, tosylate, triflate and bromide were used. The anions were distinct in several aspects: (1) size calculated according to group contribution theory: tosylate > triflate > mesylate > bromide.[51, 52] (2) Coordination ability towards transition metals and lanthanides: bromide > mesylate > triflate.[53] (3) Charge density: bromide > mesylate > triflate > tosylate. (4) Surface-inactive (triflate, tosylate, and mesylate) vs. surface-active anions (bromide). Furthermore, sulfobetaine and tertiary amino methanesulfonic acid were selected to compare the difference between zwitterionic and ionic chain ends. By tuning the combinations of ions and correlating them to achieved properties, the relationship between anions/cations/combinations of ions and properties was obtained.

1.5 Characterization Methods for Molecular Organization

This work focused on the molecular organization of oligomers with charged chain ends in bulk and across the interface. Different characterization methods were introduced in this section

with instructions on important experimental parameters, explanations of typical spectra, and analysis of data.

1.5.1 Phase Separation Behavior in Bulk

The incompatibility between blocks, pendant groups/chain ends, and backbones give polymers and oligomers the ability to phase separation and form micro- or even nano-scale features in bulk and thin films, with various morphologies, order-disorder transition temperatures (T_{ODT}), and domain spacings. Different advanced techniques have been applied to the obtained structures, including scattering and imaging methods.

For the scattering methods, one of the most widely used techniques is small-angle X-ray scattering (SAXS). Unlike imaging methods, which give a direct and detailed insight of morphology but from a small region of the sample, SAXS can offer an average over macroscopic materials with structural features in the range of 1 to 100 nm based on their electron density distribution.[54] Small-angle scattering means the small deviation (typically 0.1 to 5°) from the incident direction of radiations caused by the interaction between radiations and inhomogeneities of materials, which is illustrated in Figure 1.11. The irradiations can be x-rays, neutrons, gamma rays, electrons, and light.[55] Although small-angle neutron scattering were also used in characterized our samples, SAXS was mainly reported here because of the availability, convenience, and efficiency of the method,

The typical SAXS instruments can be sorted into two groups: (1) Point-collimation instruments. The beam will be shaped by pinholes in instruments to a small spot that illuminates the test sample. Thus, the weak scattering intensity is small, and a long measurement time from hours to days is required. (2) Lin-collimation instruments. The beam is confined in one dimension as a long narrow line. So, the scattering intensity is larger than that of point-collimation instruments,

Figure 1.11 Illustration of small-angle scattering.

leading to a shorter measurement time in the order of minutes to hours.[56]

The intensity $I(q)$ of SAXS can be expressed as the function of q, scattering vector, which obtained from photons with the wavelength of λ scattered off from the sample at the scattering angle of 2θ, shown in the following equation:

$$q = \frac{4\pi \sin\theta}{\lambda}$$

For calculation of amplitude and profile of scattering intensity, a function of the contrast of the scattering $\Delta\rho(\vec{r})$, which arises from different electron densities of materials in X-rays and various atomic nuclear structures of samples in neutrons, over the volume of a particle v_p is expressed. Here is the example of a spherical ball with a uniform scattering length density $\bar{\rho}$ and the radius of R. $\bar{\rho}$ can be calculated from coherent scattering length b_c of all atoms with the scattered volume v_p:

$$\bar{\rho} = \frac{\sum b_c}{v_p}$$

Then the shape function $F(q)$ can be expressed as:

$$F(q) = \int \Delta\rho(\vec{r})\ e^{i\vec{Q}\vec{r}} d\vec{r}^3 = \bar{\rho} \int e^{i\vec{Q}\vec{r}} d\vec{r}^3 = \bar{\rho} v_p$$

where $v_p = \frac{4\pi R^3}{3}$

Thus,

$$I(q) = |F(q)|^2$$

And based on the factorization theory, the scattering pattern of the system with the volume of V is

$$I_A(q) = \frac{|F(q)|^2}{V} = nP(q)S(q)$$

where $P(q)$ is form factor, which is typically normalized as $\tilde{P}(q) = \frac{P(q)}{P(q=0)}$; $S(q)$ is inter particle structure factor, and n is the number density of the spherical ball.[57]

$$I_A(q) = nP(q)S(q) = n\Delta\rho(\vec{r})^2 v^2 \tilde{P}(q)S(q)$$

With the obtained SAXS profile, the structural information can be extracted in three different regions, which were illustrated in Figure 1.12.[58] In the Guinier region, which is the low-q region where presents the overall dimension of the samples, fractals of scattered objects can be obtained with the power-law dependence between $P(q)$ and q: (1) Spherical object: $P(q) \propto q^0$. (2) Disk-like object: $P(q) = \frac{8V^2}{Q^2d^2} e^{-\frac{Q^2L^2}{12}} \approx \frac{8V^2}{Q^2d^2} \propto q^{-2}$, where L, d, and V are the thickness, diameter, and volume of objects, separately. (3) Rod-like object: $P(q) = \frac{\pi V^2}{qL} e^{-\frac{q^2d^2}{16}} \approx \frac{\pi V^2}{qL} \propto q^{-1}$. (4) Gaussian coil: $P(q) \approx \frac{8V^2}{Q^2R_g^2} \propto q^{-2}$, where R_g is the radius of gyration of polymers. Furthermore, Guinier analysis can be performed to approximate R_g of macromolecules by fitting the curve in the Guinier region ($qR_g \leq 1$) with the following equation:

$$InI(q) = InI_0(q) - \frac{1}{3}q^2R_g^2$$

Thus, the slope of the fitting line is $-\frac{1}{3}R_g^2$ and related to the size of macromolecules.

In high q region, named Porod region, the scattering is caused by interfaces instead of details of structures. The surface fractals can also be obtained from the power law of $I(q) \propto q^{-D}$. The slope D gives the roughness of the interfaces. $D = -4$ stands for a very smooth interface, while $-3 < D < -4$ shows a rough interface.[59]

Not only shape and size but also structural arrangement or randomness affect the scattering profile of SAXS, which is explained in Figure 1.13. Figure 1.13 (a), (b), and (c) presented three different orders of randomness: (a) Dilute Randomly located holes. In this system, holes with the

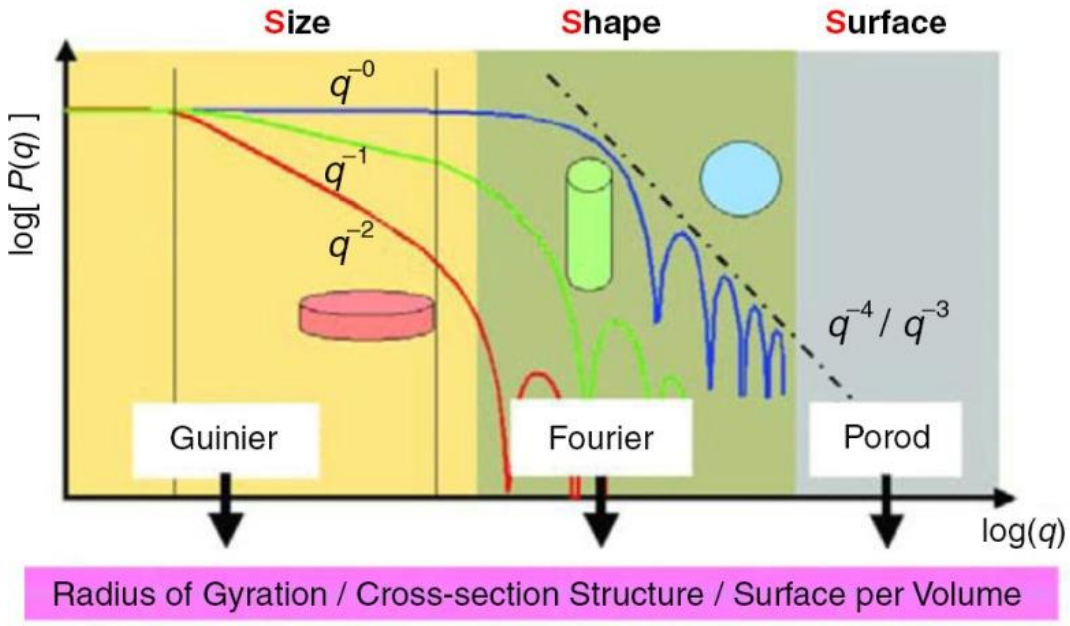

Figure 1.12 Guinier, Fourier, and Porod regions on SAXS profile and the corresponding structures. Reprinted with permission from Reference [58]. Copyright 2015 Taylor & Francis.

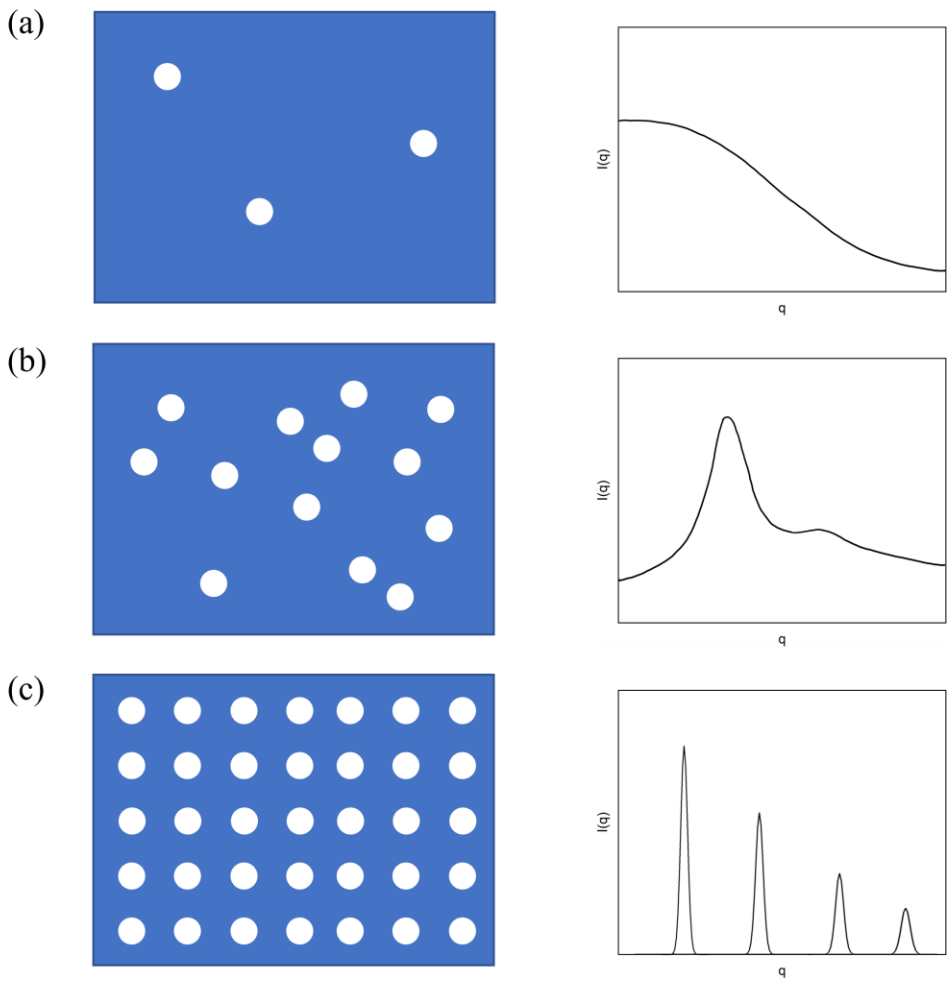

Figure 1.13 Schematic randomness of structures and corresponding scattering profiles. Reproduced with permission from Reference [60]. Copyright 2016 Springer Nature.

number of N are far from each other. Thus, $S(q) = 1$ and $I_A(q) = nP(q) = NP(q)$. The positions of holes are uncorrelated. (b) Holes with spatial correlation in short range. Holes can interfere with others, and then $S(q)$ is not equal to 1 at low q and tends to be 1 at high q, giving $I_A(q) = nP(q)S(q)$. Compared with SAXS profile of (a), (b) has a peak at low q and tends to be the same at high q. (c) Holes with the periodical arrangement. $S(q)$ is formed by narrow peaks at well-defined angles, which correspond to the geometry of hole arrangement.[60] Thus, SAXS can be applied to extract the ordered structure formed during phase separation according to the location of peaks.

In general, for the SAXS profile of samples with ordered structures, narrow peaks show a long-range order and/or a good resolution, and the intensity of peaks is proportional to the degree of order. Relative peak positions give symmetry of the structure. For example, lamellar morphology shows a relative peak position of $q_1 : q_2 : q_3 : q_4 = 1 : 2 : 3 : 4$ and hexagonal morphology is $q_1 : q_2 : q_3 : q_4 = 1 : \sqrt{3} : \sqrt{4} : \sqrt{7}$.

Furthermore, the domain spacing (d) can be calculated from the position of 1st order peak (q^*) as[61]

$$d = \frac{2\pi}{q^*}$$

In terms of imaging approaches, transmission electron microscopy (TEM), scanning electron microscope (SEM), and atomic force microscopy (AFM) are often applied to image the obtained morphology. Although imaging approaches offer a direct view of morphography, SAXS was preferred in this work because the chain ends were too small compared with oDMS chains to provide enough contrast for imaging. Element mapping may give a similar insight as imaging, but this can be done in the future.

Besides morphology and domain spacing, T_{ODT} can analyze with SAXS with temperature control. During the heating or cooling process, T_{ODT} can be determined by the disappearance or appearance of specific scattering peaks.

1.5.2 The Macroscopic Ion Conductivity

Ion conductivity, similar to electronic conductivity, is the movement of ions in response to the electric field.[62] Ion conductivity of ILs is usually measured by electrochemical impedance spectroscopy, broadband dielectric spectroscopy, and different types of cells, such as comb-shaped gold electrodes, gold plates, and indium tin oxide electrodes.[63-65] In this work, broadband dielectric spectroscopy was selected due to the access of instruments.

Broadband dielectric spectroscopy, as one of the impedance spectroscopies, describes the dielectric properties of samples subjected to an applied electric field as a function of frequency. It studies the interaction between the electric dipole moment of materials and the external electric field, which is expressed as static dielectric permittivity (ε). Other important parameters, such as DC electrical conductivity (σ) and dielectric constant (ε'), are also provided.

Permittivity (ε) contains a real part, which is ε' or dielectric constant, and imaginary part, which is ε'. They can be expressed as:

$$\varepsilon = \varepsilon' + i\varepsilon''$$

$$\varepsilon' = \frac{C_P d}{\varepsilon_0 A} \text{ and } \tan\delta = \frac{\varepsilon''}{\varepsilon'} = \frac{1}{R_P C_P \omega}$$

where ε_0, d, A, and ω are the vacuum permittivity, sample thickness, electrode area, and angular frequency, separately. C_P and R_P are capacitance and resistance. $\tan\delta$ is named as loss factor.[66]

With the applied electric field, the arrangement of electric charge carriers is occurred. To compensate the electric field, the charges start to polarize with movements of positive and negative charges to the opposite directions. The dielectric behavior was contributed by several dielectric

mechanisms, which may exist in a material and contribute to overall ε. Dielectric mechanisms contain resonance and relaxation processes. Resonance processes include electronic and atomic polarization, and relaxation processes consist of dipole and ionic relaxation. Electronic polarization is the deformation of the structure symmetry of atoms caused by the applied field. The small displacement occurs between the distribution center of negative and positive charges in the nucleus. Atomic polarization occurs when atoms are displaced from the equilibrium positions by stretching chemical bonds between atoms caused by the applied field.[67] Dipole relaxation is the process of alignments of permanent and induced dipoles to an applied field. Ionic relaxation is the dipole moment caused by the movement of positive and negative ions to the opposite direction under the applied field.[68] These dielectric mechanisms are explained in Figure 1.14. At the frequencies of microwave, dipole orientation and ion conduction strongly react to the frequency changes while atomic and electronic relaxation remain constant. As frequencies increase, characteristic frequencies, which are contributed by the fast mechanisms instead of slow mechanisms, appear as cutoffs or peaks on the curves of ε' and ε''. The intensities and characteristic frequencies for each mechanism vary by materials. For example, ε' of Teflon is constant even in the millimeter-wave ($3^{10}\ to\ 3^{11}\ Hz$) region due to no dipolar mechanism, but ε' of water dropped off around $2.2^{11}\ Hz$.[69]

As discussed in the previous section, both ε' and σ' are affected by the degree of the internal order of structure. The order-disorder transition can be monitored by the shape changes of curves of ε' and σ', which is explained in Figure 1.15.[70] At the low temperatures, σ' is low and linearly changes with frequency. With increasing temperatures, σ' increases and a short plateau appears at the low frequency region. Then, the region of plateau increases with the increase of temperature with a little rise of σ'. The low σ' and linear curve at low temperatures show that σ' is very

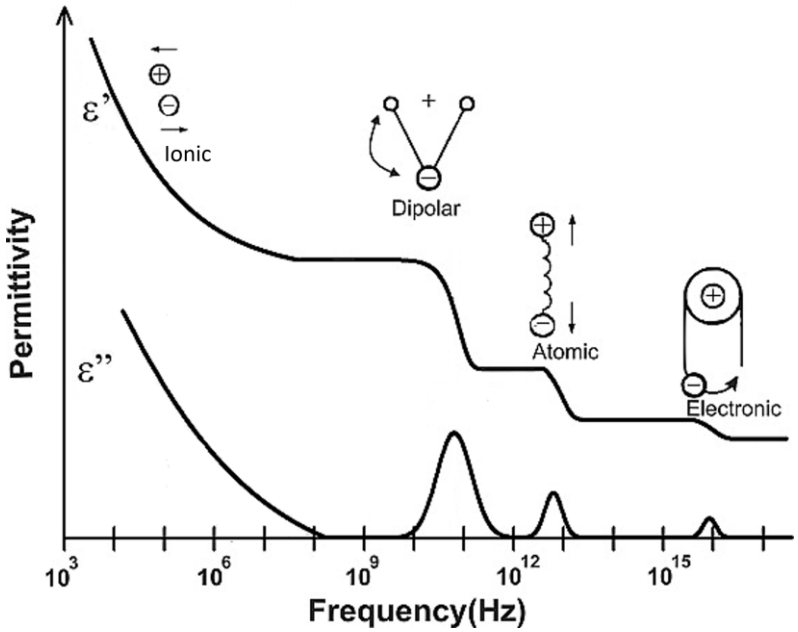

Figure 1.14 Response of dielectric mechanisms to frequency. Reproduced with permission from Reference [69]. Copyright 2006 American Geophysical Union.

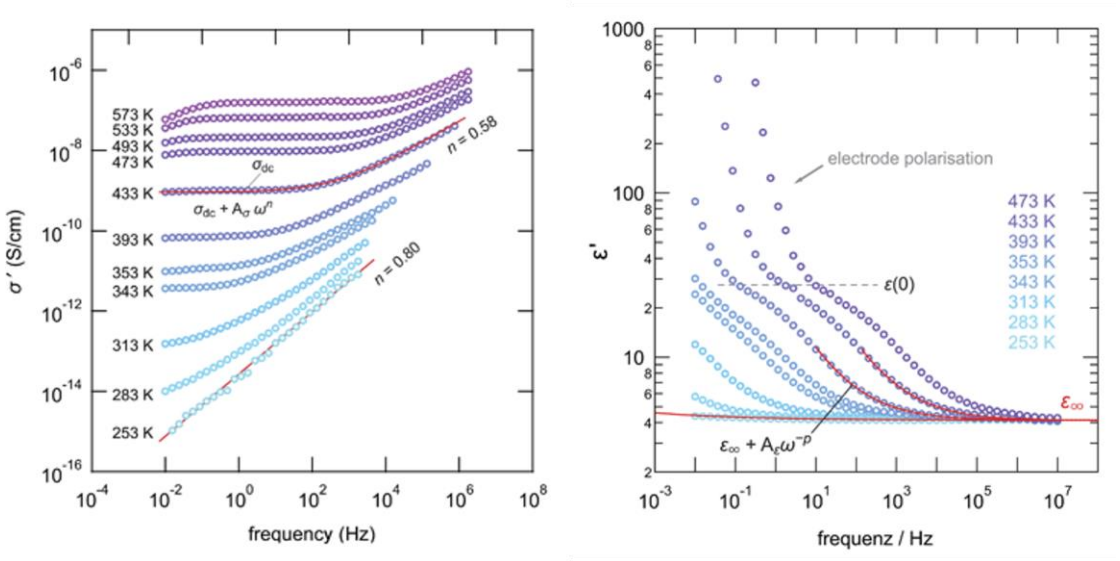

Figure 1.15 Conductivity (left) and permittivity (right) isotherms of ball-milled $LiAlO_2$. Reprinted with permission from Reference [70]. Copyright 2014 The Royal Society of Chemistry.

restrained in an ordered state. The plateau region, generally termed as DC conductivity plateau, is a bulk response and reflects the long-range ion transportation, which means the disordered state.[71] The similar transition of ε' with temperatures can also be observed as the sharp increase of ε' at low frequency and possible "bumps" appear on the curves, reflecting the freedom of dipole movements increases with decreasing of degree of order. Based on the above discussions, conductivity and permittivity isotherms were measured by DS in this work to monitor the order-disorder transition and determine T_{ODT} from another mechanism which differs from SAXS.

1.5.3 Structures at Liquid/Liquid Interface

The techniques, including second harmonic generation (SHG) spectroscopy and sum frequency generation (SFG) spectroscopy, can provide direct experimental information about the molecular orientation at the liquid/liquid interface.[72] SFG is a second-order nonlinear optical process based on the phase

matching and light fields summation induced by the ordered but non-centrosymmetric structures formed by the arrangement of molecules.[73] In experiments, two incident beams of lasers with frequencies of $f_1$and f_2 are focused on the surface of the sample to produce the output beam with the frequency of $f_3 = f_1 + f_2$, which is explained in Figure 1.16. When $f_1 = f_2$, SHG is obtained. As the special case of SFG, the output beam of SHG has a $f_{output} = 2f_{incident}$.[74]

In this work, SFG with visible (VIS) and infrared (IR) lasers was used. With the IR laser, the sample is excited from vibrational ground to vibrational excited state, then this excited state is further excited by the visible laser with a fixed wavelength to a virtual state. If the frequency of IR is tuned to permit the transition, the intensity of SFG will be $f_1 + f_2$. Further, as an even-order nonlinear optical process, the signals from centrosymmetric region and isotropic media will not be detected, which is illustrated in Figure 1.17.[75] Here the induced dipole moment per unit volume is

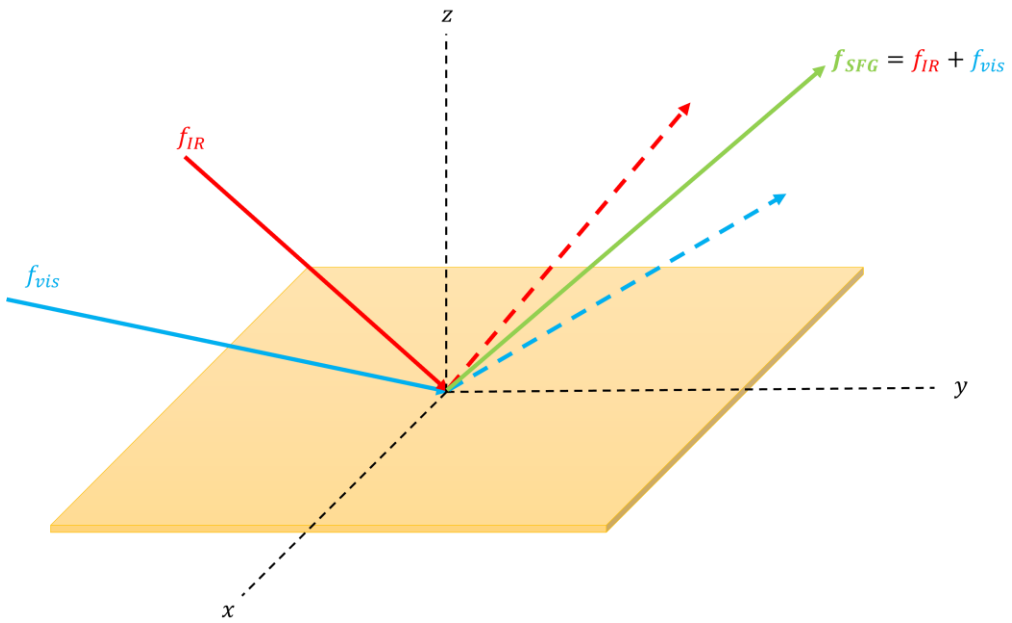

Figure 1.16 Schematic explanation of an SFG experiment.

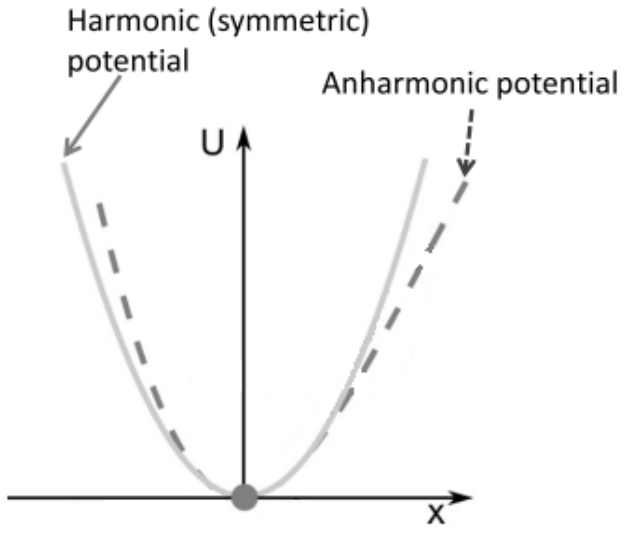

Figure 1.17 Difference between non-centrosymmetric and centrosymmetric medium in potential. Reproduced with permission from Reference [75]. Copyright 2016 AIP Publishing.

P, and the applied field is E, there is the relationship that:

$$p = \chi^{(1)}E + \chi^{(2)}E^2 + \chi^{(3)}E^3 + \cdots$$

where $\chi^{(1)}$, $\chi^{(2)}$, and $\chi^{(3)}$ describe the linear optics, second-order effects, and third-order effects.[76] For the centrosymmetric medium, $\chi^{(2)} = 0$ while the non-centrosymmetric medium is not. $\chi^{(2)}$ vanishes the identical potential and thus give information for non-centrosymmetric medium.[77]

In general, three polarization combinations are often used in SFG experiments, including ssp, sps, and ppp. The three letters from left to right stand for sum frequency, visible, and infrared, separately. The letter s or p represents s or p-polarized. For example, ssp is s-polarized sum frequency, s-polarized visible, and p-polarized infrared RI lights. The strengths of resonance for different combinations of polarization can be related to the susceptibilities of SFG active groups.[78] In this work, ssp is preferred due to the strong dominant peak of the symmetric stretch of methyl groups on polydimethylsiloxane (PDMS), whose structure is the same as oDMS.[79]

The techniques applied in this work were summarized with basic working principles and the expected results in Table 1.1.

Table 1.1 Basic working principles and expected results of SAXS, DS, and SFG.

Instrument Name	**Basic Working Principle**	**Obtained Result**
SAXS	Scattering	Morphology, T_{ODT}
DS	Interaction between dipole moment and applied electric field	T_{ODT}, Ion conductivity
SFG	Phase matching and light fields summation	Changes in interfacial structures

References

1. MacFarlane, D. R.; Kar, M.; Pringle, J. M., *Fundamentals of ionic liquids: from chemistry to applications*. John Wiley & Sons: 2017.

2. Walden, P., Molecular weights and electrical conductivity of several fused salts. *Bull. Acad. Imper. Sci.(St. Petersburg)* **1914,** *1800*.

3. Johnson, K. E., What's an ionic liquid? *The Electrochemical Society Interface* **2007,** *16* (1), 38.

4. Welton, T., Room-temperature ionic liquids. Solvents for synthesis and catalysis. *Chemical reviews* **1999,** *99* (8), 2071-2084.

5. Badri, M.; Brunet, J.-J.; Perron, R., Ionic liquids as solvents for the regioselective O-alkylation of C/O ambident nucleophiles. *Tetrahedron letters* **1992,** *33* (31), 4435-4438.

6. Freemantle, M., *An introduction to ionic liquids*. Royal Society of chemistry: 2010.

7. Hayes, R.; Warr, G. G.; Atkin, R., Structure and nanostructure in ionic liquids. *Chemical reviews* **2015,** *115* (13), 6357-6426.

8. Yuan, J.; Mecerreyes, D.; Antonietti, M., Poly (ionic liquid) s: An update. *Progress in Polymer Science* **2013,** *38* (7), 1009-1036.

9. Carrasco, P. M.; Ruiz de Luzuriaga, A.; Constantinou, M.; Georgopanos, P.; Rangou, S.; Avgeropoulos, A.; Zafeiropoulos, N. E.; Grande, H.-J.; Cabanero, G.; Mecerreyes, D., Influence of anion exchange in self-assembling of polymeric ionic liquid block copolymers. *Macromolecules* **2011,** *44* (12), 4936-4941.

10. Yuan, J.; Soll, S.; Drechsler, M.; Müller, A. H.; Antonietti, M., Self-assembly of poly (ionic liquid) s: Polymerization, mesostructure formation, and directional alignment in one step. *Journal of the American Chemical Society* **2011,** *133* (44), 17556-17559.

11. Seno, K. I.; Kanaoka, S.; Aoshima, S., Synthesis and LCST-type phase separation behavior in organic solvents of poly (vinyl ethers) with pendant imidazolium or pyridinium salts. *Journal of Polymer Science Part A: Polymer Chemistry* **2008,** *46* (17), 5724-5733.

12. Yoshimitsu, H.; Kanazawa, A.; Kanaoka, S.; Aoshima, S., Well-defined polymeric ionic liquids with an upper critical solution temperature in water. *Macromolecules* **2012,** *45* (23), 9427-9434.

13. Kausar, A., Research progress in frontiers of poly (ionic liquid) s: A review. *Polymer-Plastics Technology and Engineering* **2017,** *56* (17), 1823-1838.

14. Mecerreyes, D., Polymeric ionic liquids: Broadening the properties and applications of polyelectrolytes. *Progress in Polymer Science* **2011,** *36* (12), 1629-1648.

15. Matsumoto, M.; Shimizu, S.; Sotoike, R.; Watanabe, M.; Iwasa, Y.; Itoh, Y.; Aida, T., Exceptionally high electric double layer capacitances of oligomeric ionic liquids. *Journal of the American Chemical Society* **2017,** *139* (45), 16072-16075.

16. Stryutsky, A. V.; Korolovych, V. F.; Lee, H.; Mikan, E.; Erwin, A.; Sobko, O. O.; Gumenna, M. A.; Klimenko, N. S.; Shevchenko, V. V.; Bulavin, L. A. In *Oligomeric and polymeric ionic liquids: Engineering architecture and morphology*, International Conference Physics of Liquid Matter: Modern Problems, Springer: 2018; pp 93-118.

17. Dewilde, S.; Dehaen, W.; Binnemans, K., Ionic liquids as solvents for PPTA oligomers. *Green Chemistry* **2016,** *18* (6), 1639-1652.

18. Matuszek, K.; Brzeczek-Szafran, A.; Kobus, D.; MacFarlane, D. R.; Swadźba-Kwaśny, M.; Chrobok, A., Protic ionic liquids based on oligomeric anions [(HSO4)(H2SO4) x]−(x= 0, 1, or 2) for a clean ϵ-caprolactam synthesis. *Australian Journal of Chemistry* **2019,** *72* (2), 130-138.

19. Chen, L.; Mullen, G. E.; Le Roch, M.; Cassity, C. G.; Gouault, N.; Fadamiro, H. Y.; Barletta, R. E.; O'Brien, R. A.; Sykora, R. E.; Stenson, A. C., On the formation of a protic ionic liquid in nature. *Angewandte Chemie International Edition* **2014,** *53* (44), 11762-11765.

20. Skoog, D. A.; West, D. M.; Holler, F. J.; Crouch, S. R., *Fundamentals of analytical chemistry*. Cengage learning: 2013.

21. Jesus, F.; Passos, H.; Ferreira, A. M.; Kuroda, K.; Pereira, J. L.; Gonçalves, F. J.; Coutinho, J. A.; Ventura, S. P., Zwitterionic compounds are less ecotoxic than their analogous ionic liquids. *Green Chemistry* **2021,** *23* (10), 3683-3692.

22. Hashimoto, H.; Nelson, M. G.; Switzer, C., Zwitterionic DNA. *Journal of the American Chemical Society* **1993,** *115* (16), 7128-7134.

23. Ga, D.-H.; Lim, C.-M.; Jang, Y.; Son, T. I.; Han, D. K.; Joung, Y. K., Surface-Modifying Effect of Zwitterionic Polyurethane Oligomers Complexed with Metal Ions on Blood Compatibility. *Tissue Engineering and Regenerative Medicine* **2022,** *19* (1), 35-47.

24. Pispas, S.; Hadjichristidis, N., End-functionalized block copolymers of styrene and isoprene: synthesis and association behavior in dilute solution. *Macromolecules* **1994,** *27* (7), 1891-1896.

25. Yoon, S.; MacKnight, W. J.; Hsu, S. L., End-group effect on chain conformation of poly (propylene glycol) and poly (ethylene glycol). *Journal of applied polymer science* **1997,** *64* (1), 197-202.

26. Xu, Y.; Huang, J.; Li, Y.; Wang, M.; Cao, Y.; Yuan, C.; Zeng, B.; Dai, L., A novel hybrid polyhedral oligomeric silsesquioxane-based copolymer with zwitterion: Synthesis, characterization, self-assembly behavior and pH responsive property. *Macromolecular Research* **2017,** *25* (8), 817-825.

27. Jalbert, C.; Koberstein, J. T.; Hariharan, A.; Kumar, S. K., End group effects on surface properties of polymers: semiempirical calculations and comparison to experimental surface tensions for α, ω-functional poly (dimethylsiloxanes). *Macromolecules* **1997,** *30* (15), 4481-4490.

28. Jo, G.; Kim, O.; Kim, H.; Hyeok Choi, U.; Lee, S.-B.; Jeong Park, M., End-functionalized block copolymer electrolytes: effect of segregation strength on ion transport efficiency. *Polymer Journal* **2016,** *48* (4), 465-472.

29. Qiu, X.; Koga, T.; Tanaka, F.; Winnik, F. M., New insights into the effects of molecular weight and end group on the temperature-induced phase transition of poly(N-isopropylacrylamide) in water. *Science China Chemistry* **2013,** *56* (1), 56-64.

30. Perkin, S.; Albrecht, T.; Klein, J., Layering and shear properties of an ionic liquid, 1-ethyl-3-methylimidazolium ethylsulfate, confined to nano-films between mica surfaces. *Physical Chemistry Chemical Physics* **2010,** *12* (6), 1243-1247.

31. Santos, H. A.; García-Morales, V.; Pereira, C. M., Electrochemical properties of phospholipid monolayers at liquid–liquid interfaces. *ChemPhysChem* **2010,** *11* (1), 28-41.

32. Volkov, A. G., *Liquid interfaces in chemical, biological and pharmaceutical applications*. CRC Press: 2001.

33. Fredlake, C. P.; Crosthwaite, J. M.; Hert, D. G.; Aki, S. N.; Brennecke, J. F., Thermophysical properties of imidazolium-based ionic liquids. *Journal of Chemical & Engineering Data* **2004,** *49* (4), 954-964.

34. Crosthwaite, J. M.; Muldoon, M. J.; Dixon, J. K.; Anderson, J. L.; Brennecke, J. F., Phase transition and decomposition temperatures, heat capacities and viscosities of pyridinium ionic liquids. *The Journal of Chemical Thermodynamics* **2005,** *37* (6), 559-568.

35. Liu, S.; Yan, G.; Wang, J.; Zhou, J.; Bie, L.; Jia, Y.; Meng, F., Self-assembly, phase behaviour and ion-conducting property of pyridinium-based ionic liquid-crystalline oligomers. *Liquid Crystals* **2021,** *48* (2), 201-214.

36. Jo, G.; Ahn, H.; Park, M. J., Simple route for tuning the morphology and conductivity of polymer electrolytes: one end functional group is enough. *ACS Macro Letters* **2013,** *2* (11), 990-995.

37. Moyer, B. A., *Ion exchange and solvent extraction: Volume 23, Changing the landscape in solvent extraction*. CRC Press: 2019; Vol. 23.

38. Shi, S.; Russell, T. P., Nanoparticle Assembly at Liquid–Liquid Interfaces: From the Nanoscale to Mesoscale. *Advanced Materials* **2018,** *30* (44), 1800714.

39. Uchiyama, Y.; Kitamori, T.; Sawada, T.; Tsuyumoto, I., Role of the Liquid/Liquid Interface in a Phase-Transfer Catalytic Reaction As Investigated by in Situ Measurements Using the Quasi-Elastic Laser Scattering Method. *Langmuir* **2000,** *16* (16), 6597-6600.

40. Ali, M.; Ghosh, S. K., Chapter 31 - Liquid-liquid interface as scaffold for self-assembly of nanostructures into functional materials. In *Smart Nanocontainers*, Nguyen-Tri, P.; Do, T.-O.; Nguyen, T. A., Eds. Elsevier: 2020; pp 515-536.

41. Poli, E.; Jong, K. H.; Hassanali, A., Charge transfer as a ubiquitous mechanism in determining the negative charge at hydrophobic interfaces. *Nature Communications* **2020,** *11* (1), 901.

42. Rapaport, H., Ordered Peptide Assemblies at Interfaces. *Supramolecular Chemistry* **2006,** *18* (5), 445-454.

43. Tsionsky, M.; Bard, A. J.; Mirkin, M. V., Long-Range Electron Transfer through a Lipid Monolayer at the Liquid/Liquid Interface. *Journal of the American Chemical Society* **1997,** *119* (44), 10785-10792.

44. Villar, G.; Bayley, H., Functional Droplet Interface Bilayers. In *Encyclopedia of Biophysics*, Roberts, G. C. K., Ed. Springer Berlin Heidelberg: Berlin, Heidelberg, 2013; pp 861-868.

45. Taylor, G. J.; Luo, Y.; Hong, K.; Sarles, S. A.; Sacci, R. L.; Doughty, B.; Collier, C. P., Self-Assembly of Charged Oligomeric Bilayers at the Aqueous/Organic Interface Regulated by Ion-Pair Associations. **2020**.

46. Lin, L.; Chowdhury, A. U.; Ma, Y.-Z.; Sacci, R. L.; Katsaras, J.; Hong, K.; Collier, C. P.; Carrillo, J.-M. Y.; Doughty, B., Ion Pairing Mediates Molecular Organization Across Liquid/Liquid Interfaces. *ACS Applied Materials & Interfaces* **2021,** *13* (28), 33734-33743.

47. Nickmans, K.; Schenning, A. P., Directed Self-Assembly of Liquid-Crystalline Molecular Building Blocks for Sub-5 nm Nanopatterning. *Advanced Materials* **2018,** *30* (3), 1703713.

48. Kanzian, T.; Nigst, T. A.; Maier, A.; Pichl, S.; Mayr, H., Nucleophilic Reactivities of Primary and Secondary Amines in Acetonitrile. *European Journal of Organic Chemistry* **2009,** *2009* (36), 6379-6385.

49. Brotzel, F.; Kempf, B.; Singer, T.; Zipse, H.; Mayr, H., Nucleophilicities and Carbon Basicities of Pyridines. *Chemistry – A European Journal* **2007,** *13* (1), 336-345.

50. Baidya, M.; Brotzel, F.; Mayr, H., Nucleophilicities and Lewis basicities of imidazoles, benzimidazoles, and benzotriazoles. *Organic & Biomolecular Chemistry* **2010,** *8* (8), 1929-1935.

51. Wu, A. X.; Lin, S.; Mizrahi Rodriguez, K.; Benedetti, F. M.; Joo, T.; Grosz, A. F.; Storme, K. R.; Roy, N.; Syar, D.; Smith, Z. P., Revisiting group contribution theory for estimating

fractional free volume of microporous polymer membranes. *Journal of Membrane Science* **2021,** *636*, 119526.

52. Bondi, A., van der Waals Volumes and Radii. *The Journal of Physical Chemistry* **1964,** *68* (3), 441-451.

53. Díaz-Torres, R.; Alvarez, S., Coordinating ability of anions and solvents towards transition metals and lanthanides. *Dalton Transactions* **2011,** *40* (40), 10742-10750.

54. Seidlitz, A.; Thurn-Albrecht, T., Small-Angle X-ray Scattering for Morphological Analysis of Semicrystalline Polymers. In *Polymer Morphology*, 2016; pp 151-164.

55. Pauw, B. R., Everything SAXS: small-angle scattering pattern collection and correction. *Journal of Physics: Condensed Matter* **2013,** *25* (38), 383201.

56. Li, F.; Liu, Z.; Sun, T., Energy-dispersive small-angle X-ray scattering with cone collimation using X-ray capillary optics. *Review of Scientific Instruments* **2016,** *87* (9), 093106.

57. Rochette, C. N., *Structural analysis of nanoparticles by small angle X-ray scattering*. Universitaet Bayreuth (Germany): 2013.

58. Boldon, L.; Laliberte, F.; Liu, L., Review of the fundamental theories behind small angle X-ray scattering, molecular dynamics simulations, and relevant integrated application. *Nano Rev* **2015,** *6*, 25661-25661.

59. Schmidt, P. W., A review of some recent applications of small-angle scattering in studies of polydisperse systems and porous materials. *Makromolekulare Chemie. Macromolecular Symposia* **1988,** *15* (1), 153-166.

60. Craievich, A. F., Small-Angle X-ray Scattering by Nanostructured Materials. In *Handbook of Sol-Gel Science and Technology* [Online] Klein L., A. M., Jitianu A., Ed. Springer, Cham.: 2016.

61. Hamley, I.; Castelletto, V., Small-Angle Scattering of Block Copolymers. In *Soft Matter Characterization*, Borsali, R.; Pecora, R., Eds. Springer Netherlands: Dordrecht, 2008; pp 1021-1081.

62. Owen, J., 21 - Ionic Conductivity. In *Comprehensive Polymer Science and Supplements*, Allen, G.; Bevington, J. C., Eds. Pergamon: Amsterdam, 1989; pp 669-686.

63. Choi, J.-H.; Ye, Y.; Elabd, Y. A.; Winey, K. I., Network Structure and Strong Microphase Separation for High Ion Conductivity in Polymerized Ionic Liquid Block Copolymers. *Macromolecules* **2013,** *46* (13), 5290-5300.

64. Rondla, R.; Lin, J. C. Y.; Yang, C. T.; Lin, I. J. B., Strong Tendency of Homeotropic Alignment and Anisotropic Lithium Ion Conductivity of Sulfonate Functionalized Zwitterionic Imidazolium Ionic Liquid Crystals. *Langmuir* **2013,** *29* (37), 11779-11785.

65. Jafta, C. J.; Bridges, C.; Haupt, L.; Do, C.; Sippel, P.; Cochran, M. J.; Krohns, S.; Ohl, M.; Loidl, A.; Mamontov, E.; Lunkenheimer, P.; Dai, S.; Sun, X.-G., Ion Dynamics in Ionic-Liquid-Based Li-Ion Electrolytes Investigated by Neutron Scattering and Dielectric Spectroscopy. *ChemSusChem* **2018,** *11* (19), 3512-3523.

66. Deshmukh, K.; Sankaran, S.; Ahamed, B.; Sadasivuni, K. K.; Pasha, K. S. K.; Ponnamma, D.; Rama Sreekanth, P. S.; Chidambaram, K., Chapter 10 - Dielectric Spectroscopy. In *Spectroscopic Methods for Nanomaterials Characterization*, Thomas, S.; Thomas, R.; Zachariah, A. K.; Mishra, R. K., Eds. Elsevier: 2017; pp 237-299.

67. Psarras, G. C., 2 - Fundamentals of Dielectric Theories. In *Dielectric Polymer Materials for High-Density Energy Storage*, Dang, Z.-M., Ed. William Andrew Publishing: 2018; pp 11-57.

68. Feldman, Y.; Puzenko, A.; Ryabov, Y., Dielectric Relaxation Phenomena in Complex Materials. In *Fractals, Diffusion, and Relaxation in Disordered Complex Systems*, 2006; pp 1-125.

69. Chen, Y.; Or, D., Effects of Maxwell-Wagner polarization on soil complex dielectric permittivity under variable temperature and electrical conductivity. *Water Resources Research* **2006,** *42* (6).

70. Wohlmuth, D.; Epp, V.; Bottke, P.; Hanzu, I.; Bitschnau, B.; Letofsky-Papst, I.; Kriechbaum, M.; Amenitsch, H.; Hofer, F.; Wilkening, M., Order vs. disorder—a huge increase in ionic conductivity of nanocrystalline LiAlO2 embedded in an amorphous-like matrix of lithium aluminate. *Journal of Materials Chemistry A* **2014,** *2* (47), 20295-20306.

71. Chaurasia, S.; Saroj, A.; Shalu; Singh, V.; Tripathi, A.; Gupta, A.; Verma, Y.; Singh, R., Studies on structural, thermal and AC conductivity scaling of PEO-LiPF6 polymer electrolyte with added ionic liquid [BMIMPF6]. *AIP Advances* **2015,** *5* (7), 077178.

72. Benjamin, I., MOLECULAR STRUCTURE AND DYNAMICS AT LIQUID-LIQUID INTERFACES. *Annual Review of Physical Chemistry* **1997,** *48* (1), 407-451.

73. Kumar, V.; Coluccelli, N.; Polli, D., Chapter 5 - Coherent Optical Spectroscopy/Microscopy and Applications. In *Molecular and Laser Spectroscopy*, Gupta, V. P., Ed. Elsevier: 2018; pp 87-115.

74. Erbe, A.; Nayak, S.; Chen, Y. H.; Niu, F.; Pander, M.; Tecklenburg, S.; Toparli, C., How to Probe Structure, Kinetics, and Dynamics at Complex Interfaces In Situ and Operando by Optical Spectroscopy. In *Encyclopedia of Interfacial Chemistry*, Wandelt, K., Ed. Elsevier: Oxford, 2018; pp 199-219.

75. Cazzanelli, M.; Schilling, J., Second order optical nonlinearity in silicon by symmetry breaking. *Applied Physics Reviews* **2016,** *3* (1), 011104.

76. Choudhary, S.; Boyd, R. W., Tutorial on nonlinear optics. 2016; pp 31-76.

77. Chen, Z., Understanding surfaces and buried interfaces of polymer materials at the molecular level using sum frequency generation vibrational spectroscopy. *Polymer International* **2007,** *56* (5), 577-587.

78. Zhuang, X.; Miranda, P.; Kim, D.; Shen, Y., Mapping molecular orientation and conformation at interfaces by surface nonlinear optics. *Physical Review B* **1999,** *59* (19), 12632.

79. Kim, C.; Gurau, M. C.; Cremer, P. S.; Yu, H., Chain conformation of poly (dimethyl siloxane) at the air/water interface by sum frequency generation. *Langmuir* **2008,** *24* (18), 10155-10160.

CHAPTER 2 SYNTHESIS OF END-GROUP FUNCTIONALIZED DIMETHYL SILOXANE OLIGOMERS (oDMS)

Abstract

In this chapter, we described the synthesis and characterization of a library of oDMS oligomers with different ionic and zwitterionic end groups by a metal-free and scalable method with high conversion. Starting from the custom-synthesized monon-hydroxyl terminated oDMS (oDMS-*OH*) and mainly using commercially available oDMS-*OH*, different anion precursors, including mesylate, tosylate, triflate, and bromide, were introduced by esterification or S_N2 substitution. Then, different cations were installed through S_N2 substitution with the corresponding amines, including imidazole, pyridine, and morpholine, to afford the mono-ionic chain end oDMS (oDMS-*IL*). For mono-zwitterionic chain ends, hydroxyl groups were modified into tertiary amine groups, followed by ring-opening of 1,3-propanesultone to obtain mono-zwitterionic (sulfobetaine) chain end oDMS (oDMS-*ZW*). To compare the effects of ionic and zwitterionic chain ends, tertiary amine terminated oDMS was reacted with methanesulfonic acid to afford oDMS-*IL* with a similar chemical structure as oDMS-*ZW*. The end-group modifications of oDMS were summarized in Figure 2.1.

Throughout the reaction, proton nuclear magnetic resonance (^{1}H NMR) spectroscopy was employed to monitor the reaction progresses and confirm the purity of the resulting materials. As shown in the spectra of ^{1}H NMR and matrix-assisted laser desorption/ionization time-of-flight mass spectrometry (MALDI-TOF MS), the peaks in ^{1}H NMR shift very clean in an expected manner for each product, and the exact molecular weight of each oDMS with different cationic species identically matched the predicted numbers, which confirming the high purity of the end-functionalized oDMSs.

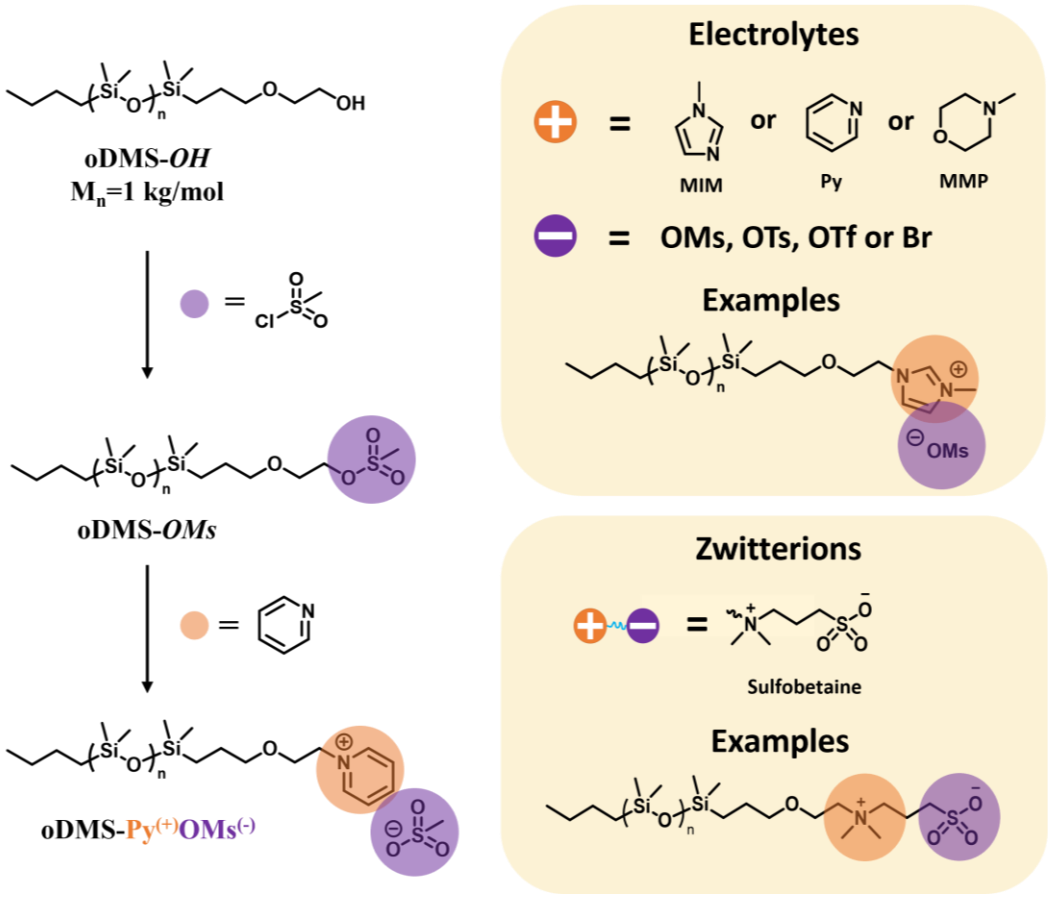

Figure 2.1 Chain end modification of oDMS-*OH*.

2.1 Introduction

The development of new materials with desirable structures and properties, including self-assembly, ion conducting, and other tunable features, requires specific functionality in polymers or oligomers. One straightforward approach to introduce functionality on the backbone or side chains of polymers is controlled polymerization of tailor-made monomers with predesigned structures. However, the synthesis of special monomers is usually time-consuming and the functionality itself will affect the polymerization process, which leads to a large dispersity or even the failure of the polymerization. Thus, this high-precision method gives limited examples for well-defined polymers. To obtain various kinds of functional polymers, different methodologies, including chain extension from functionalized initiators and chain-end transformation of well-defined samples have been developed. Both approaches provide end groups for further modifications, involving end-capping with amine, halides, carboxyl, ester, ionic and zwitterionic groups, by taking advantage of the versatility of organic reactions.[1, 2] Although the number of functionalized groups on chain-end modified polymers is much lower than that of highly functionalized polymers from designed monomers, the properties of end-group modified polymers or oligomers can be tuned with one single chain end, which has been discussed in Chapter 1. Because of its efficiency and convenience, end group modification is chosen in this work.

Among diverse end groups, hydroxyl groups are often selected as the starting point because they can be effectively reacted into ether, ester, mesylate, tosylate, triflate, halide, amines, and other end groups with a conversion higher than 90%.[3] However, this efficiency is still not enough for end group modification of oligomers because of their moderate molecular weights between polymers and small molecules. First, compared with small molecules, the oligomer chains lower the chances of collisions between chain ends and reactants which gives a suppressed yield. In

general, the tosylation of decyl alcohol with p-toluenesulfonyl chloride is almost quantitative.[4] In terms of oligo(isobutylenes), Mülhaupt, Iván, and coworkers obtained a conversion of 93% for tosylation, and 7% of hydroxyl groups were converted into chloride groups.[5] Second, the nature of oligomers makes them hard to purify. Small molecules can be purified by column chromatography or recrystallization, while low functionalities of oligomers give a weak signal on thin layer chromatography leading to loss of materials, and most of them will not crystallize. Although oligomers can be purified via column chromatography, this technique will be the last choice due to its laborious and the potential risk of material loss. Like polymers, the best purification method is precipitation, while the choice of reactants is limited due to the solubility for the precipitation process. Thus, the development of end group modification method with high conversion for oligomers is needed.

For silicone-based materials, metal catalysts are often used because of their high efficiency. For example, hydrosilylation is very effective with the Karstedt catalyst (a platinum-contained catalyst). However, based on our experiences, platinum in Karstedt catalyst is very difficult to remove from silicon compounds after reactions resulted in black-colored products. So, a metal-free method is also required to obtain chain-end modified oligomers with high purity.

To prove the success of end group modification and purity of obtained samples, effective end-group analysis is required. ^{1}H NMR spectroscopy and MALDI-TOF MS are the most powerful techniques for this task. ^{1}H NMR spectroscopy gives reliable signals with integrations that are directly related to protons in different chemical environments, and end groups can be identified and quantified. Not only end groups but also molecular weight of end-group functionalized oligomers can be calculated based on ratios of protons at end groups and backbones.[6, 7] However, another important parameter, dispersity (dispersions of distributions of molar masses)[8], which

proves the quality of samples that these oligomers do not be degraded during reactions, cannot be analyzed by ^{1}H NMR spectroscopy. With MALDI-TOF MS, both end groups and repeat units can be determined according to the single-charged quasi-molecular ions with fragmentations.[9]

In summary, this work developed a metal-free and high-conversion end group modification method for oDMS to obtain high-quality model materials.

2.2 Experiments

2.2.1 Materials

All reagents were used as received from Sigma-Aldrich, Fisher Scientific, and VWR International without further purification unless otherwise noted. oDMS-*OH* was purchased from Gelest, and the molecular weight (1256 kg/mol, n=14) was checked with ^{1}H NMR, which was shown in Figure 2.1.

2.2.2 Synthesis of anion and cation oDMS precursors

Oligodimethylsiloxane mesylate (oDMS-*OMs*) was synthesized by the following procedure, which was illustrated in Scheme 2.1:[10] Into a 250 ml Schlenk flask, oDMS-*OH* (10.0 g, 10 mmol, 1.0 eq), triethylamine (1.3 g, 13 mmol, 1.3 eq) and dichloromethane (DCM) (100 ml) was added under an inert atmosphere. Then, methanesulfonyl chloride (MsCl) (1.4 g, 12 mmol, 1.2 eq) was added dropwise into the solution in an ice bath. The reaction was stirred overnight at room temperature (RT). After condensing the solution, the oligomer solution was precipitated in a large excess of cold methanol/ H2O (v/v = 8/1) solution, affording the pure target product as a colorless oil with quantitative yield. ^{1}H NMR spectrum was shown in the Appendix with Figure S1.

Oligodimethylsiloxane tosylate (oDMS-*OTs*) was prepared by a similar procedure which was shown in scheme 2.2:[4] In a typical procedure, a 250 ml dry Schlenk flask was charged with 10.0 g of oDMS-*OH* (10 mmol, 1.0 eq), 1.3 g of triethylamine (13 mmol, 1.3 eq), and 100 ml of

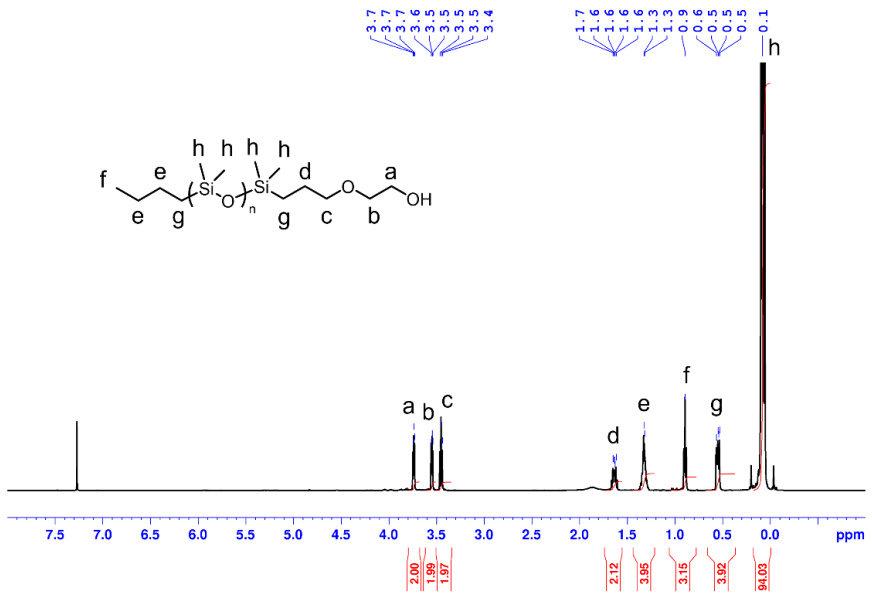

Figure 2.1 [1]HNMR spectrum of oDMS-*OH*.

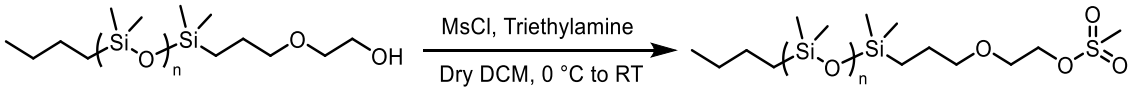

Scheme 2.1 Synthesis of oDMS-*OMs*.

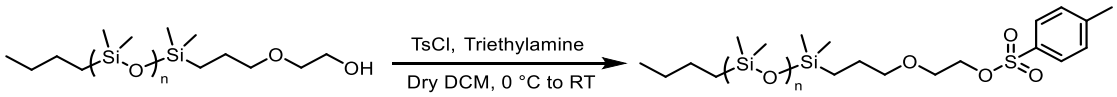

Scheme 2.2 Synthesis of oDMS-*OTs*.

dry dichloromethane. Then, the flask was subsequently put into an ice bath. 2.3 g of p-toluenesulfonyl chloride (TsCl) (12 mmol, 1.2 eq) was added portionwise into the solution under an inert atmosphere. The reaction was allowed warm to room temperature and stir for overnight. The solution was then condensed and precipitated in a large excess of cold methanol/ H2O (v/v = 8/1) solution, affording the colorless oil as the crude product as 92% oDMS-*OTs* and 8% oDMS-*OH*. oDMS-*OTs* were separated by column chromatography (Hexanes/DCM = 2:1), and a colorless oil was obtained as the final product. (92% isolated yield) ^{1}H NMR spectrum was shown in the Appendix with Figure S2.

Oligodimethylsiloxane triflate (oDMS-*OTf*) was converted by the described method, which was illustrated in Scheme 2.3: 10.0 g of oDMS-*OH* (10 mmol, 1.0 eq), 1.1 g of pyridine (14 mmol, 1.4 eq), and 100 ml of anhydrous dichloromethane were added into a 250 mL Schlenk flask. The mixture was then put into an acetone/dry ice bath. 3.38 g of trifluoromethanesulfonic anhydride (OTf_2) (12 mmol, 1.2 eq) was added dropwise into the solution under a nitrogen atmosphere. The reaction was kept in the acetone/dry ice bath and stirred for 4 hours. Then, water was added into the reaction. The organic layer was collected and washed with water quickly three times. After drying the organic layer with $MgSO_4$, the solvent was removed. oDMS-*OTf* was purified by column chromatography (Hexanes/DCM = 5:1) as a colorless oil. (74% isolated yield). ^{1}H NMR spectrum was shown in the Appendix with Figure S3.

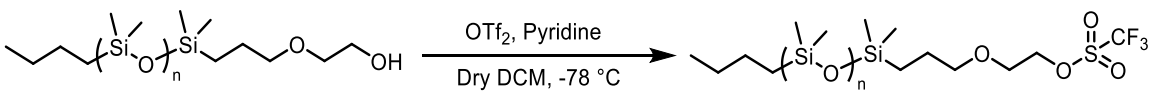

Scheme 2.3 Synthesis of oDMS-*OTf*.

Oligodimethylsiloxane bromide (oDMS-*Br*) was synthesized by Appel reaction, which was shown in Scheme 2.4.[11] In a typical procedure, a 500 ml Schlenk flask under an inert atmosphere was added with oDMS-*OH* (15.0 g 15 mmol, 1.0 eq), triphenylphosphine (PPh_3) (4.8 g, 18 mmol, 1.2 eq), and 180 ml of dichloromethane. After putting the flask into an ice bath, 6.0 g of carbon tetrabromide (CBr_4) (18 mmol, 1.2 eq) was added portionwise and stirred overnight at room temperature. Sequentially, the condensed solution was precipitated in the cold methanol/ H2O (v/v = 8/1) solution to obtain the colorless oil with quantitative yield. ^{1}H NMR spectrum was shown in the Appendix with Figure S4.

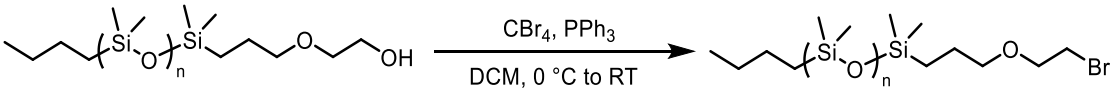

Scheme 2.4 Synthesis of oDMS-*Br*.

Dimethylamine terminated oligodimethylsiloxane (oDMS-*N(CH$_3$)$_2$*) was prepared from oDMS-*Br* with the modified procedure which was shown in Scheme 2.5.[12] Into a 250 ml Schlenk flask, 10 g of oDMS-Br (10 mmol, 1.0 eq) and 3.3 mL of pyridine (41 mmol, 4.1 eq) were first added. Then, 100 ml of dimethylamine ($NH(CH_3)_2$) (2.0 M) in tetrahydrofuran (THF) solution was charged into the mixture and stirred overnight at 40 ˚C. After precipitation of condensed solution in the cold methanol/ H2O (v/v = 6/1) solution, a light-green oil with quantitative yield was afforded as the pure compound. ^{1}H NMR spectrum was shown in the Appendix with Figure S5.

2.2.3 Preparation of oDMS with ionic chain ends

Imidazolium based oDMS with ionic chain ends, including oligodimethylsiloxane

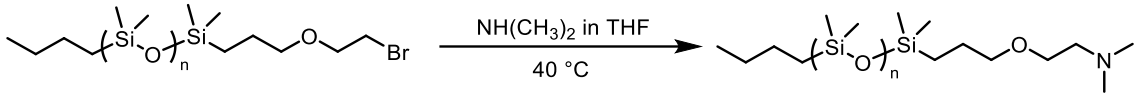

Scheme 2.5 Synthesis of oDMS-*N(CH$_3$)$_2$*.

imidazolium mesylate (oDMS-*MIM$^{(+)}$OMs$^{(-)}$*), oligodimethylsiloxane imidazolium tosylate (oDMS-*MIM$^{(+)}$OTs$^{(-)}$*), oligodimethylsiloxane imidazolium triflate (oDMS-*MIM$^{(+)}$OTf$^{(-)}$*), and oligodimethylsiloxane imidazolium bromide (oDMS-*MIM$^{(+)}$Br$^{(-)}$*), were converted from the corresponding anion oDMS precursors and illustrated in Scheme 2.6. Anion oDMS precursors (2.0 g, 2.0 mmol, 1.0 eq), 1-methylimidazole (2.0 g, 24.4 mmol, 12.2 eq) and 2 ml of toluene were added into a 20 mL vial. After purging with nitrogen for 30 mins, the mixture was heated at 110 ˚C for 24 hours. Toluene and excess imidazolium were removed at 90 ˚C under high vacuum for 48 hours to obtain the final product as the brown gel with quantitative yield. ^{1}H NMR and MS spectrum were shown in the Appendix from Figure S6 to S13.

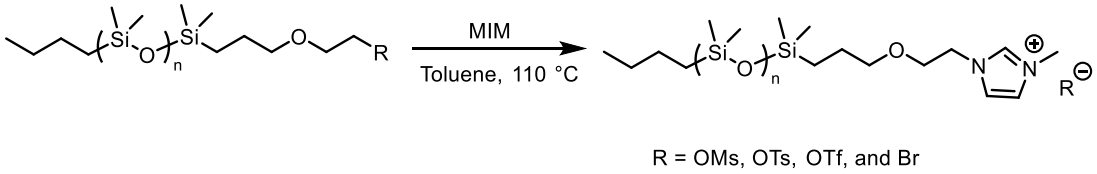

Scheme 2.6 Synthesis of oDMS with *MIM$^{(+)}$* based charged chain ends.

Pyridinium based oDMS with ionic chain ends, consist of oligodimethylsiloxane pyridinium mesylate (oDMS-*Py$^{(+)}$OMs$^{(-)}$*), oligodimethylsiloxane pyridinium tosylate (oDMS- *Py $^{(+)}$OTs$^{(-)}$*),

oligodimethylsiloxane pyridinium triflate (oDMS- *Py* $^{(+)}$*OTf*$^{(-)}$), and oligodimethylsiloxane pyridinium bromide (oDMS- *Py* $^{(+)}$*Br*$^{(-)}$), were synthesized through the following approach and shown in Scheme 2.7: into a 20 mL vial, anion oDMS precursors (2.0 g, 2.0 mmol, 1.0 eq) and 5 mL of pyridine were added and then purged with nitrogen for 30 mins. After heating at 90 ˚C for 24 hours, removal of excess pyridinium was performed at 90 ˚C under high vacuum for 48 hours to afford the brown gel with quantitative yield. ^{1}H NMR and MS spectrum were shown in the Appendix from Figure S14 to S21.

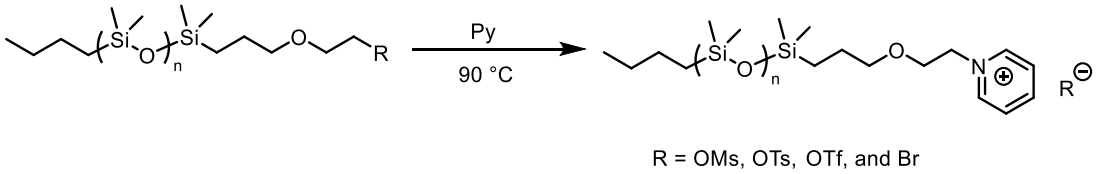

Scheme 2.7 Synthesis of oDMS with *Py*$^{(+)}$ based charged chain ends.

Morpholinium based oDMS with ionic chain ends, comprising oligodimethylsiloxane morpholinium mesylate (oDMS-*MMP*$^{(+)}$*OMs*$^{(-)}$), oligodimethylsiloxane morpholinium tosylate (oDMS- *MMP* $^{(+)}$*OTs*$^{(-)}$), oligodimethylsiloxane morpholinium triflate (oDMS- *MMP* $^{(+)}$*OTf*$^{(-)}$), and oligodimethylsiloxane morpholinium bromide (oDMS- *MMP* $^{(+)}$*Br*$^{(-)}$), were prepared by the similar method and illustrated in Scheme 2.8: After adding 2.0 g of anion oDMS precursors (2.0 mmol, 1.0 eq), 2.46 g of N-methylmorpholine (24.3 mmol, 12.2 eq), and 2 ml of toluene into a 20 mL flask, the solution was purged with nitrogen for 30 mins, followed by heating at 90 ˚C for 24 hours. Solvent and excess reactant were removed under high vacuum for 2 days at 90 ˚C. A brown gel was collected with quantitative yield as the final product without further purification, except

for oDMS- *MMP* $^{(+)}Br^{(-)}$. During the reaction, white solids started to precipitate due to the poor thermal stability of oDMS- *MMP* $^{(+)}Br^{(-)}$. After filtering the white salts, column chromatography was performed to purify the crude oDMS- *MMP* $^{(+)}Br^{(-)}$. The unreacted oDMS-*Br* was flashed by DCM and the pure product was collected with methanol (80% isolated yield). ^{1}H NMR and MS spectrum were shown in the Appendix from Figure S22 to S29.

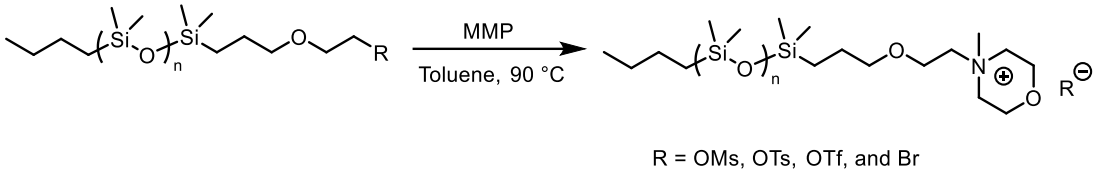

Scheme 2.8 Synthesis of oDMS with *MMP*$^{(+)}$ based charged chain ends.

Oligodimethylsiloxane tertiary amino methanesulfonic acid (oDMS-*NH(CH$_3$)$_2$*$^{(+)}$MeSO$_3^{(-)}$) was synthesized by the described procedure, which was shown in Scheme 2.9: 0.5 g of cation oDMS precursor, which is oDMS-*N(CH$_3$)$_2$* (0.5 mmol, 1.0 eq) was dissolved in 5 mL of acetone in a 20 mL vial. Then, acetone solution, which contains equimolar methanesulfonic acid (MeSO$_3$H), was added dropwise into the mixture under the ice batch. After stirring at room temperature for 1 hour, acetone was removed under vacuum at room temperature. The product was redissolved in n-hexane and centrifuged to remove undissolved methanesulfonic acid if it existed. The pure product was a green viscous gel with quantitative yield, while the product would degrade in one day at room temperature.

2.2.4 Synthesis of oDMS with zwitterionic chain ends

Oligodimethylsiloxane sulfobetaine (oDMS-*N(CH$_3$)$_2$*$^{(+)}$*-(CH$_2$)$_3$-SO$_3^{(-)}$*) was prepared from

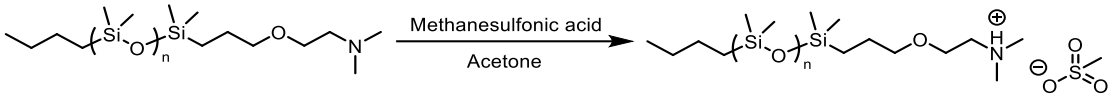

Scheme 2.9 Synthesis of oDMS-$NH(CH_3)_2^{(+)}MeSO_3^{(-)}$.

cation oDMS precursor with the improved procedure, which was illustrated in Scheme 2.10.[13] A 250 ml Schlenk flask was charged with 5 g of oDMS-$N(CH_3)_2$ (5 mmol, 1.0 eq) and 28 ml of acetonitrile. After purging with nitrogen for 30 mins, 1.3 g of 1, 3-propanesultone (5.5 mol, 1.1 eq) was added to the solution. Then, the reaction was stirred overnight at 40 ˚C. The crude product was purified by column chromatography with DCM to remove the unreacted 1, 3-propanesultone, and DCM/methanol (5:1) to collect the pure product as the white solids (90% isolated yield). ^{1}H NMR and MS spectrum were shown in the Appendix from Figure S30 to S31.

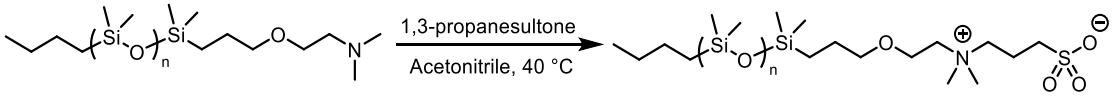

Scheme 2.10 Synthesis of oDMS-$N(CH_3)_2^{(+)}$-$(CH_2)_3$-$SO_3^{(-)}$.

2.3 Characterization

2.3.1 Proton Nuclear Magnetic Resonance (^{1}H NMR) Analysis

^{1}H NMR spectra were recorded on a Bruker-500 MHz NMR spectrometer at 25 ˚C in deuterated chloroform ($CDCl_3$) (7.27 ppm ^{1}H reference) with a relaxation delay of 5 s, the number of scans as 32, and loop counter of 2, unless otherwise noted.

2.3.2 Matrix-assisted Laser Desorption/Ionization Time-of-flight (MALDI-TOF) Mass Spectrometry Measurement

The experiments were conducted at a Bruker MALDI-TOF Autoflex Speed instrument by Dr. Mark Arnould in Center for Nanophase Materials Sciences (CNMS) in Oak Ridge National Laboratory (ORNL). Samples were prepared in chloroform at 10 mg/mL unless already in solution. The matrix was DCTB (trans-2-[3-(4-tert-Butylphenyl)-2-methyl-2-propenylidene]malononitrile) at 60 mg/mL and no salt was added due to the polymer being charged. Aliquots of the solution were mixed in a 20:1 ratio of matrix: analyte and 0.5 μL of the mixture was deposited on the stainless steel target for analysis. The spectra were acquired in the reflectron mode by summing several thousand laser shots into the sum buffer using a laser intensity just above threshold. The absolute molecular weight, polydispersity and end group analysis were performed in Polymerix (Sierra Analytics) software.

2.4 Results and Discussion

^{1}H NMR signals of protons on the chain ends and oDMS backbone were significantly different in chemical shifts due to the dramatic change in chemical environments. Protons on oDMS chains had chemical shifts of 0.1 ppm, and the chemical shifts of C_4H_9 end groups were ranged from 0.5 to 1.7 ppm with four peaks. These signals would not be changed during the reaction because the lack of functionalities and their positions with ratios of integrations can be used as references for calculating the converted end groups. For the side of functional end groups, their signals moved to the direction of down-field regions due to the electronegativity of neighboring oxygens. Thus, the conversion of end groups can be readily monitored during the reactions without the influence of oDMS backbones and other chain ends.

It was found that the esterification with MsCl or OTf_2 and the S_N2 substitution with

CBr_4/PPh_3 or dimethylamine were all highly efficient, as evidenced in the ^1H NMR spectra where the disappearance of the three sets of protons related to hydroxyl chain ends after the reactions. For example, ^1H NMR spectra of starting material and oDMS-*OMs* were compared in Figure 2.2. The protons on the methylene groups of $-CH_2-OH$ and $-CH_2-CH_2-OH$ from starting material showed chemical shifts of 3.7 and 3.6 ppm. On the one hand, these signals shifted to 4.4 and 3.7 ppm after converting to mesylate. On the other hand, the ratio of integrations of protons on methylene groups of $-CH_2-CH_2-O-$ and on methyl groups of mesylate group is 2: 3. The expected signal shifts due to chemical environment changes, the disappearance of signals related to starting materials, and the correct ratio of protons between the backbone and charged chain ends confirmed the successful converting of the hydroxyl group to the mesylate group at the chain ends.

For the esterification with TsCl, 92% of OH groups were converted to tosyl groups. The unreacted oDMS-*OH* can be easily removed by column chromatography. Subsequently, S_N2 reactions between amines and anion precursors on oDMS yield different counter-ions. Both pyridine and *N*-methylmorphine reached quantitative conversion under 90 ˚C, while 1-methylimidazole required 110 ˚C because of different nucleophilicities. Also, the excess amounts of amines can be cleanly removed under high vacuum with heating to produce pure material. For zwitterionic end groups, a sulfobetaine chain end was obtained by ring-opening of 1,3-propanesultone. All resulting ionic oligomers are liquids at 90 ˚C and weak gels at room temperature, while zwitterionic oligomer is solid like gel. The ^1H NMR spectra of oDMS-$Py^{(+)}$-$OMs^{(-)}$ and oDMS-*OMs* anion precursor were compared in Figure 2.3 to explain the success of end group modifications. After mesylate was coordinated with pyridine, the chemical environment near chain ends changed dramatically, resulting in the significant shifts of signals for $-CH_2-N-$ and $-CH_2-CH_2-N-$ from 4.4 and 3.7 ppm to 5.1 and 3.9 ppm, respectively. The protons in pyridine and

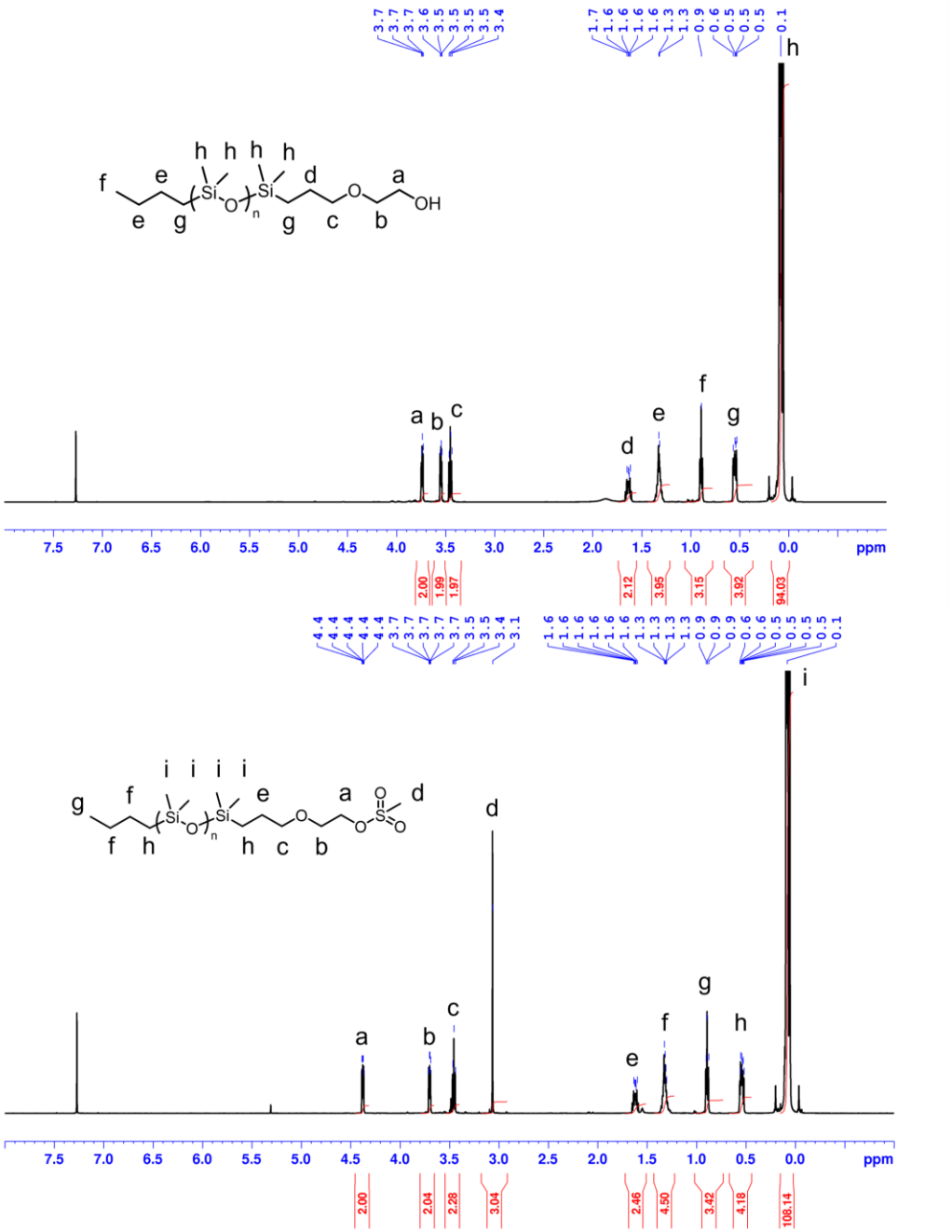

Figure 2.2 Comparison of ^{1}HNMR spectrum of oDMS-*OH* and oDMS-*OMs*.

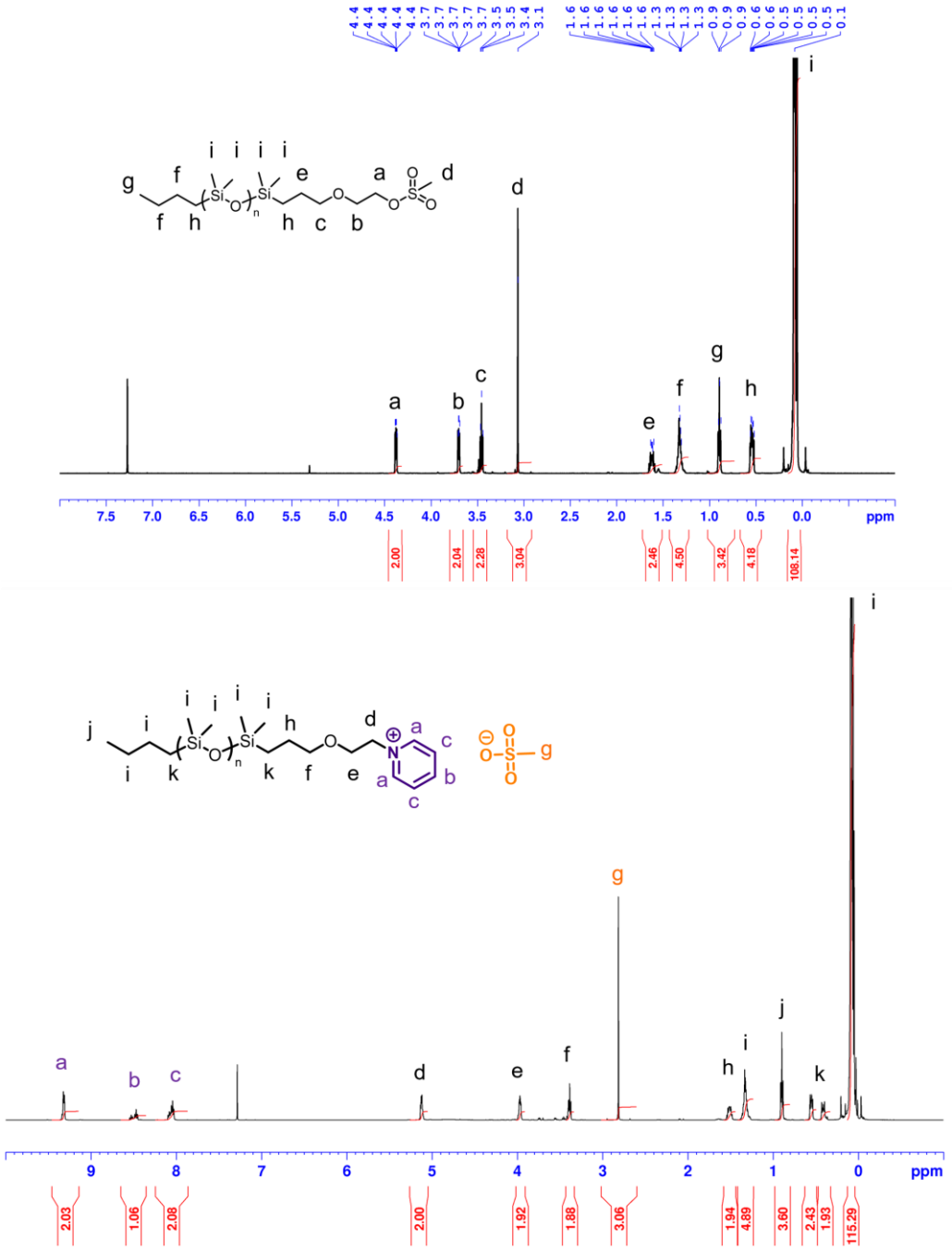

Figure 2.3 Comparison of ^{1}HNMR spectrum of oDMS-*OH* and oDMS-*Py*$^{(+)}$*OMs*$^{(-)}$.

mesylate were highlighted as the purple and yellow colors separately. Based on the ratio of integrations between these colored signals, the chemical structure of charged chain end was confirmed. Furthermore, all peaks were assigned unambiguously to the structure of oDMS-$Py^{(+)}$-$OMs^{(-)}$ with correct chemical shifts and integrations. No other peaks existed on the 1H NMR spectrum, which indicated the high purity of the product.

Interestingly, unlike other end groups, with the end group of $MMP^{(+)}Br^{(-)}$ or $NH(CH_3)_2^{(+)}MeSO_3^{(-)}$, oDMS started to degrade under certain conditions. When applying heating, oDMS- $MMP^{(+)}Br^{(-)}$ was not stable with precipitating of white solids during the reaction, which was also shown in the thermalgravity measurement in the next chapter. In terms of $NH(CH_3)_2^{(+)}MeSO_3^{(-)}$, an excess amount of $MeSO_3H$, which provides an acidic condition, hydrolyzed the siloxane oxygen bonds of oDMS backbone.[14] So, it is critical to add equimolar $MeSO_3H$ and neutralize or remove any possible excess of $MeSO_3H$ after the reaction. However, the sample was still degraded in three days at room temperature.

Furthermore, MALDI-TOF MS was applied to confirm the purity of the obtained amphiphilic oligomer which includes absolute molecular weight, polydispersity, and end group analysis. The MS results are summarized in Table 2.1, and MS spectra were attached in the Appendix. The calculated molecular weights and mass of the end groups were matched with theoretical numbers, indicating the completion of end group modification. For example, oDMS-$Py^{(+)}OMs^{(-)}$ have a molecular weight of 1256 + 174 = 1430 g/mol according to the ^{1}H NMR results, and MALDI TOF MS provided the same result of 1440 g/mol which is well within experimental error. For the end group structural analysis, the theoretical mass of $Si(CH_3)_3(CH_2)_3O(CH_2)_3$-Py is 354.23 Da, and the mass of the end groups calculated from the spectrum is 354.15 Da yielding an exact match with a 80 mDa error. The MALDI MS spectra characterized the polydispersities of

the synthesized samples to be between 1.04 to 1.11 highlighting the fact that the oDMS samples do not degrade during the synthesis.

2.5 Conclusion

A library of oDMS oligomers with different ionic and zwitterionic chain ends was successfully prepared by a metal-free, high-conversion, and scalable method, which was summarized in Figure 2.2. The success of the synthesis work was confirmed by ^{1}H NMR and MALDI-TOF MS. Compared with the starting materials and their precursors, the obtained materials were significantly different in their physical states and this results from replacing just one single chain end.

Table 2.2 Molecular weight information of amphiphilic oligomers from MALDI-TOF MS.

Amphiphilic Oligomers	M_n (g/mol)	M_w (g/mol)	Dispersity
oDMS-*MIM*$^{(+)}$*OMs*$^{(-)}$	1350	1434	1.06
oDMS-*MIM*$^{(+)}$*OTs*$^{(-)}$	1377	1444	1.05
oDMS-*MIM*$^{(+)}$*OTf*$^{(-)}$	1398	1463	1.05
oDMS-*MIM*$^{(+)}$*Br*$^{(-)}$	1296	1381	1.07
oDMS-*Py*$^{(+)}$*OMs*$^{(-)}$	1325	1444	1.09
oDMS-*Py*$^{(+)}$*OTs*$^{(-)}$	1350	1419	1.05
oDMS-*Py*$^{(+)}$*OTf*$^{(-)}$	1541	1636	1.06
oDMS-*Py*$^{(+)}$*Br*$^{(-)}$	1337	1478	1.11
oDMS-*MMP*$^{(+)}$*OMs*$^{(-)}$	1397	1492	1.07
oDMS-*MMP*$^{(+)}$*OTs*$^{(-)}$	1339	1410	1.05
oDMS-*MMP*$^{(+)}$*OTf*$^{(-)}$	1515	1592	1.05
oDMS-*MMP*$^{(+)}$*Br*$^{(-)}$	1443	1557	1.08
oDMS-$N(CH_3)_2^{(+)}$-$(CH_2)_3$-$SO_3^{(-)}$	1730	1803	1.04

References

1. Kim, J.; Jung, H. Y.; Park, M. J., End-group chemistry and junction chemistry in polymer science: Past, present, and future. *Macromolecules* **2020,** *53* (3), 746-763.

2. Grubbs, R. B.; Grubbs, R. H., 50th Anniversary Perspective: Living Polymerization Emphasizing the Molecule in Macromolecules. *Macromolecules* **2017,** *50* (18), 6979-6997.

3. Wuts, P. G.; Greene, T. W., *Greene's protective groups in organic synthesis*. John Wiley & Sons: 2006.

4. Kabalka, G. W.; Varma, M.; Varma, R. S.; Srivastava, P. C.; Knapp Jr, F. F., The tosylation of alcohols. *The Journal of Organic Chemistry* **1986,** *51* (12), 2386-2388.

5. Pásztói, B.; Trötschler, T. M.; Szabó, Á.; Szarka, G.; Kerscher, B.; Mülhaupt, R.; Iván, B., Synthesis of Tosyl-and Nosyl-Ended Polyisobutylenes with High Extent of Functionalities: The Effect of Reaction Conditions. *Polymers* **2020,** *12* (11), 2504.

6. Otte, D. A.; Borchmann, D. E.; Lin, C.; Weck, M.; Woerpel, K., 13C NMR spectroscopy for the quantitative determination of compound ratios and polymer end groups. *Organic letters* **2014,** *16* (6), 1566-1569.

7. Päch, M.; Zehm, D.; Lange, M.; Dambowsky, I.; Weiss, J.; Laschewsky, A., Universal Polymer Analysis by 1H NMR Using Complementary Trimethylsilyl End Groups. *Journal of the American Chemical Society* **2010,** *132* (25), 8757-8765.

8. Stepto, R. F. T., Dispersity in polymer science (IUPAC Recommendations 2009). *Pure and Applied Chemistry* **2009,** *81* (2), 351-353.

9. Chen, H.; He, M.; Pei, J.; Liu, B., End-Group Analysis of Blue Light-Emitting Polymers Using Matrix-Assisted Laser Desorption/Ionization Time-of-Flight Mass Spectrometry. *Analytical Chemistry* **2002,** *74* (24), 6252-6258.

10. Chowdhury, A. U.; Taylor, G. J.; Bocharova, V.; Sacci, R. L.; Luo, Y.; McClintic, W. T.; Ma, Y.-Z.; Sarles, S. A.; Hong, K.; Collier, C. P., Insight into the mechanisms driving the self-assembly of functional interfaces: moving from lipids to charged amphiphilic oligomers. *Journal of the American Chemical Society* **2019,** *142* (1), 290-299.

11. Baughman, T. W.; Sworen, J. C.; Wagener, K. B., The facile preparation of alkenyl metathesis synthons. *Tetrahedron* **2004,** *60* (48), 10943-10948.

12. Zheng, Y.; Zhu, L.; Fan, L.; Zhao, W.; Wang, J.; Hao, X.; Zhu, Y.; Hu, X.; Yuan, Y.; Shao, J.; Wang, W., Synthesis, SAR and pharmacological characterization of novel anthraquinone cation compounds as potential anticancer agents. *European Journal of Medicinal Chemistry* **2017,** *125*, 902-913.

13. Kim, S.; Ye, S.-h.; Adamo, A.; Orizondo, R. A.; Jo, J.; Cho, S. K.; Wagner, W. R., A biostable, anti-fouling zwitterionic polyurethane-urea based on PDMS for use in blood-contacting medical devices. *Journal of Materials Chemistry B* **2020,** *8* (36), 8305-8314.

14. Cypryk, M.; Apeloig, Y., Mechanism of the acid-catalyzed Si− O bond cleavage in siloxanes and siloxanols. A theoretical study. *Organometallics* **2002,** *21* (11), 2165-2175.

CHAPTER 3 EFFECTS OF CHAIN ENDS ON THERMAL PROPERTIES OF CHARGED OLIGOMERS

Abstract

In this chapter, thermal properties of the amphiphilic oligomers with different charged chain ends were measured, including thermal stability represented by thermal degradation temperature (T_d), melting temperature (T_m), and cold crystallization temperature (T_c). T_d was first measured as the guidance for setting the experiment conditions related to thermal processes. Compared with unfunctionalized oDMS-*OH*, all charged chain ends improved their T_ds, except for *MMP* $^{(+)}$*Br*$^{(-)}$, which degraded from the beginning of heating. The relatively good thermal stability of most samples guaranteed their intact after the thermal treatments, including thermal annealing and heating and cooling cycles. Different from observations based on ILs in the literature that cations have a small effect on T_d, both cations and anions tuned the T_ds of end-group functionalized oligomers, influenced by a complex system consisting of nucleophilicities of cations, sizes, and coordination abilities of anions.

Furthermore, although oDMS-*OH* has no T_m and T_c, end groups of *MIM*$^{(+)}$*OTf*$^{(-)}$ and *Py* $^{(+)}$*OTf*$^{(-)}$ gave the functionalized materials these properties, which presented the significant influence of charged chain ends on the thermal properties of end-group functionalized oligomers and the existence of possible ordered structure on oDMS-*MIM*$^{(+)}$*OTf*$^{(-)}$ and oDMS-*Py* $^{(+)}$*OTf*$^{(-)}$. However, the effects of end groups on T_g were not discussed in this work. Because oDMS have an ultra-low T_g, which is lower than the limitation of our available differential scanning calorimeter (DSC).

3.1 Introduction

The good thermal stability with non-flammable nature makes ILs one of the safest solvents for high-temperature applications. Thermal properties are also important as guidelines for the laboratory experiments related to heating, including the upper-temperature limit to prevent thermal degradation and suitable temperatures for thermal annealing and melt processes. As discussed in sections 1.3.1 and 1.4.1, thermal stabilities of ILs have been intensively studied. Some conclusions have been summarized[1]:

(1) The longer n-alkyl chain in cations of $MIM^{(+)}$ results in lower thermal stability, while triazolium ($MPy^{(+)}$) and amino-based cations give some exceptions.[2-4]

(2) The introduction of amine on the alkyl chain of cations decreases the thermal stability of $MIM^{(+)}$ based ILs.[5-7] Hydroxyl groups on the alkyl chain of cations decrease the thermal stability of $MIM^{(+)}NTf_2^{(-)}$, while increasing thermal stability of $MIM^{(+)}Cl^{(-)}$ due to the intramolecular hydrogen bond.[8, 9]

(3) The size and coordination ability of anions affect the thermal stability of ILs with certain rules. For examples, triazolium and azepanium based ILs have the thermal stability of $OTf^{(-)} > OTs^{(-)} > Br^{(-)}$.[10-12]

However, the effect of cations on the thermal stability of ILs is still not clear. Brennecke and coworkers concluded that cations had a small effect on T_d, that these two cations did not alter T_d that much as anions, while coordination ability and size of anions dominated thermal properties. They found $MIM^{(+)} > Py^{(+)}$ in thermal stability of ILs with $Br^{(-)}$ and $Tf_2N^{(-)}$.[13] Mu and coworkers studied the thermal stability of 66 ionic liquids with different anion and cation types. For anions of $BF_4^{(-)}$, *hexafluorophosphate* ($PF_6^{(-)}$), $Tf_2N^{(-)}$, $Cl^{(-)}$ and $Br^{(-)}$, the order of cations was $MIM^{(+)} > Py^{(+)}$ in thermal stability of ILs. However, for *dicyanamide* ($DCA^{(-)}$), the order of cations was *Py*

$^{(+)}$ > $MIM^{(+)}$. In terms of cations, the orders of anions obtained from cations with different types were not identical and even reversed for certain anions.[14]

Based on these complex conclusions, instead of cation or anion itself, cation and anion may work together to affect the thermal stability of ILs. For T_m and T_c, many ILs do not crystallize, but they are glass-form at the temperature range of 188 K and 223 K.[13]

In terms of OILs or OZLs, the effect of charged chain ends on the thermal properties of oligomers has not been explored. A similar phenomenon in thermal properties of ILs may be observed on OILs or OZLs with the same end groups of ILs, while the degree of influence might be lower due to the low percentage of ILs in OILs. Furthermore, with the different connection methods of ions in OILs and OZLs, different thermal properties were expected. To solve these questions, this work studied the thermal properties of a library of oDMS with chain ends consisting of anions and cations varying in characteristics, and details were discussed in this chapter.

3.2 Experimental Part

3.2.1 Characterization of Thermal Stability

Thermogravimetric analysis (TGA) was performed on a TA Instruments Q5000IR at a constant ramp rate of 10 ℃/min up to 700 ℃ under nitrogen flow. The thermal stability of samples, measured by T_d, was determined by the temperature, where 2% of the weight loss of samples was achieved.

3.2.2 Measurement of Glass Transition Temperature, Crystallization, and Melting Temperature

Differential scanning calorimetry (DSC) measurements were performed using TA Instruments calorimeters (Q2000) under nitrogen flow. Approximately 4–6 mg of oligomers with charged chain ends were loaded into aluminum hermetic pans. To remove thermal history, the

samples were first heated to 150 ˚C and then equilibrated for 4 min. A subsequent cool/heat cycle (-80 to 150 ˚C) was measured at 10 ˚C/min for ramp experiments. T_g, T_c, and T_m data presented in the main text were obtained from the second cooling and second heating curves.

3.3 Results and Discussion

The thermal properties of the amphiphilic oligomers were summarized in Table 3.1. T_g was not included in Table 3.1 because it was not detected in the temperature range of measurements. The effect of charged chain ends on thermal properties was discussed by cations and anions, separately.

For thermal stability, a complicated mechanism was involved in the thermal degradation of oDMS with charged chain ends, which was illustrated in Figure 3.1.[15] For the molecular ionic liquid $MIM^{(+)}Br^{(-)}$, the temperature range corresponding to the weight loss was 250 to 350 ℃ which indicating the dissociation of ions. Compared with molecular ionic liquid, oDMS-$MIM^{(+)}Br^{(-)}$ had a much larger temperature range, which was 200 to 500 ℃. In addition, unfunctionalized oDMS had 30% residual weight after the heating, while only 5% of weight remained for oDMS-$MIM^{(+)}Br^{(-)}$. The 30% of residuals for oDMS-*OH* were related to the Si, and it suggested that charged chain ends were able to react with the oDMS backbone at elevated temperatures, which led to lower weight of residuals after heating. Thus, the complicated mechanism was expected, and included degradation of the oDMS backbone, dissociation of ions, and reactions between charged chain ends and backbones.

When the same anion was selected, the order of T_d for different cations was concluded in Table 3.2 and Figure 3.2. Their TGA curves were shown in the Appendix with Figure S32, Figure S33, Figure S34, and Figure S35. Also, the order of T_d for different anions was summarized in Table 3.3 and illustrated in Figure 3.3. Their TGA curves were shown in the Appendix with Figure

Table 3.3 Thermal properties of oDMS-*ILs* and oDMS-*ZW*.

Cation	Anion	T_d (℃)	T_m (℃)	T_c (℃)
oDMS-*OH*		200	/	/
$Py^{(+)}$	$OMs^{(-)}$	232	/	/
	$OTf^{(-)}$	214	-11	-34
	$OTs^{(-)}$	242	/	/
	$Br^{(-)}$	220	/	/
$MIM^{(+)}$	$OMs^{(-)}$	223	/	/
	$OTf^{(-)}$	224	13	-1
	$OTs^{(-)}$	226	/	/
	$Br^{(-)}$	233	/	/
$MMP^{(+)}$	$OMs^{(-)}$	210	/	/
	$OTf^{(-)}$	249	/	/
	$OTs^{(-)}$	220	/	/
	$Br^{(-)}$	187	/	/
Zwitterion				
$N(CH_3)_2^{(+)}$-$(CH_2)_3$-$SO_3^{(-)}$		240	/	/

Table 3.4 The order of T_d with different cations.

Anion	Cation
$OMs^{(-)}$	$Py^{(+)} > MIM^{(+)} > MMP^{(+)}$
$OTs^{(-)}$	$Py^{(+)} > MIM^{(+)} > MMP^{(+)}$
$OTf^{(-)}$	$MMP^{(+)} > MIM^{(+)} > Py^{(+)}$
$Br^{(-)}$	$MIM^{(+)} > Py^{(+)}$

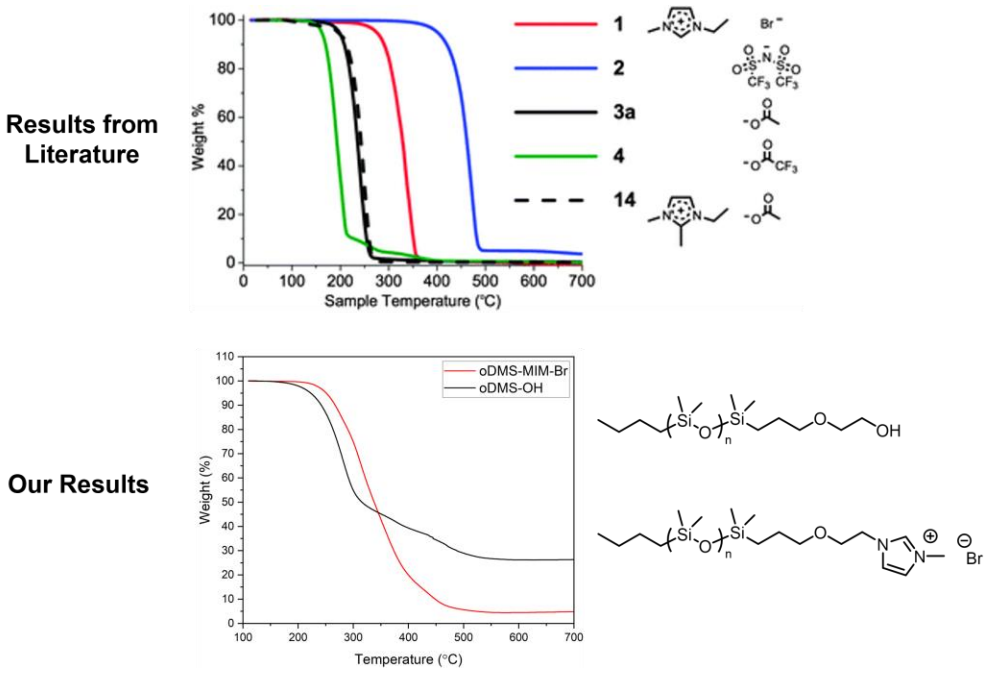

Figure 3.1 Compassion of TGA curves (10 °C/mins) of molecular ionic liquids, unfunctionalized oligomer, and oligomer with charged chain ends. The figure on the top was reprinted with permission from Reference [15]. Copyright 2013 The Royal Society of Chemistry.

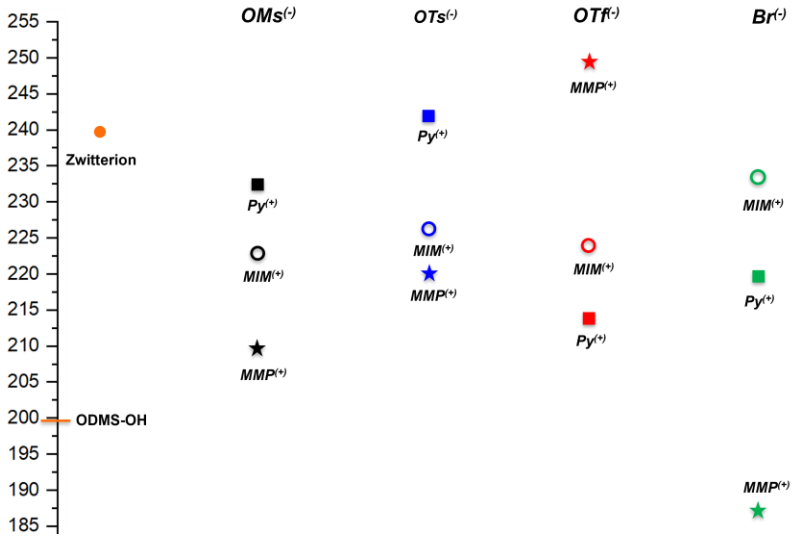

Figure 3.2 The effect of anions on the thermal stability of oDMS with charged chain ends.

Table 3.5 The order of T_d with different anions.

Cation	Anion
$Py^{(+)}$	$OTs^{(-)} > OMs^{(-)} > Br^{(-)} > OTf^{(-)}$
$MIM^{(+)}$	$Br^{(-)} > OTs^{(-)} > OTf^{(-)} > OMs^{(-)}$
$MMP^{(+)}$	$OTf^{(-)} > OTs^{(-)} > OMs^{(-)}$

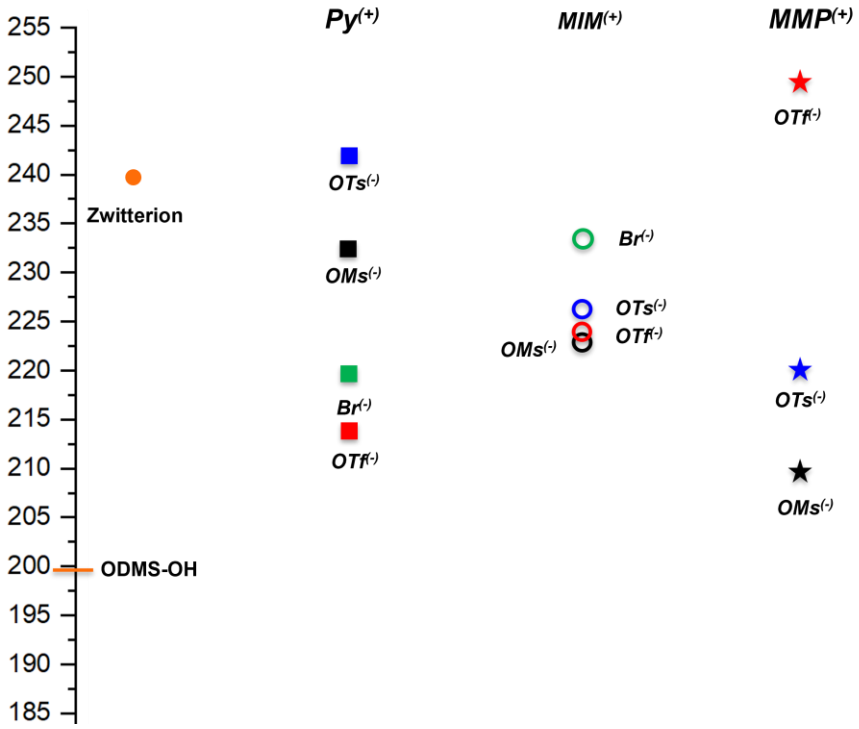

Figure 3.3 The effect of cations on the thermal stability of oDMS with charged chain ends.

S36, Figure S37, and Figure S38. $MMP^{(+)}Br^{(-)}$ was not included in Table 2 and Table 3 because it caused the degradation of oDMS from the very beginning of heating.

Based on Table 3.2, different cations did affect T_d with certain trends. For the same anion, two opposite tendencies were observed that $OMs^{(-)}$ and $OTs^{(-)}$ have the same order of cations, while $OTf^{(-)}$ and $Br^{(-)}$ followed opposite order of cations. For $OMs^{(-)}$ and $OTs^{(-)}$, they had a similar coordination ability while their sizes were different. The order of cation followed the increase of relative basicity of amines. When the anions sit at the extremes on coordination ability, the order of cation was the decrease of relative basicity of amines, which is the same with previous observations in literature based on $Br^{(-)}$ and $Tf_2N^{(-)}$.[14]

However, the order of anions did not follow any tendency when comparing between different cations according to Table 3.3, which was similar to the results from Mu and coworkers. They investigated the thermal stability of ionic liquids of different types of cations and anions. The order of anions for thermal stability was only matched within the cations with similar chemical properties. When different types of cations were introduced, the orders of anions were not able to compare between different cations.[14]

Thus, according to these phenomena of unpredictable trends in the literature and this work from cations or anions with various characteristics, instead of anions or cations themselves, both characteristics of cations and anions worked together to determine T_d with a complicated mechanism on thermal degradation.

As an amorphous oligomer, the unfunctionalized oDMS-OH has no T_c and T_m. Most modified oligomers were also still amorphous, while oDMS-$MIM^{(+)}OTf^{(-)}$ and oDMS-$Py^{(+)}OTf^{(-)}$ became crystallized, which is cohesive with the findings in the literature that $OTf^{(-)}$ and $Tf_2N^{(-)}$ might induce crystallization in ILs.[13, 16] The DSC curves of oDMS-$MIM^{(+)}OTf^{(-)}$ and oDMS-Py

$^{(+)}OTf^{(-)}$ were introduced in Figure 3.4. The DSC curves of oDMS-OH were shown in the Appendix in Figure S39.

3.4 Conclusion

In this chapter, the thermal properties of the library of oDMS oligomers with different ionic and zwitterionic chain ends were studied. The thermal stability of chain-end modified oligomers was improved and was able to tune with the different combinations of cations and anions in the range of 210 ℃ to 242 ℃, except the chain end of *MMP* $^{(+)}Br^{(-)}$ degraded the amphiphilic oligomers from the beginning of heating. Furthermore, thermal stability was influenced by both cations and anions with a complicated degradation mechanism, and the dramatic change of the characteristics of cations or anions altered the observed conclusions. When explaining the effect of cation or anion on thermal stability, the characteristics of cation or anion needed to be specified because each ion behaves different. More effects are needed to further explore effects of ions, instead of anions or cations, the nature of ion pairs may play an important role in the thermal properties of ILs and charged chain-end oligomers. Compared chain ends of ILs with ZWs, ZW significantly improved the thermal stability and almost reached the highest T_d of oligomers with ionic chain ends.

With the single chain end of *MIM* $^{(+)}OTf^{(-)}$ and *Py* $^{(+)}OTf^{(-)}$, the amorphous oligomers were modified with T_c and T_m, which further demonstrated the power of simply chain end modifications on their properties.

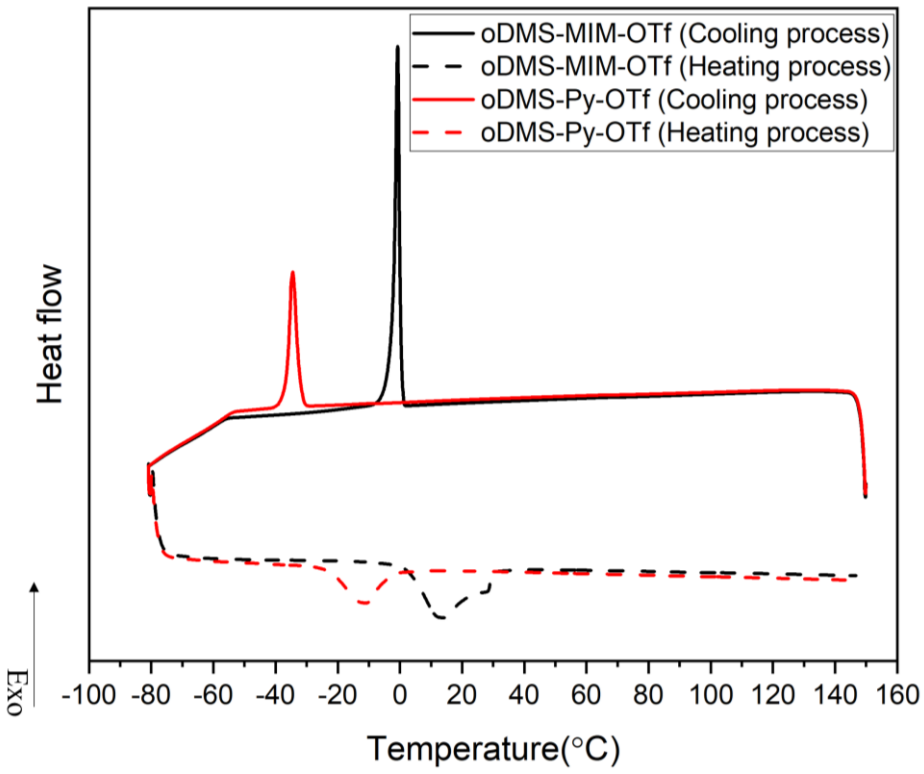

Figure 3.4 Melting and cold crystallization peaks of oDMS-*MIM*$^{(+)}$*OTf*$^{(-)}$ and oDMS-*Py*$^{(+)}$*OTf*$^{(-)}$.

References

1. Xu, C.; Cheng, Z., Thermal stability of ionic liquids: Current status and prospects for future development. *Processes* **2021,** *9* (2), 337.

2. Thomas, E.; Vijayalakshmi, K.; George, B. K., Kinetic stability of imidazolium cations and ionic liquids: a frontier molecular orbital approach. *Journal of Molecular Liquids* **2019,** *276*, 721-727.

3. De La Hoz, A. T.; Brauer, U. G.; Miller, K. M., Physicochemical and Thermal Properties for a Series of 1-Alkyl-4-methyl-1, 2, 4-triazolium Bis (trifluoromethylsulfonyl) imide Ionic Liquids. *The Journal of Physical Chemistry B* **2014,** *118* (33), 9944-9951.

4. Bhattacharyya, S.; Shah, F. U., Thermal stability of choline based amino acid ionic liquids. *Journal of Molecular Liquids* **2018,** *266*, 597-602.

5. Liu, S.; Chen, Y.; Shi, Y.; Sun, H.; Zhou, Z.; Mu, T., Investigations on the thermal stability and decomposition mechanism of an amine-functionalized ionic liquid by TGA, NMR, TG-MS experiments and DFT calculations. *Journal of Molecular Liquids* **2015,** *206*, 95-102.

6. Xue, Z.; Zhang, Y.; Zhou, X.-q.; Cao, Y.; Mu, T., Thermal stabilities and decomposition mechanism of amino- and hydroxyl-functionalized ionic liquids. *Thermochimica Acta* **2014,** *578*, 59-67.

7. Efimova, A.; Pfützner, L.; Schmidt, P., Thermal stability and decomposition mechanism of 1-ethyl-3-methylimidazolium halides. *Thermochimica Acta* **2015,** *604*, 129-136.

8. Krasovskiy, V.; Chernikova, E.; Glukhov, L.; Kapustin, G.; Koroteev, A., Effect of hydroxyl groups in a cation structure on the properties of ionic liquids. *Russian Journal of Physical Chemistry A* **2018,** *92* (12), 2379-2385.

9. Williams, M. L.; Dickmann, J. S.; McCorkill, M. E.; Hassler, J. C.; Kiran, E., The kinetics of thermal decomposition of 1-alkyl-3-methylimidazolium chloride ionic liquids under isothermal and non-isothermal conditions. *Thermochimica Acta* **2020,** *685,* 178509.

10. Al-Sallami, W.; Parsaeian, P.; Neville, A., An appraisal of the thermal decomposition mechanisms of ILs as potential lubricants. *Lubrication Science* **2019,** *31* (6), 229-238.

11. Akçay, A.; Balci, V.; Uzun, A., Structural factors controlling thermal stability of imidazolium ionic liquids with 1-n-butyl-3-methylimidazolium cation on γ-Al2O3. *Thermochimica Acta* **2014,** *589,* 131-136.

12. Makhoukhi, B.; Villemin, D.; Didi, M. A., Synthesis of bisimidazolium–ionic liquids: Characterization, thermal stability and application to bentonite intercalation. *Journal of Taibah University for Science* **2016,** *10* (1), 168-180.

13. Crosthwaite, J. M.; Muldoon, M. J.; Dixon, J. K.; Anderson, J. L.; Brennecke, J. F., Phase transition and decomposition temperatures, heat capacities and viscosities of pyridinium ionic liquids. *The Journal of Chemical Thermodynamics* **2005,** *37* (6), 559-568.

14. Cao, Y.; Mu, T., Comprehensive Investigation on the Thermal Stability of 66 Ionic Liquids by Thermogravimetric Analysis. *Industrial & Engineering Chemistry Research* **2014,** *53* (20), 8651-8664.

15. Clough, M. T.; Geyer, K.; Hunt, P. A.; Mertes, J.; Welton, T., Thermal decomposition of carboxylate ionic liquids: trends and mechanisms. *Physical Chemistry Chemical Physics* **2013,** *15* (47), 20480-20495.

16. Choudhury, A. R.; Winterton, N.; Steiner, A.; Cooper, A. I.; Johnson, K. A., In situ crystallization of ionic liquids with melting points below− 25 C. *CrystEngComm* **2006,** *8* (10), 742-745.

CHAPTER 4 INFLUENCES OF CHAIN ENDS ON PHASE BEHAVIOR IN BULK

Abstract

The introduction of charged chain ends provides unique opportunities for the modification of oligomers, with the possibility to tune their phase separations into ordered structures with high ion conductivities. In this chapter, the phase behavior and ion conductivity of selected oDMS with charged chain ends are explored. Characterized by small-angle X-ray scattering (SAXS), the amphiphilic oligomers were self-assembled into sub-10 nm structures with different morphologies, domain spacings, and order-disorder transition temperatures according to the characteristics of cations and anions on charged chain ends. The incompatibility between oDMS chains and charged chain ends was then analyzed. Compared with anions, cations significantly affect phase behavior. Additionally, oDMS with zwitterionic end groups also formed a well-defined nanostructure.

As discussed in previous sections, the ordered bulk structures correlated with the ionic conductivities. To further prove the phase transition behavior, isotherms of permittivity and ion conductivity vs. frequency were measured by dielectric spectroscopy (DS). Compared with SAXS, which measured macroscopic information, DS proved that phase transition occurred within the same morphology for several samples. Influences of cations, anions, and zwitterion on the ion conductivity were then correlated and compared. Interestingly, a jump point was found in the relationship between ion conductivity and temperature for charged chain ends of zwitterion or with the anion of bromide, which indicated the complex relationship between the degree of order of internal structure, characteristics of ions, and ion conductivities.

4.1 Introduction

Microphase separation of block copolymers has made these materials the subject of intense scientific study and commercial applications due to the precise structures with different scales.[1]

Based on previous studies, the incompatibility leads to the microphase separation into various morphologies in bulk as a function of block composition, which is shown in Figure 4.1.[2]

To support the growing needs in the microelectronics industry, which needs smaller nanostructures to achieve higher on-chip density but facing challenges in photolithography, high χ block polymers have been developed to fabricate sub-10 nm or even smaller nanofeatures. High χ, where χ is the Flory-Huggins interaction parameter, means the blocks are highly incompatible. Meanwhile, low N needs a low degree of polymerization, that is, a low molecular weight. Strong segregation theory predicts that $d \approx bN^{2/3}\chi^{1/6}$, where d is lamellar domain spacing, b is the statistical segment length. Based on Mean-field theory that $\chi N > 10.5$ is required to produce an ordered structure for a symmetric AB diblock copolymer ($f_A = f_B = 0.5$). Then, the maximum value for b is 1 nm for a flexible polymer. With the above assumptions, the relationship of d is simplified as $d \geq 5\chi^{-1/2}$ nm. With this relationship, it is evident that the higher χ gives a lower d. The smallest feature estimated with the application of high χ block copolymers is 2 nm.[3] At this length scale, N is as low as 10 and the molecules are co-oligomers instead of block copolymers.

Among diverse types of oligomers, oligo(dimethylsiloxane) (oDMS) has found wide promise in self-assembly when combined with different monomers due to their high-χ values, and it is also an attractive etch mask. Meijer and co-workers synthesized oDMS-b-oLA, and the block co-oligomer can form cylinder or lamellar morphologies depending on the compositions.[4] Bates and Hawker with co-works studied the dispersity effect on self-assembly of oDMS-b-oMMA block co-oligomers.[5] The category was further expanded from block co-oligomers to functionalized oDMS oligomers. Alegria and coworkers studied the oDMS oligomers with monocarboxydecyl chain ends to fabricate the sub-10 nm structure dependent on temperature.[6]

Schenning and co-workers introduced azobenzene into the middle and end of oDMS oligomer

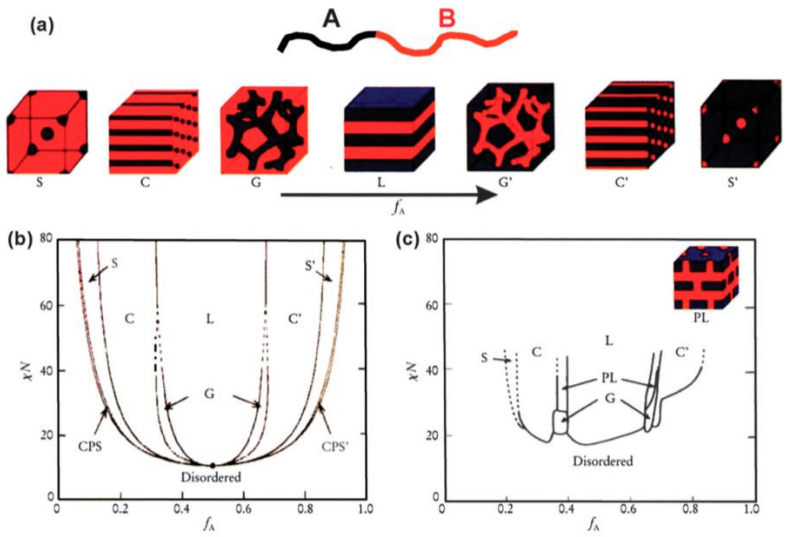

Figure 4.1 (a) Equilibrium morphologies in bulk of AB diblock copolymers: S and S' = body-centered-cubic spheres, C and C' = hexagonally packed cylinders, G and G' = bicontinuous gyroids, and L = lamellae. (b) Theoretical phase diagram of AB diblocks predicted by the self-consistent mean-field theory, depending on the volume fraction (f) of the blocks and the segregation parameter, χN ; CPS and CPS' = closely packed spheres. (c) Experimental phase diagram of polystyrene-b-polyisoprene copolymers, in which $f_A$represents the volume fraction of polyisoprene, PL = perforated lamellae. Reprinted with permission from Reference [2]. Copyright 2012 The Royal Society of Chemistry.

chain. Both modified oligomers form sub-5 nm features by stimulating with light.[7, 8] Meijer and co-workers designed oDMS oligomers with two ends capped by azobenzene, whose the π–π stacking interactions lead to form ordered lamellar phases.[9] These previous works again have enlightened the importance of end groups on the self-assembly behavior of and reviewed recently by Park and co-works, which is shown in Figure 4.2.[10]

To resemble high χ block copolymers and the natural lipid, hydrophilic charged chain ends, including ionic and zwitterionic groups, were introduced to chain ends of hydrophobic oDMS. Based on the incompatibility of charged chain ends and oDMS backbones, the resulting amphiphilic oligomers are expected to self-assemble in bulk. In addition, conductivity was introduced to the amphiphilic oligomers by charged chain ends. The phase behaviors and ion conductivities of obtained materials were characterized by SAXS and DS to understand the effect of cations, anions, and zwitterion. The complex relationship between the degree of order of internal structure, ion conductivity, and characteristics of ions was discussed in the following sections.

4.2 Experimental Part

4.2.1 Fabrication of Thin Films of End-group Functionalized oDMS

The solvent casting method was applied to obtain thin films with end-group functionalized oDMS. Amphiphilic oligomers were dried at 90 ℃ under high vacuum, and then a 1% solution of oDMS oligomers was slowly dried on the substrate. After drying the solvent, the films were ready for the following measurements.

4.2.2 Measurement of Nanostructures on Thin Films by Small-angle X-ray Scattering (SAXS)

The SAXS measurements were conducted at BL23A1 and TPS 25A in National Synchrotron Radiation Research Center and performed by our collaborators, Bokai Wang, Dr. Yu-Xian Lin, Dr. C.-H. Lin, and Prof. Hsin-Lung Chen in the Department of Chemical Engineering at National

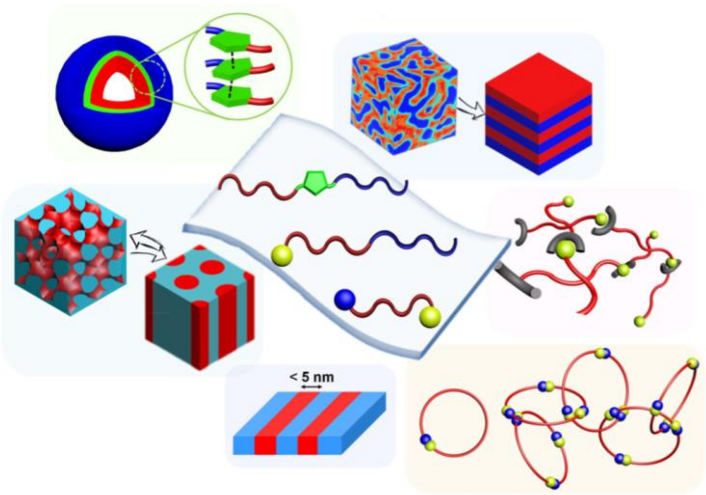

Figure 4.2 Schematic representative of end-functionalized polymers with tuning morphology, intermolecular interactions, and properties. Reprinted with permission from Reference [10]. Copyright 2020 American Chemical Society.

Tsing Hua University.

4.2.3 Analysis of Ion Conductivity by Dielectric Spectroscopy (DS)

Broadband dielectric measurements with a Novocontrol Concept 40 system were conducted in the frequency range of $1 - 10^7\ Hz$. The Novocontrol Concept 40 system includes a ZGS active sample cell interface, an Alpha-A impedance analyzer, and a Quatro Cryosystem temperature control unit. A Teflon spacer was used to separate two gold-plated electrodes, and the amphiphilic oligomers were placed and then lightly pressed. The experiments were performed from room temperature to high temperatures and then cooled to room temperature ($293 - 403 - 293\ K$). The samples were equilibrated for at least 5 minutes at each temperature before conducting dielectric measurements.

4.3 Results and Discussion

The ordered structures of amphiphilic oDMS were measured by SAXS and DS. With SAXS, the morphologies, domain spacing, and T_{ODT}s were analyzed. Combined with DS, the phase transition behaviors and T_{ODT}s were further confirmed. In addition, ion conductivities of oligomers with charged chain ends were measured. All the above parameters were related to the characteristics of charged chain ends, and the incompatibility between charged chain ends and the oDMS tails. More details will be discussed in the following sections.

4.3.1 Analysis of Domain Spacing, Morphology, and Order-disorder Transition Temperature (T_{ODT}) of Nanostructure by SAXS

For the amphiphilic oligomers with ordered structures, their SAXS peaks were composed of narrow, sharp peaks representing ordered phases and board peaks standing for disordered phases. Compared with board peaks, the low percentages of sharp peaks were correlated with the low weight fractions of charged chain ends in the total weights of amphiphilic oligomers, which were

summarized in Table 4.1. As discussed in section 1.5.1, based on the positions of peaks and position of 1st order peak of SAXS profiles, the morphologies and domain spacing were calculated. In addition, with the disappearance or formation of narrow peaks during temperature changes, T_{ODT}s were obtained. The highest temperature which SAXS reached was 110 ℃. Thus, T_{ODT} > 110 ℃ represented that was T_{ODT} not detected in the temperature range of SAXS measurements. All the results were summarized in Table 4.2. (HEX: Hexagonally packed IL cylinders; LAM: lamellar structures)

The SAXS profile of each sample was discussed next. For the pyridinium-based chain ends, Figure 4.3 showed the SAXS profile of oDMS-*Py* $^{(+)}Br^{(-)}$. The relative peak positions of $q_1 : q_2 : q_3 = 1 : \sqrt{3} : 2$ offered a HEX structure which was marked in Figure 4.3. The narrow peaks that disappeared under heating between 100 to 110 ℃ suggested that T_{ODT} was ranged here. In addition, the ordered structure was able to recover from the disordered state under cooling. The SAXS profile of oDMS-*Py* $^{(+)}OMs^{(-)}$ was then shown in Figure 4.4. With the change of the anions, the morphology of oDMS-*Py* $^{(+)}OMs^{(-)}$ was tuned to LAM structure. No order-disorder transition was observed in the temperature range of measurements. The larger fraction of broad peaks in SAXS profiles of oDMS-*Py* $^{(+)}Br^{(-)}$ and oDMS-*Py* $^{(+)}OMs^{(-)}$in the cooling process than that of in the heating process because the cooling rate was much faster than the heating rate.

For chain ends of imidazolium-based ionic liquid, the SAXS profile of oDMS-*MIM* $^{(+)}Br^{(-)}$ was illustrated in Figure 4.5. A HEX phase was observed according to the relative peak positions marked in Figure 4.5, and T_{ODT} of 70 to 80 ℃ was only observed upon heating with no structure recovery during cooling. Similarly, oDMS-*MIM* $^{(+)}OMs^{(-)}$. which was shown in Figure 4.6, also had the HEX structure, while T_{ODT} was a little bit lower as 60 to 70 ℃ with no structure recovery during cooling. In terms of morpholine-based chain ends, the SAXS profile of oDMS-*MMP*

Table 4.1 Weight fractions of charged chain ends.

Amphiphilic Oligomers	M_w (g/mol)	Molecular weight of charge chain ends (g/mol)	Weight fraction of charge chain ends (%)
oDMS-$MIM^{(+)}OMs^{(-)}$	1434	177.2	12.4
oDMS-$MIM^{(+)}Br^{(-)}$	1381	162.01	11.7
oDMS-$Py^{(+)}OMs^{(-)}$	1444	174.19	12.1
oDMS-$Py^{(+)}Br^{(-)}$	1478	159.01	10.8
oDMS-$MMP^{(+)}OMs^{(-)}$	1492	196.24	13.2
oDMS-$N(CH_3)_2^{(+)}$-$(CH_2)_3$-$SO_3^{(-)}$	1803	1.04	9.2

Table 4.2 Phase structures of oDMS-*ILs* and oDMS-*ZW* based on SAXS measurements.

Cation	**Anion**	**Morphology**	**Domain spacing (nm)**	T_{ODT} **(℃)**
oDMS-*OH*		/	/	/
$Py^{(+)}$	$OMs^{(-)}$	LAM	7.80	>110
	$Br^{(-)}$	HEX	6.23	100~110
$MIM^{(+)}$	$OMs^{(-)}$	HEX	6.04	60~70
	$Br^{(-)}$	HEX	6.31	65~70
$MMP^{(+)}$	$OMs^{(-)}$	LAM	8.34	>110
Zwitterion				
$N(CH_3)_2^{(+)}$-$(CH_2)_3$-$SO_3^{(-)}$		HEX	6.33	>110

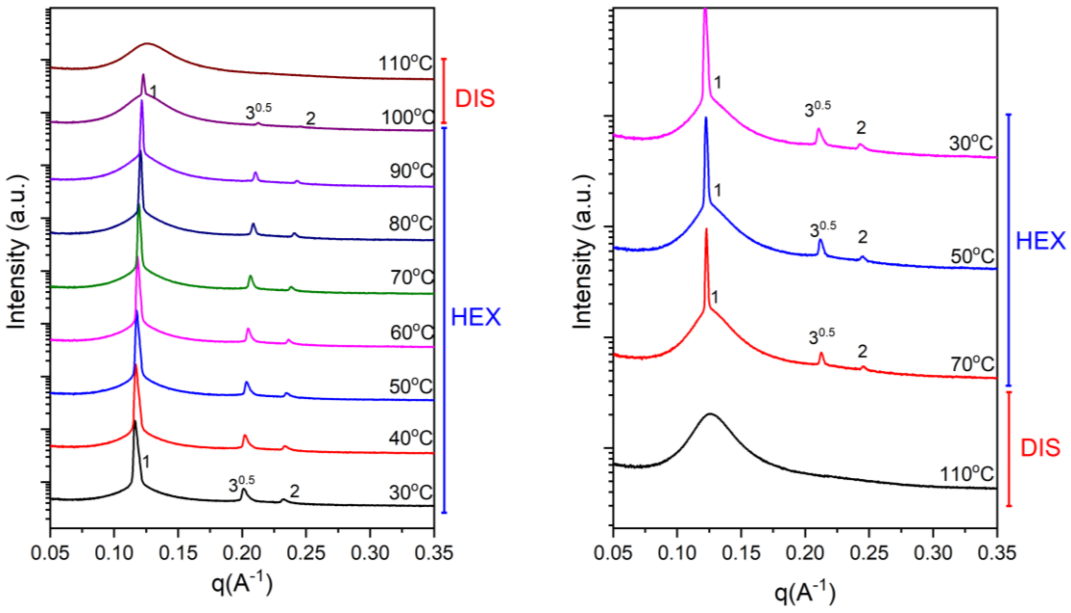

Figure 4.3 SAXS profile of oDMS-*Py*$^{(+)}$*Br*$^{(-)}$ under heating (left) and cooling processes (right).

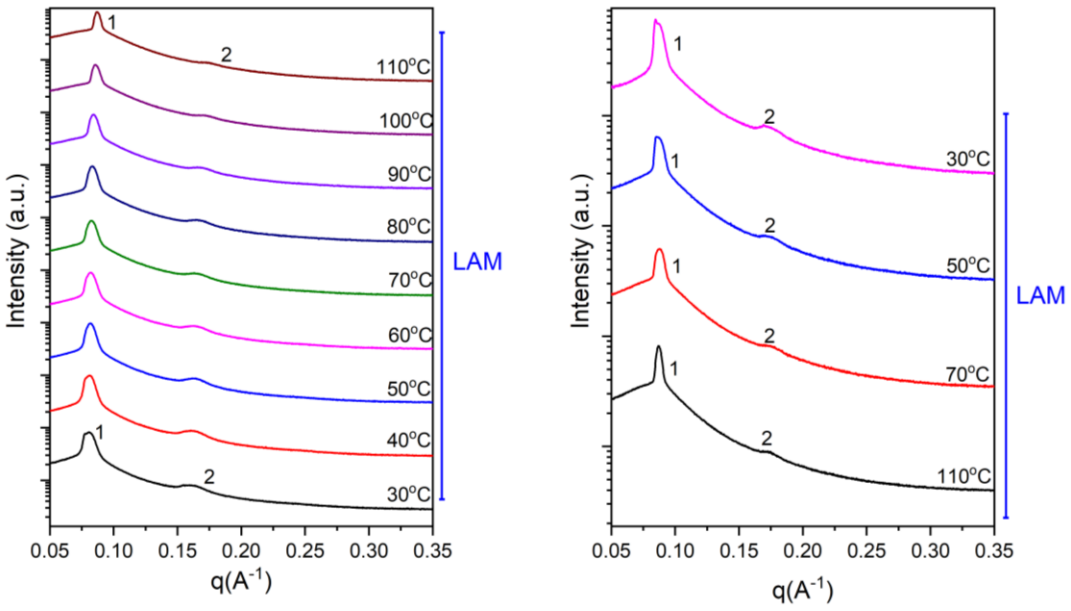

Figure 4.4 SAXS profile of oDMS-*Py*$^{(+)}$*OMs*$^{(-)}$ under heating (left) and cooling processes (right).

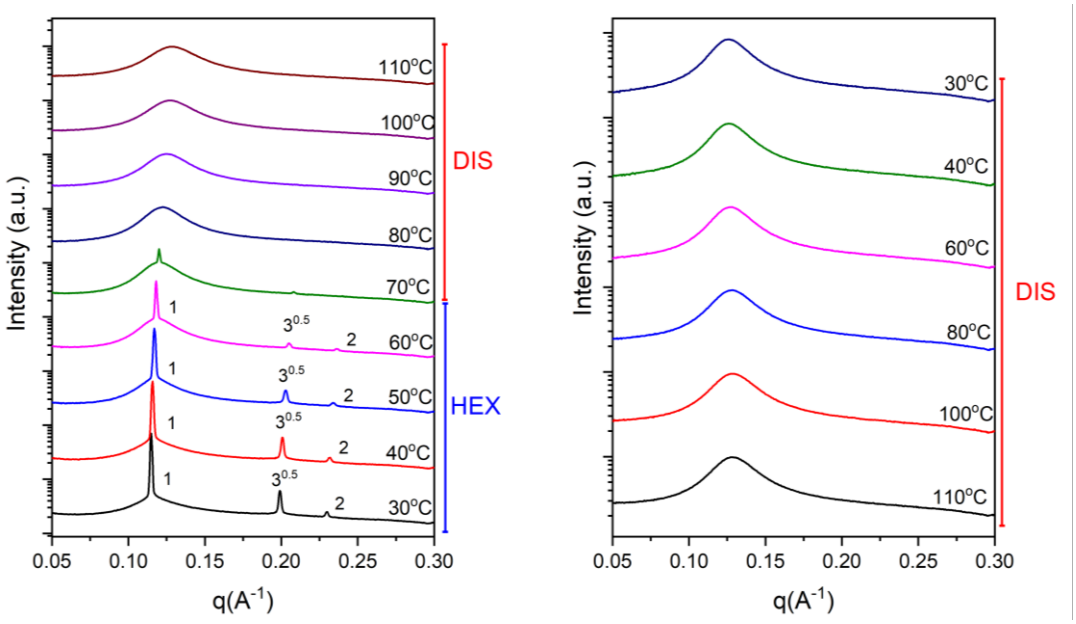

Figure 4.5 SAXS profile of oDMS-*MIM* $^{(+)}$*Br*$^{(-)}$ under heating (left) and cooling processes (right).

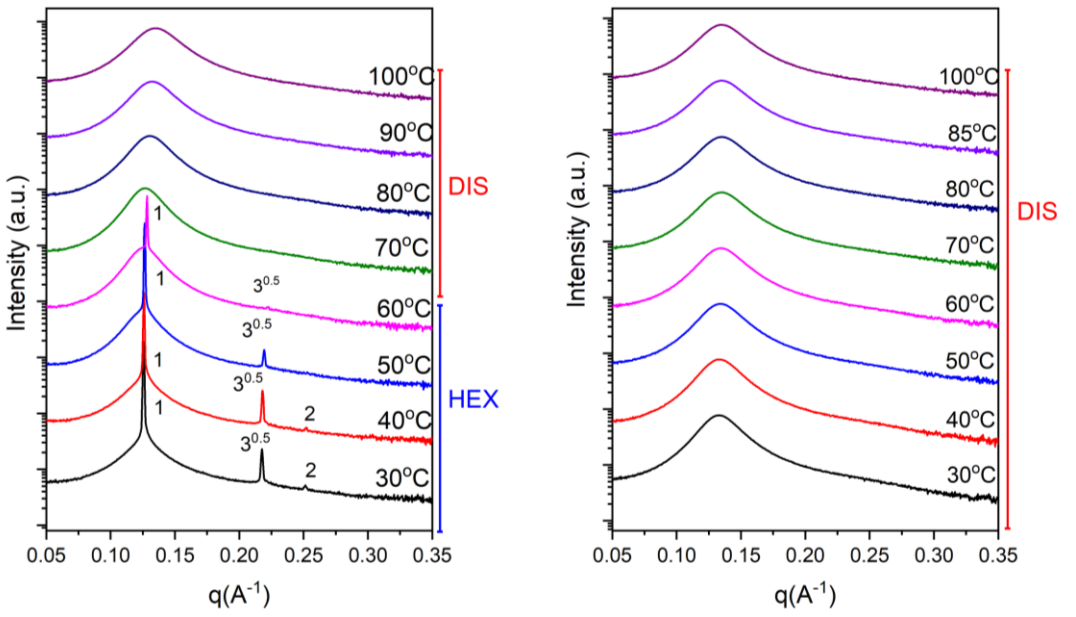

Figure 4.6 SAXS profile of oDMS-*MIM* $^{(+)}$*OMs*$^{(-)}$ under heating (left) and cooling processes (right).

$^{(+)}OMs^{(-)}$ was illustrated in Figure 4.7. The relative positions of peaks provided information on LAM phase. Also, no order-disorder transition was observed in the temperature range of experiments.

For zwitterionic chain ends, the SAXS profile of oDMS-$N(CH_3)_2^{(+)}$-$(CH_2)_3$-$SO_3^{(-)}$ was shown in Figure 4.8, showing the HEX structure without the order-disorder transition.

In summary, amphiphilic oligomers were able to form LAM or HEX morphologies with different domain spacings from 6.04 nm to 8.34 nm, and order-disorder transition temperatures ranged from 60 ℃ to a temperature larger than 100 ℃ (higher than the temperature range of SAXS measurements). The various phase behaviors were dictated by the characteristics of cations and anions.

4.3.2 Study of Phase Transition Behavior and Order-disorder Transition Temperature (T_{ODT}) by Dielectric Spectroscopy (DS)

Confirmation of the phase transition behavior was needed using a different methodology. In this instance, dielectric spectroscopy (DS) was chosen to confirm the behavior. Based on the discussion in section 1.5.2, the isotherms of ion conductivity (σ') vs. frequency (f') and the permittivity (ε') vs. frequency (f') were able to provide the needed information. T_{ODT}s measured by DS were summarized in Table 4.3, and the Figures of isotherms for each sample were discussed next. Colors of rainbows were used to show the temperature changes where dark colors represented low temperatures and colors near red stood for high temperatures. For example, the black color is the lowest temperature (room temperature), while the red color is the highest temperature which is 130 ℃. The chain ends and their corresponding Figures' names were listed in Table 4.4 for the convenience of reading due to the large amounts of Figures.

With the pyridinium based chain ends, oDMS-$Py^{(+)}Br^{(-)}$ showed an obvious transition on

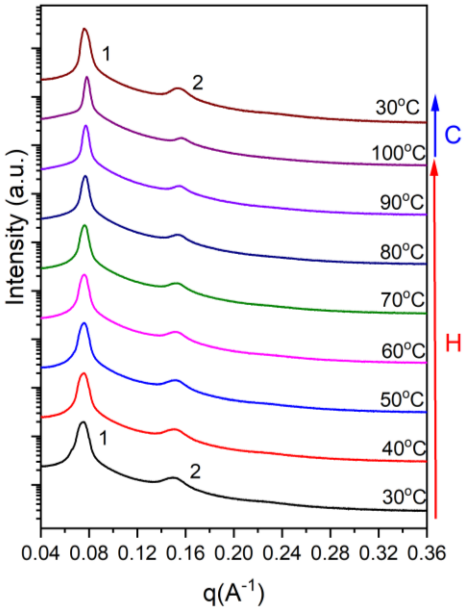

Figure 4.7 SAXS profile of oDMS-*MMP* $^{(+)}$*OMs*$^{(-)}$ under heating and cooling processes.

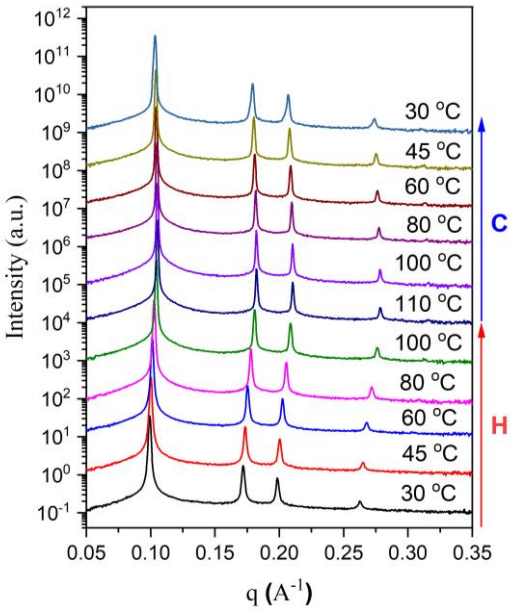

Figure 4.8 SAXS profile of oDMS-$N(CH_3)_2^{(+)}$-$(CH_2)_3$-$SO_3^{(-)}$ under heating and cooling processes.

both isotherms of σ' vs. f' and ε' vs. f'. In Figure 4.9, starting from room temperature, which was the black curve, the shape of the curves of σ' was the polyline with two non-zero slopes, which suggested the existence of an ordered structure due to the movement of ions being restricted by ordered structures. The values of σ' were then increased with each increased temperature due to the increase of mobility of ions, but the shape of curves was still similar because the movement of ions was still in the same order structures (black to green colored curves). However, when the temperature reached 95 ℃, ion conductivity started to drop. Also, a significant gap between curves was observed between 95~100 ℃. Furthermore, a long plateau was formed at 100 ℃. This plateau is called the DC plateau, which showed a disordered structure because ions were able to diffuse freely with long-range order of movements. Thus, T_{ODT} during heating was 95~100 ℃, determined by the appearance of the plateau. On the other hand, the transition was also confirmed by isotherms of ε' vs. f'. In Figure 4.10, the values of ε' were slightly increased at each elevated temperature without the shape change of curves due to the existence of ordered structures (black to green curves). At 95 ℃, the permittivity started to decrease. Also, the remarkable gap between curves appeared again between 95~100 ℃, which suggested the decrease in the degree of order of internal structure. Thus, the same transition temperature was found as 95~100 ℃. In terms of the cooling process, the same transition occurred for both isotherms of σ' vs. f' and ε' vs. f' with the reversed order in Figure 4.11 and Figure 4.12, which proved that the order-disorder transition is reversible.

After exchanging the anion to $OMs^{(-)}$, isotherms of oDMS-$Py^{(+)}OMs^{(-)}$ for σ' vs. f' and ε' vs. f' during the heating process are shown in Figure 4.13 and Figure 4.14, then Figure 4.15 and Figure 4.16 as the cooling process, respectively. In Figure 4.13, the approximately linear curve with non-zero slopes of σ' vs. f' at room temperature (black colored curve) suggested the

Table 4.3 T_{ODT}s of oDMS-*ILs* and oDMS-*ZW* based on DS measurements.

Cation	Anion	T_{ODT} (°C) Heating Cycles	T_{ODT} (°C) Cooling Cycles
$Py^{(+)}$	$OMs^{(-)}$	Weak transition ~ 65	Weak transition ~ 65
	$Br^{(-)}$	95~100	100~105
$MIM^{(+)}$	$OMs^{(-)}$	60~70	60~70
	$Br^{(-)}$	50~55	55~60
	$OTs^{(-)}$	Not detected	Not detected
	$OTf^{(-)}$	Not detected	Not detected
$MMP^{(+)}$	$OMs^{(-)}$	Weak transition ~ 65	Weak transition ~ 65
Zwitterion			
$N(CH_3)_2^{(+)}$-$(CH_2)_3$-$SO_3^{(-)}$		~110	~125

Table 4.4 Figure names of tested samples.

Cation	Anion	Isotherms of σ' vs. f' (Heating)	Isotherms of σ' vs. f' (Cooling)	Isotherms of ε' vs. f' (Heating)	Isotherms of ε' vs. f' (Cooling)
$Py^{(+)}$	$Br^{(-)}$	Figure 4.9	Figure 4.11	Figure 4.10	Figure 4.12
	$OMs^{(-)}$	Figure 4.13	Figure 4.15	Figure 4.14	Figure 4.16
$MIM^{(+)}$	$Br^{(-)}$	Figure 4.17	Figure 4.19	Figure 4.18	Figure 4.20
	$OMs^{(-)}$	Figure 4.21	Figure 4.23	Figure 4.22	Figure 4.24
	$OTs^{(-)}$	Figure 4.25	Figure 4.27	Figure 4.26	Figure 4.28
	$OTf^{(-)}$	Figure 4.29	Figure 4.31	Figure 4.30	Figure 4.32
$MMP^{(+)}$	$OMs^{(-)}$	Figure 4.33	Figure 4.35	Figure 4.34	Figure 4.36
Zwitterion					
$N(CH_3)_2^{(+)}$-$(CH_2)_3$-$SO_3^{(-)}$		Figure 4.37	Figure 4.39	Figure 4.38	Figure 4.40

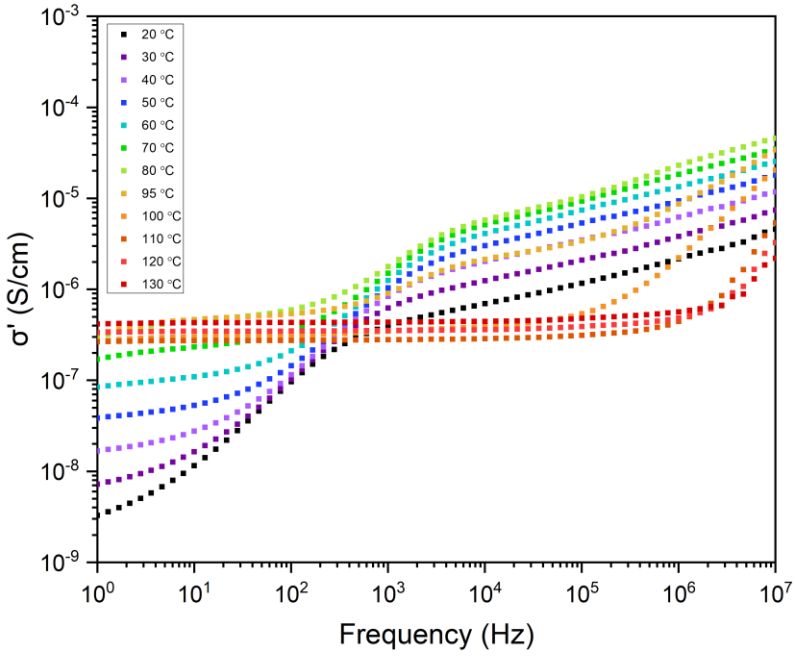

Figure 4.9 The isotherms of ion conductivity vs. frequency of oDMS-*Py*$^{(+)}$*Br*$^{(-)}$ (Heating process).

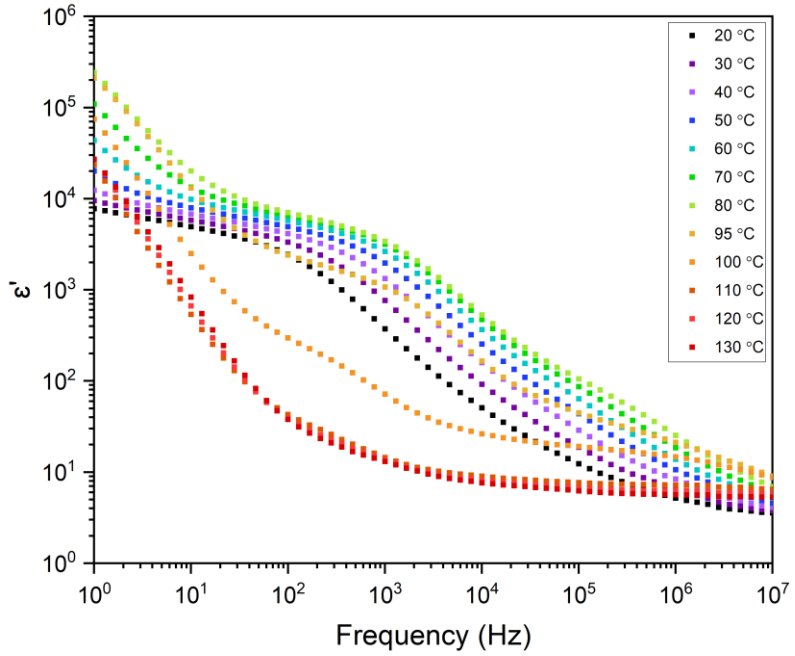

Figure 4.10 The isotherms of permittivity vs. frequency of oDMS-*Py*$^{(+)}$*Br*$^{(-)}$ (Heating process).

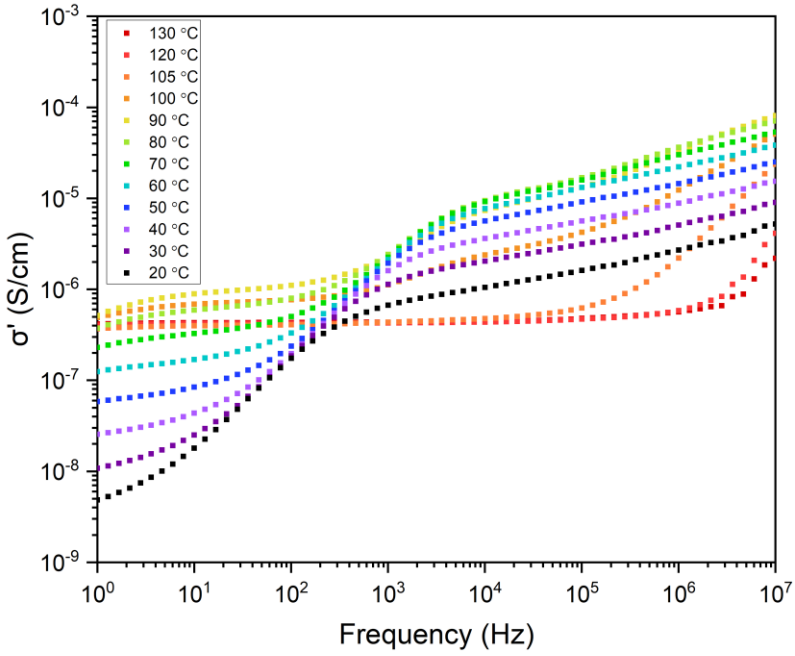

Figure 4.11 The isotherms of ion conductivity vs. frequency of oDMS-$Py^{(+)}Br^{(-)}$ (Cooling process).

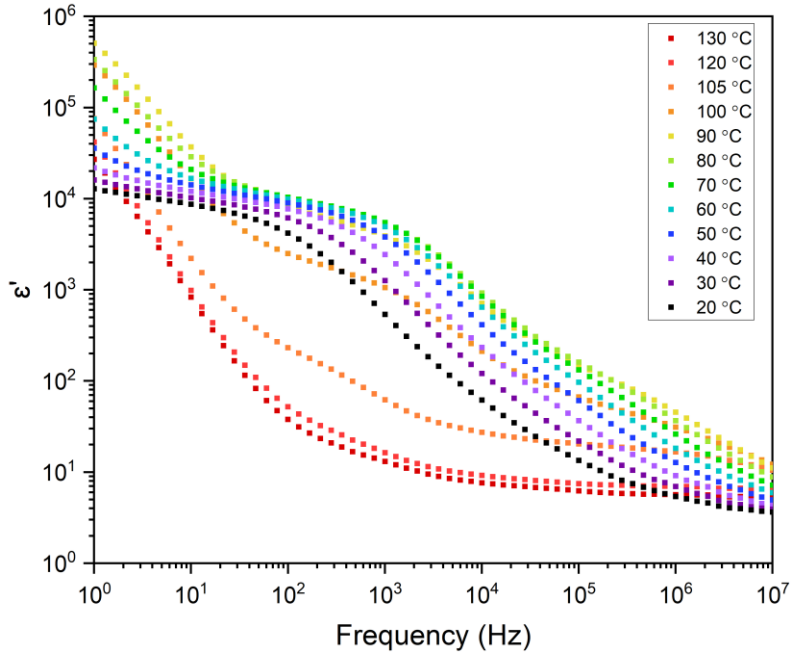

Figure 4.12 The isotherms of permittivity vs. frequency of oDMS-$Py^{(+)}Br^{(-)}$ (Cooling process).

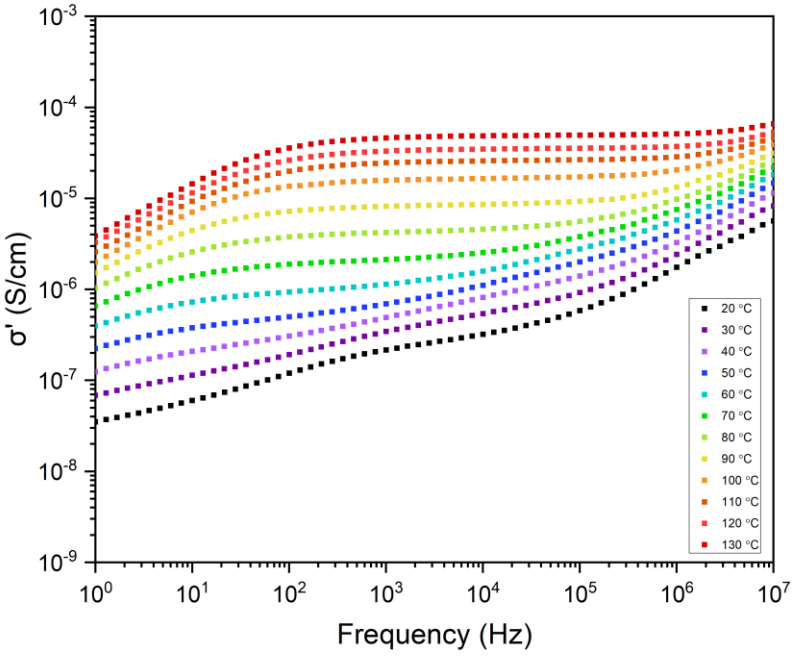

Figure 4.13 The isotherms of ion conductivity vs. frequency of oDMS-*Py* $^{(+)}$*OMs*$^{(-)}$ (Heating process).

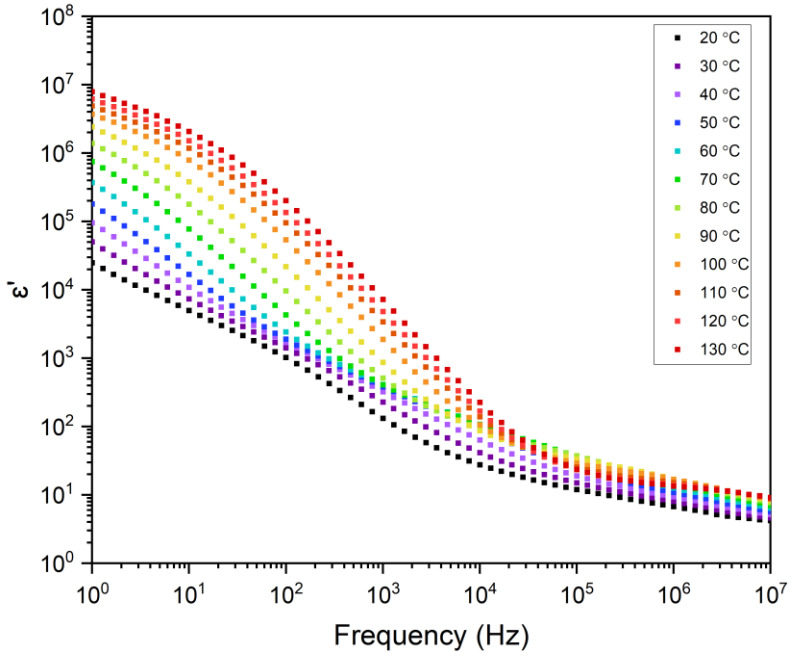

Figure 4.14 The isotherms of permittivity vs. frequency of oDMS-*Py* $^{(+)}$*OMs*$^{(-)}$ (Heating process).

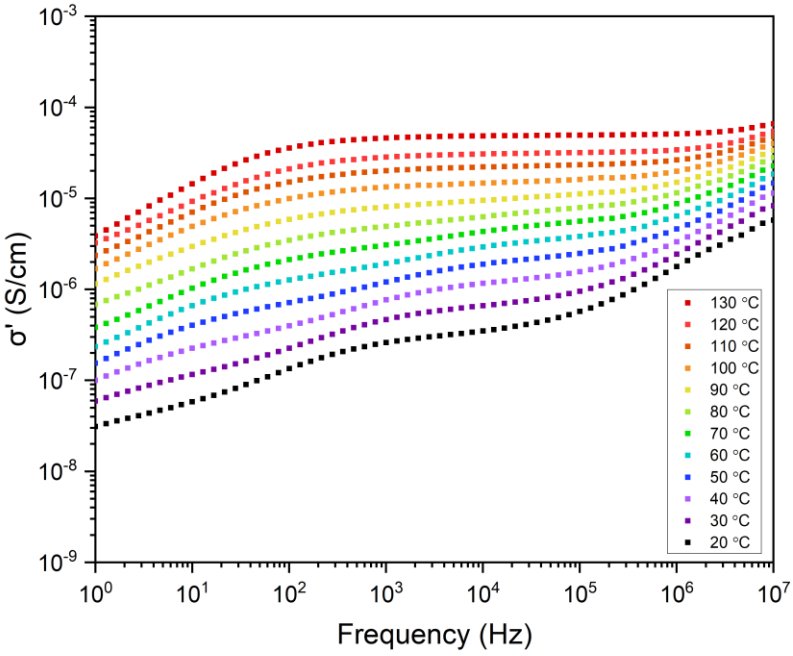

Figure 4.15 The isotherms of ion conductivity vs. frequency of oDMS-*Py* $^{(+)}$*OMs*$^{(-)}$ (Cooling process).

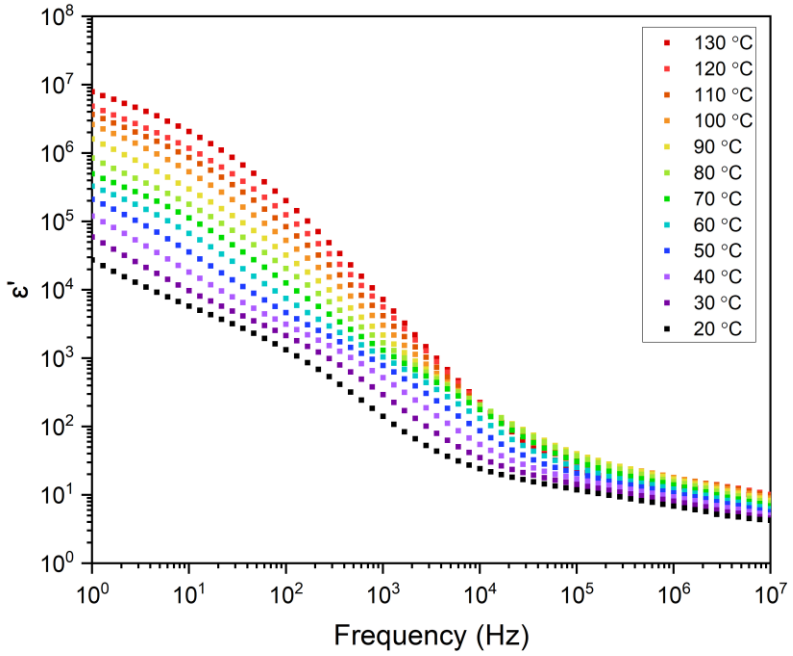

Figure 4.16 The isotherms of permittivity vs. frequency of oDMS-*Py* $^{(+)}$*OMs*$^{(-)}$ (Cooling process).

existence of the ordered structure. With the increase of temperature, the values of σ' were increased. After heating to 65 ℃, a plateau (the DC plateau) started to form on the green-blue colored curve from 10^1 to 10^4 Hz. Then, the plateau became longer and extended from 10^3 to 10^7 Hz with the increase of temperatures, which suggested the disappearance of the ordered structure. Thus, the transition occurred at 65 ℃. For ε', black to blue colored curves followed the similar slopes between $1\sim10^4$ Hz before 65 ℃, while the slope of the curve (blue-green color) started to increase from 65 ℃ in Figure 4.14, which suggested the transition occurred at 65 ℃. A similar behavior was also observed in the cooling cycles in Figure 4.15 and Figure 4.16.

For oligomers with chain ends of imidazolium-based ILs, four different anions were studied:

(1) The anion of $Br^{(-)}$ gave a clear change of curves in both isotherms of σ' vs. f' and ε' vs. f'., the σ' vs. f' was an approximately linear line (black to blue curves) in Figure 4.17. As increasing temperatures, the DC plateau appeared at 50 ℃ (light blue curve), which offered T_{ODT} as 50~55 ℃. For ε' in Figure 4.18, a T_{ODT} was observed by dramatically drops of ε' (blue to light-blue curves). In terms of cooling cycles, T_{ODT} was indicated by the similar transitions of curves but slightly different as 55~60 ℃ in Figure 4.19 and Figure 4.20.

(2) When exchanging the anion to $OMs^{(-)}$, the curve of σ' vs. f' at room temperature gave no DC plateau suggesting the order structure existed at ambient temperature (black curve) in Figure 4.21. The DC plateau appeared at 65 ℃ (blue-green colored curve), offering the T_{ODT} as 60~65 ℃. In Figure 4.22, the slopes of curves of ε' vs. f' started to diverge from 60~70 ℃, which provided a similar T_{ODT} as σ'. For the cooling process, as shown in Figure 4.23 and Figure 4.24, the same T_{ODT} was observed with the same but reversed tendency.

(3) After changing the anion to $OTs^{(-)}$ or $OTf^{(-)}$, no transition was observed in the isotherms σ' vs. f' and ε' vs. f' under heating and cooling cycles, which were illustrated in Figure 4.25,

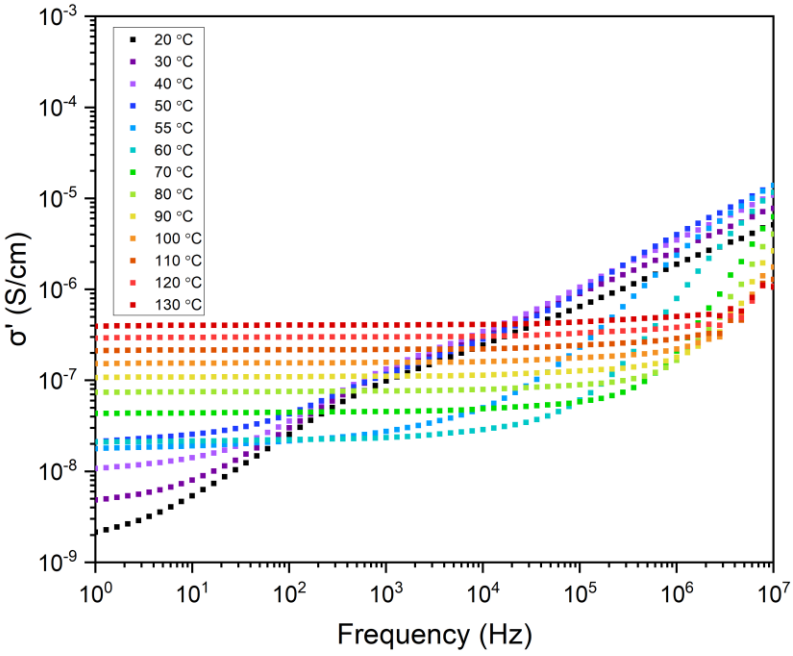

Figure 4.17 The isotherms of ion conductivity vs. frequency of oDMS-*MIM* $^{(+)}Br^{(-)}$ (Heating process).

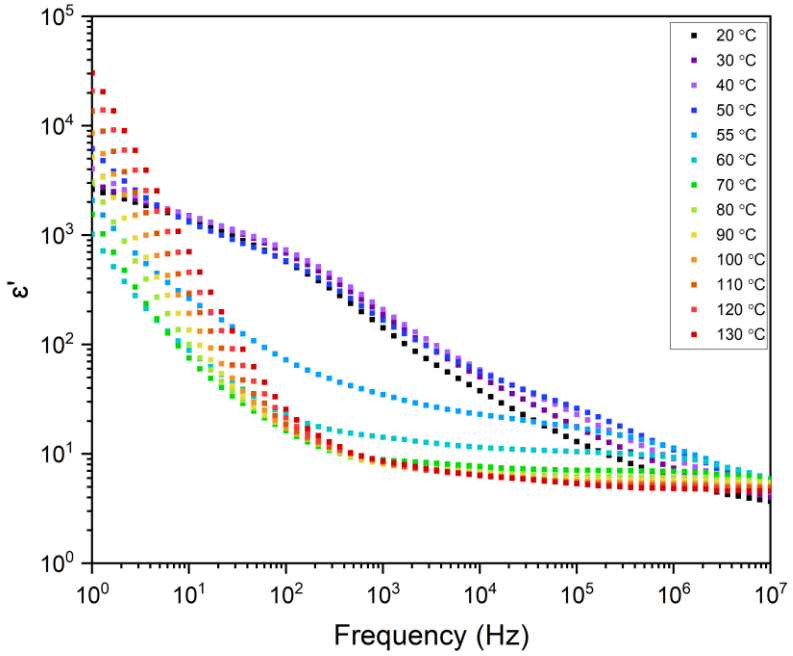

Figure 4.18 The isotherms of permittivity vs. frequency of oDMS-*MIM* $^{(+)}Br^{(-)}$ (Heating process).

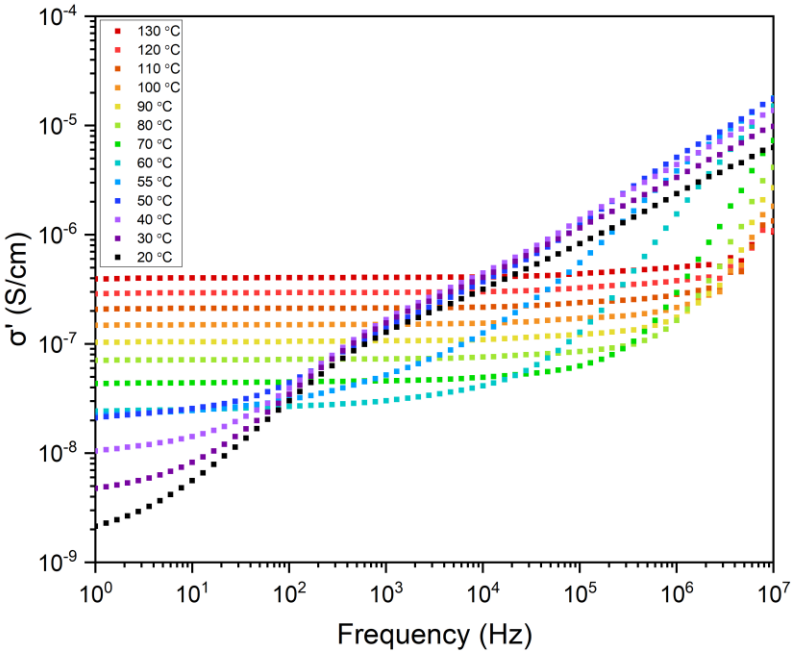

Figure 4.19 The isotherms of ion conductivity vs. frequency of oDMS-*MIM* $^{(+)}Br^{(-)}$ (Cooling process).

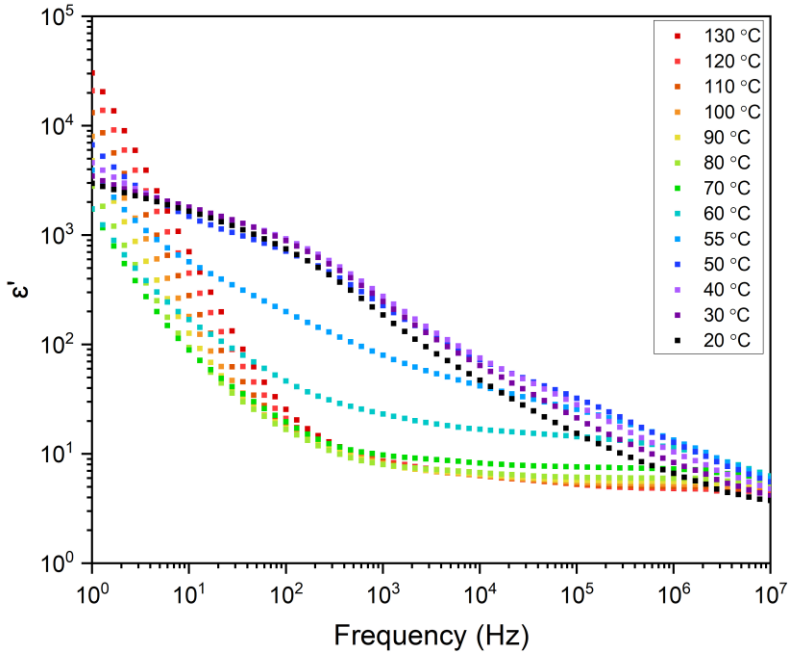

Figure 4.20 The isotherms of permittivity vs. frequency of oDMS-*MIM* $^{(+)}Br^{(-)}$ (Cooling process).

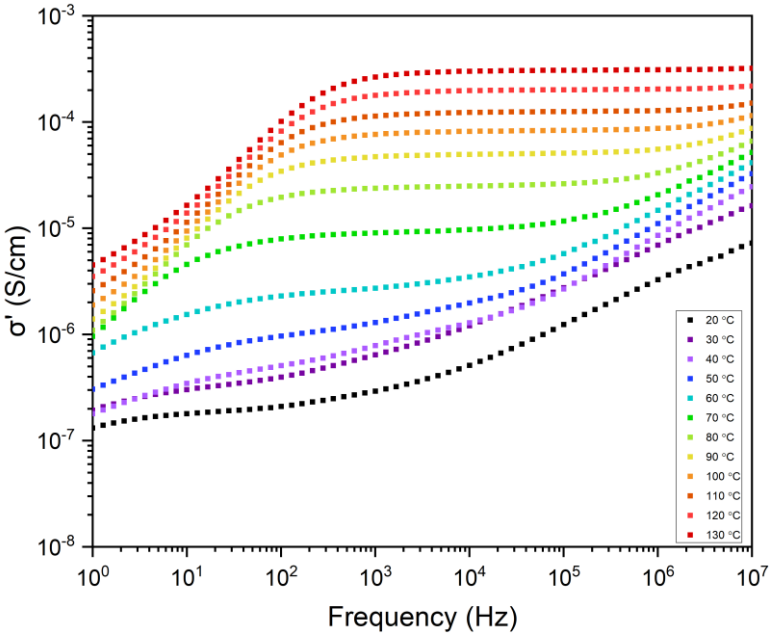

Figure 4.21 The isotherms of ion conductivity vs. frequency of oDMS-*MIM* $^{(+)}$*OMs*$^{(-)}$ (Heating process).

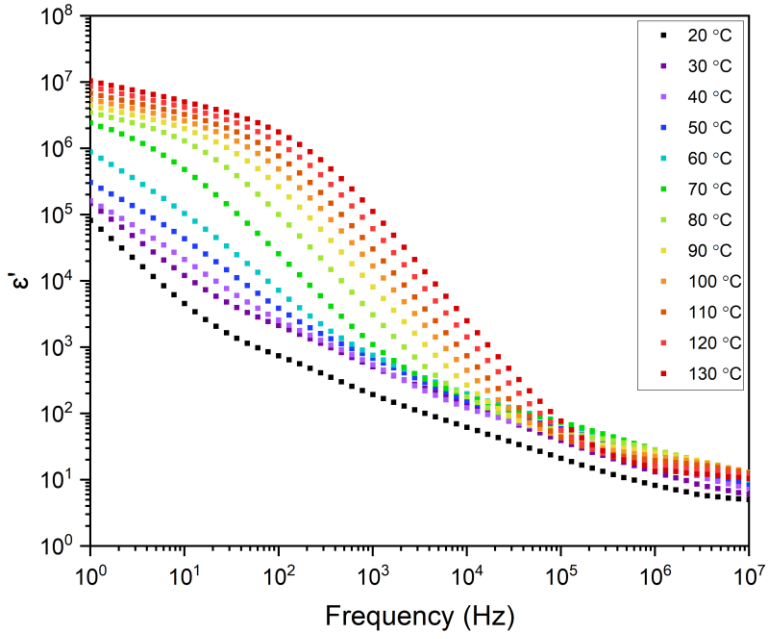

Figure 4.22 The isotherms of permittivity vs. frequency of oDMS-*MIM* $^{(+)}$*OMs*$^{(-)}$ (Heating process).

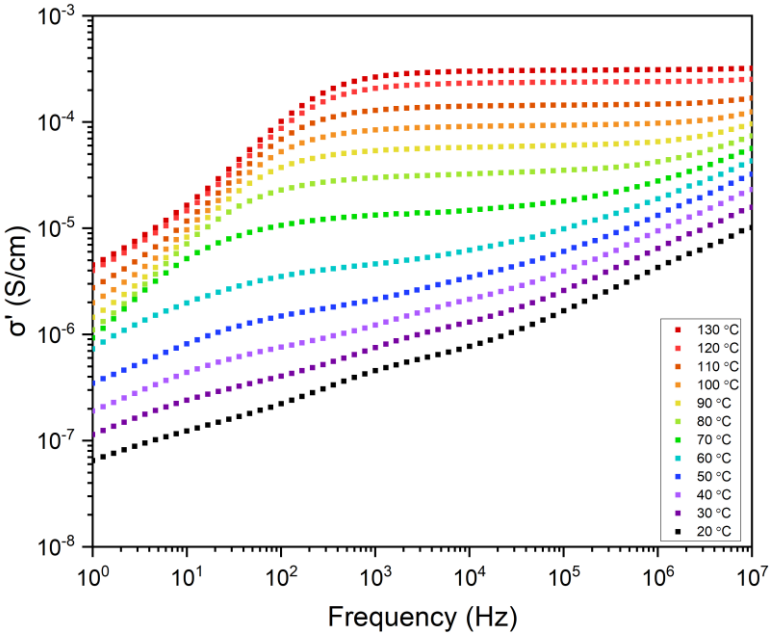

Figure 4.23 The isotherms of ion conductivity vs. frequency of oDMS-*MIM* $^{(+)}$*OMs*$^{(-)}$ (Cooling process).

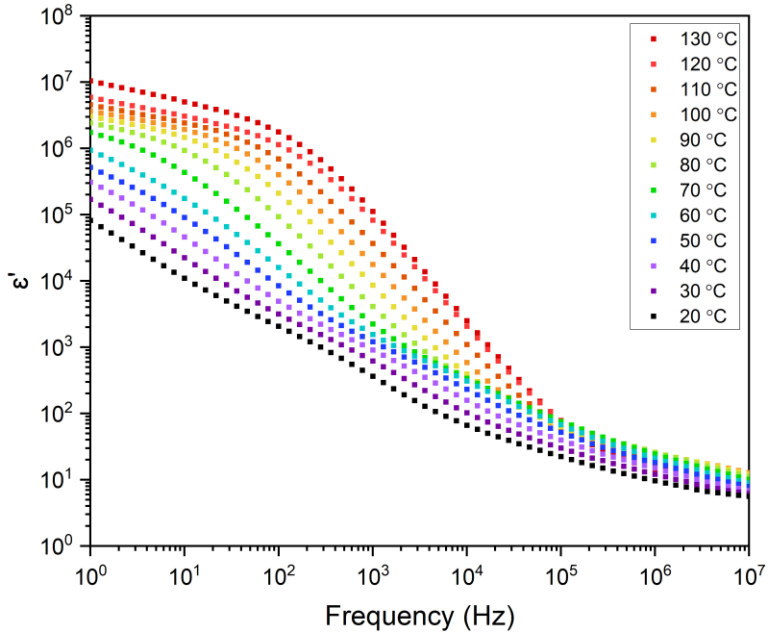

Figure 4.24 The isotherms of permittivity vs. frequency of oDMS-*MIM* $^{(+)}$*OMs*$^{(-)}$ (Cooling process).

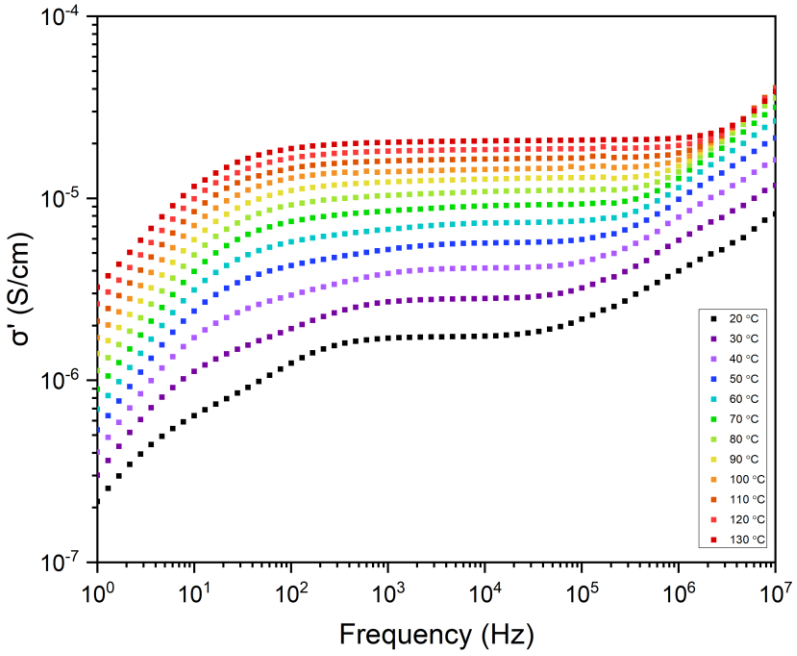

Figure 4.25 The isotherms of ion conductivity vs. frequency of oDMS-*MIM*$^{(+)}$*OTs*$^{(-)}$ (Heating process).

Figure 4.26, Figure 4.27, and Figure 4.28 for $OTs^{(-)}$ and Figure 4.29. Figure 4.30, Figure 4.31, and Figure 4.32 for $OTf^{(-)}$.

In terms of morpholine based chain ends, no plateau was found on the curves of σ' vs. f' before 65 ℃ in Figure 4.33. Then, DC plateau was found on the light blue curve at 65 ℃, which gave the transition. For ε', the slopes of curves of ε' vs. f' between 1~10000 Hz in Figure 4.34 were diverged into another value at 65 ℃, which also proved the structure change. In Figure 4.35 and Figure 4.36, which were the cooling cycles, the reversed transition was shown around 65 ℃ but is not as obvious as the heating process.

Furthermore, the zwitterionic chain end gave the amphiphilic oligomer significant transition on the isotherms of σ' vs. f' and ε' vs. f'. In Figure 4.37, the linear curve of σ' vs. f' at most temperatures showed stable and ordered structures in a wide range of temperatures. After 110 ℃, a plateau showed up on the orange-colored curve between 1 to 100 Hz, and the order-disorder transition happened. For ε', it increased first, then decreased from 100 ℃ (orange curve) and reached a close value around 110~115 ℃ in Figure 4.38. The cooling curves offered a higher T_{ODT}. The noticeable change in curves of σ' vs. f' and ε' vs. f' between 130 and 125 ℃ was observed in Figure 4.39 and Figure 4.40, which offered a T_{ODT} of 125 ℃.

In summary, phase transitions of oligomers with charged chain ends were characterized by dielectric spectroscopy to reveal the relationship between ion conductivity/permittivity and frequency of applied electric fields. Most transition temperatures obtained by SAXS and DS were similar, while oDMS-$Py^{(+)}$-$OMs^{(-)}$ and oDMS-$MMP^{(+)}$-$OMs^{(-)}$ gave different results. In the following sections, differences in phase transition behaviors from SAXS and DS were discussed. Furthermore, the effects of ions and order structures on ion conductivity were also discussed.

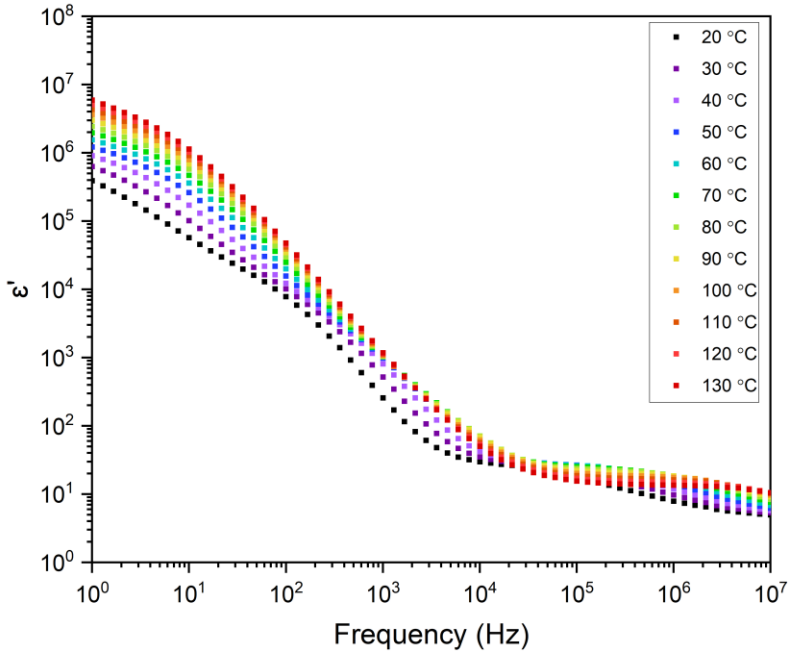

Figure 4.26 The isotherms of permittivity vs. frequency of oDMS-*MIM*$^{(+)}$*OTs*$^{(-)}$ (Heating process).

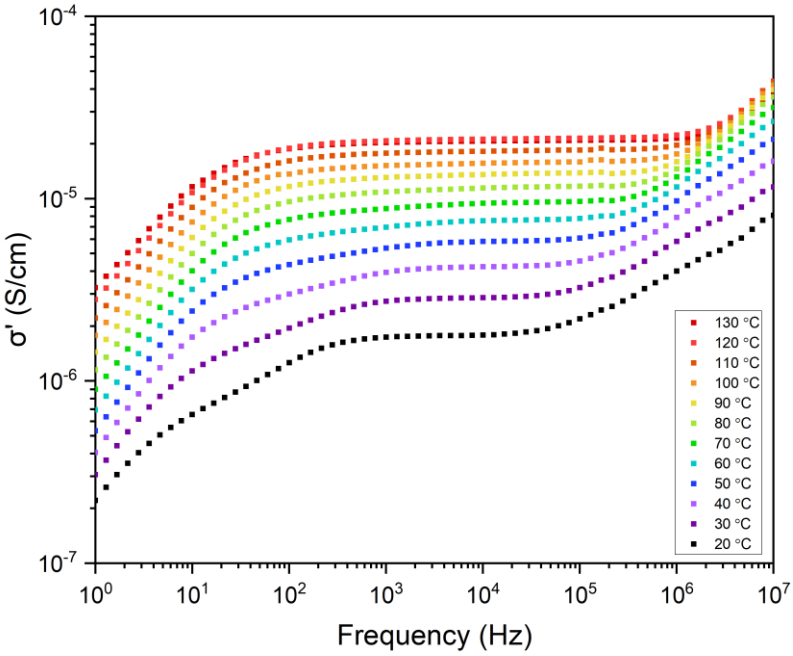

Figure 4.27 The isotherms of ion conductivity vs. frequency of oDMS-*MIM*$^{(+)}$*OTs*$^{(-)}$ (Cooling process).

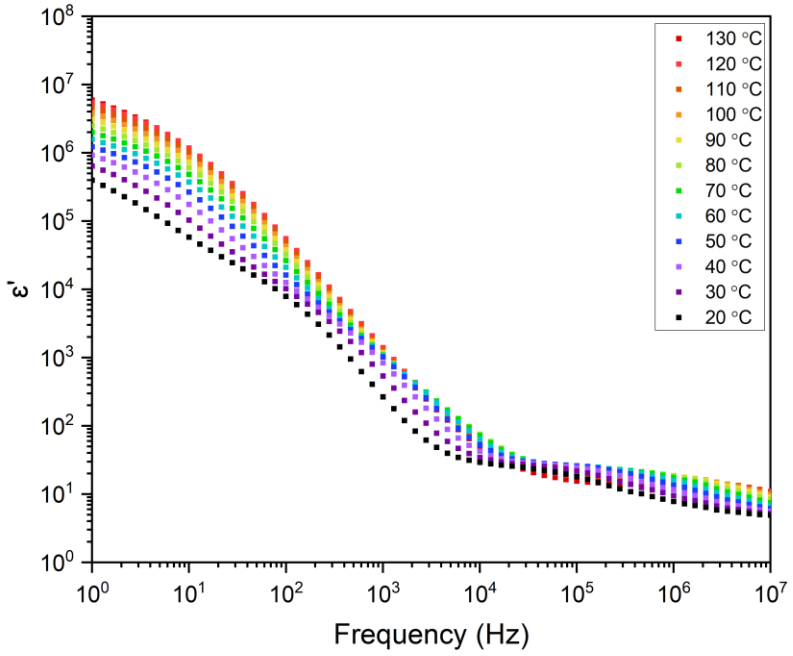

Figure 4.28 The isotherms of permittivity vs. frequency of oDMS-*MIM*$^{(+)}$*OTs*$^{(-)}$ (Cooling process).

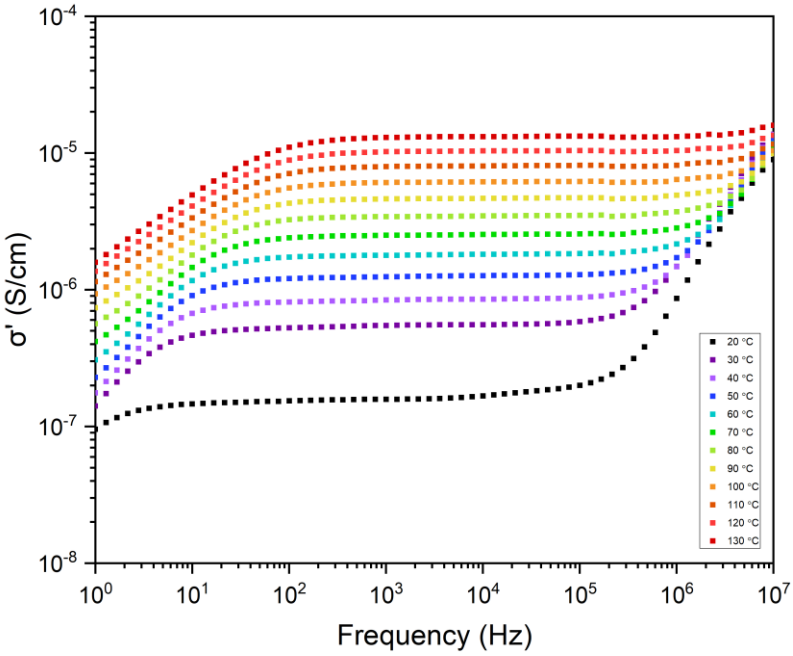

Figure 4.29 The isotherms of ion conductivity vs. frequency of oDMS-*MIM*$^{(+)}$*OTf*$^{(-)}$ (Heating process).

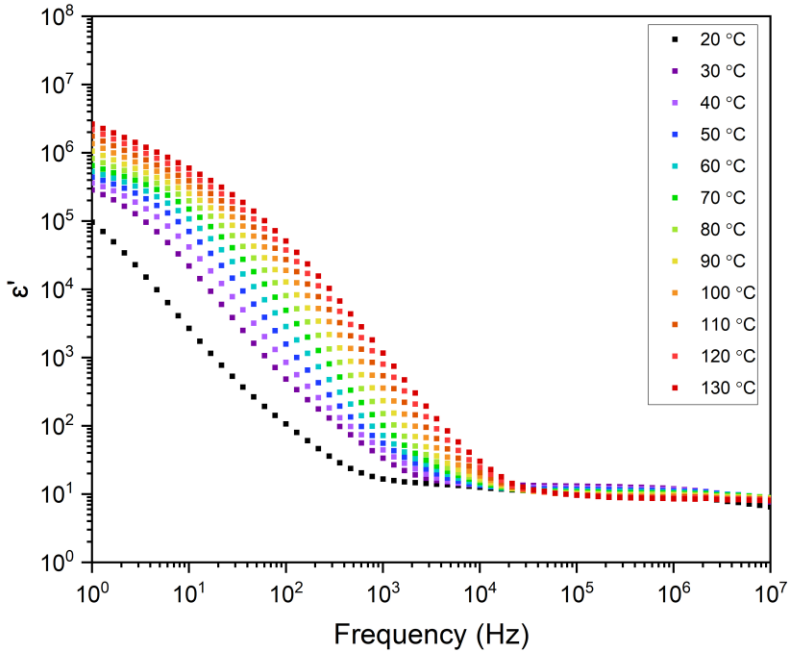

Figure 4.30 The isotherms of permittivity vs. frequency of oDMS-*MIM*$^{(+)}$*OTf*$^{(-)}$ (Heating process).

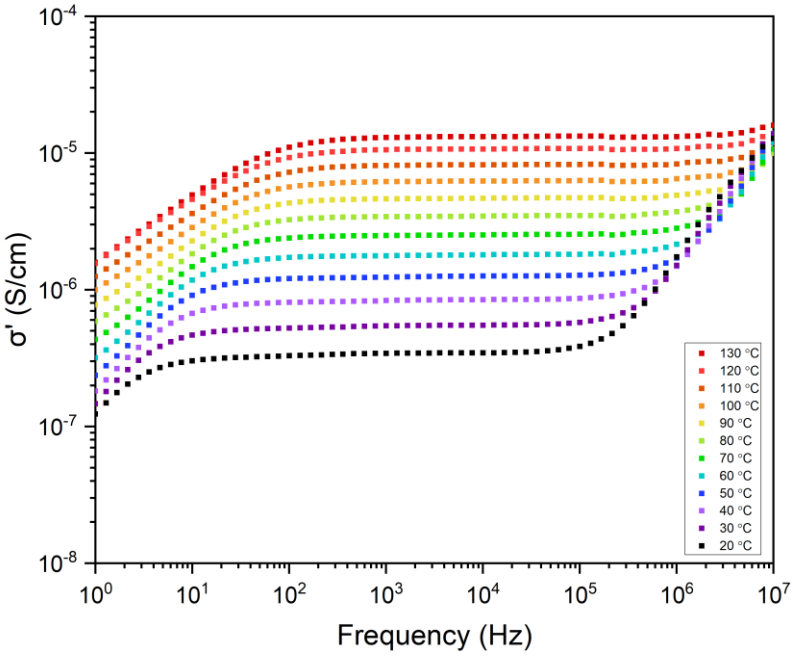

Figure 4.31 The isotherms of ion conductivity vs. frequency of oDMS-*MIM*$^{(+)}$*OTf*$^{(-)}$ (Cooling process).

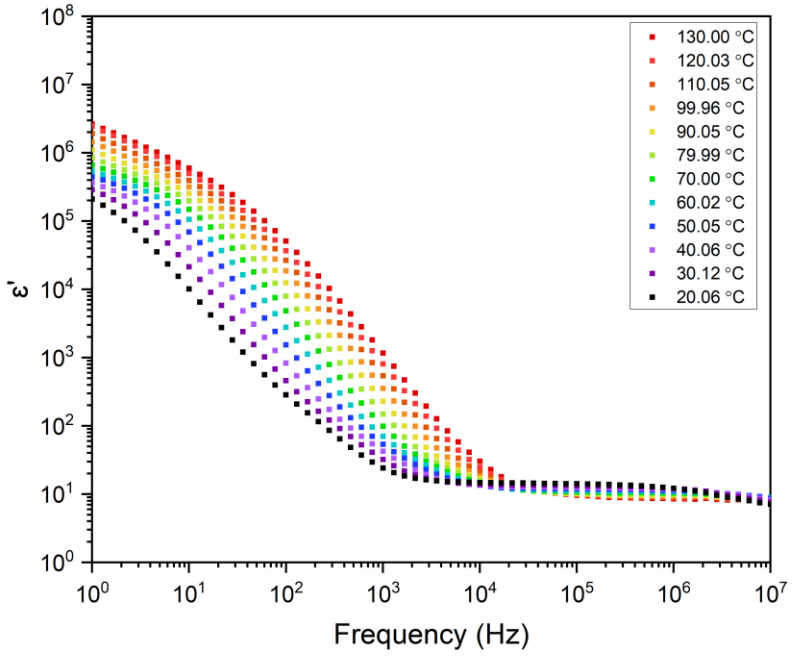

Figure 4.32 The isotherms of permittivity vs. frequency of oDMS-*MIM*$^{(+)}$*OTf*$^{(-)}$ (Cooling process).

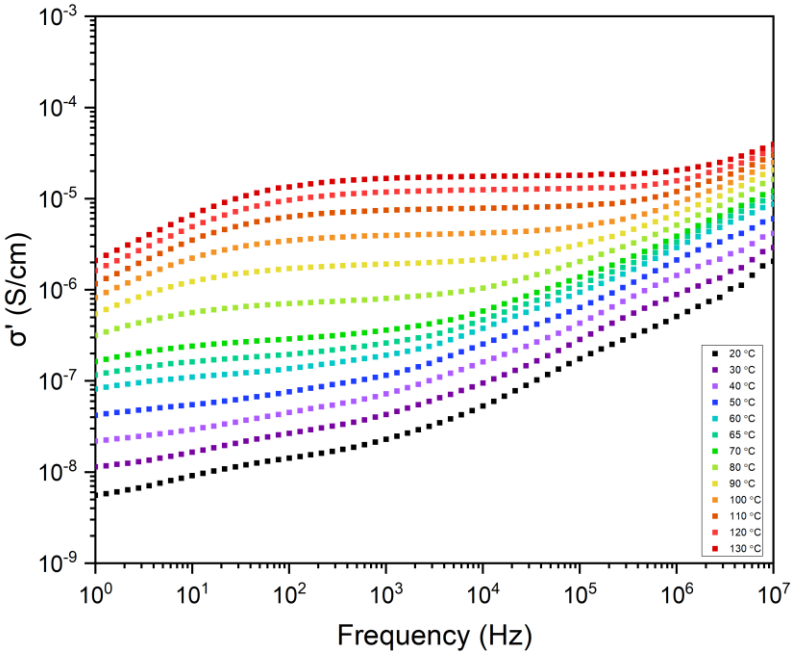

Figure 4.33 Ion conductivity vs. frequency of oDMS-*MMP*$^{(+)}$*OMs*$^{(-)}$ (Heating process).

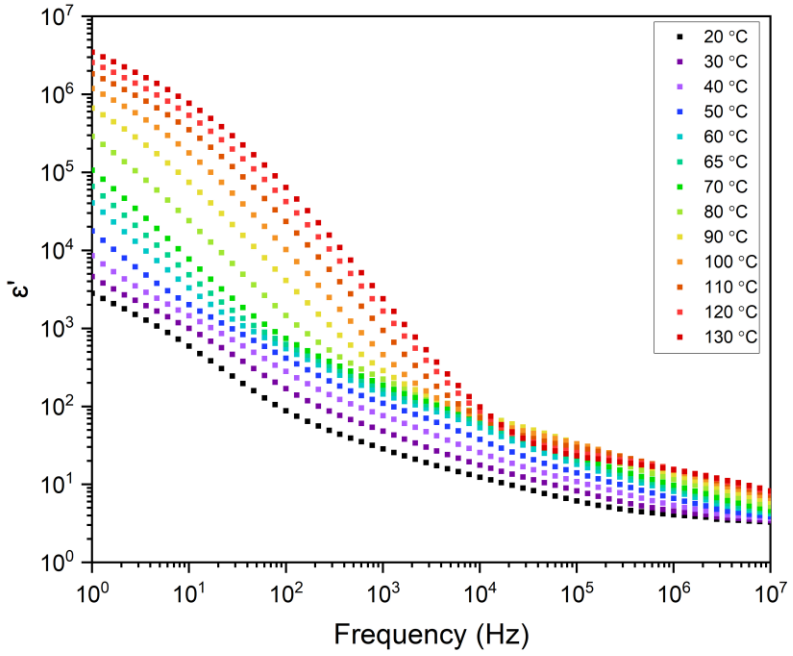

Figure 4.34 Permittivity vs. frequency of oDMS-*MMP* $^{(+)}$*OMs*$^{(-)}$ (Heating process).

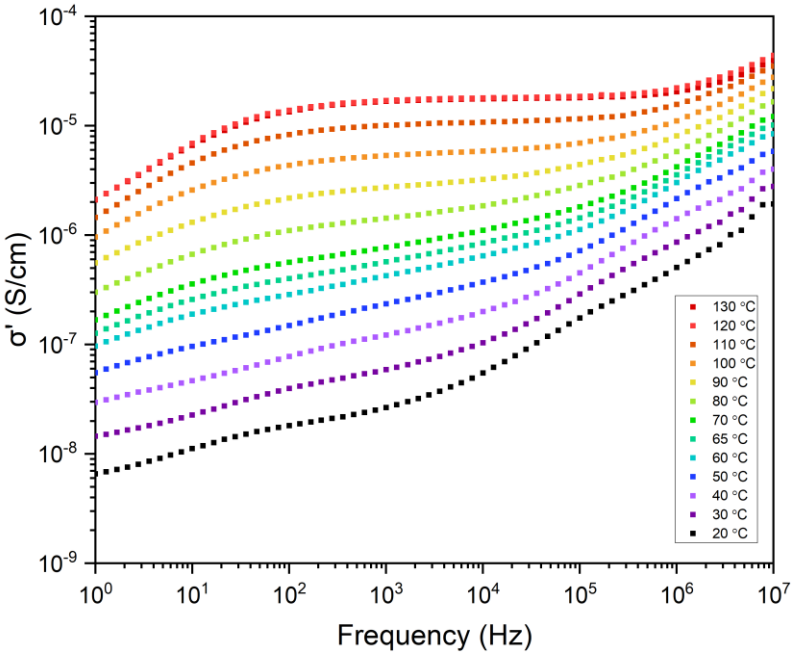

Figure 4.35 Ion conductivity vs. frequency of oDMS-*MMP* $^{(+)}$*OMs*$^{(-)}$ (Cooling process).

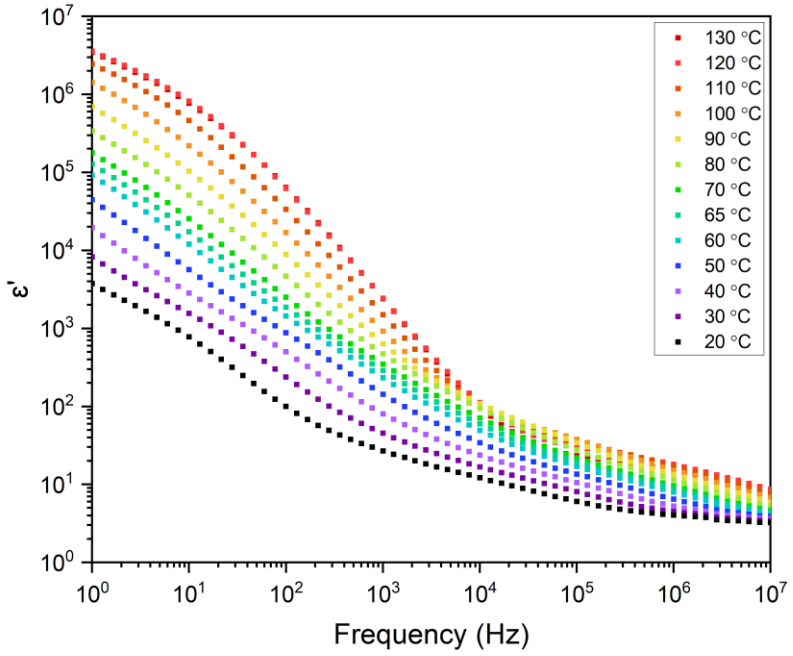

Figure 4.36 Permittivity vs. frequency of oDMS-*MMP* $^{(+)}$*OMs*$^{(-)}$ (Cooling process).

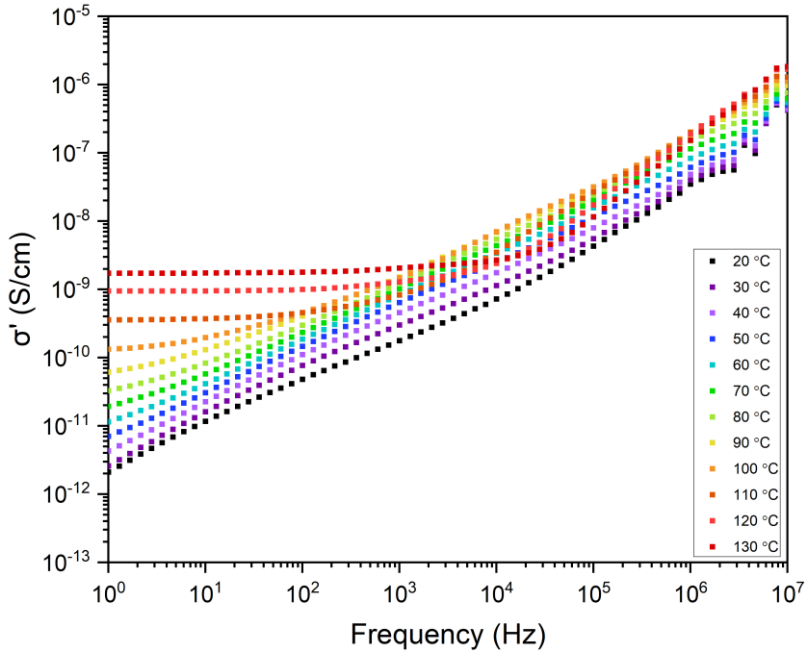

Figure 4.37 Ion conductivity vs. frequency of oDMS-$N(CH_3)_2^{(+)}$-$(CH_2)_3$-$SO_3^{(-)}$ (Heating process).

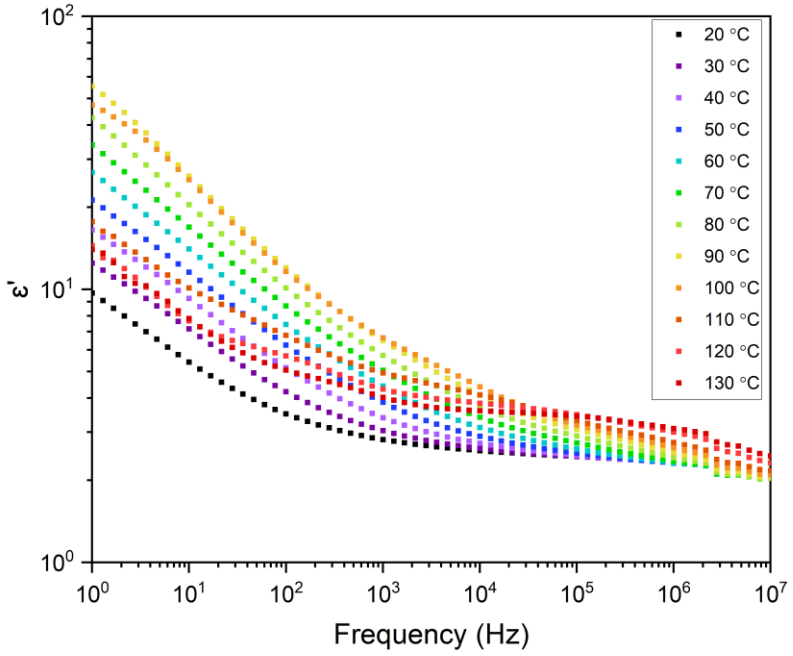

Figure 4.38 Permittivity vs. frequency of oDMS-$N(CH_3)_2^{(+)}$-$(CH_2)_3$-$SO_3^{(-)}$ (Heating process).

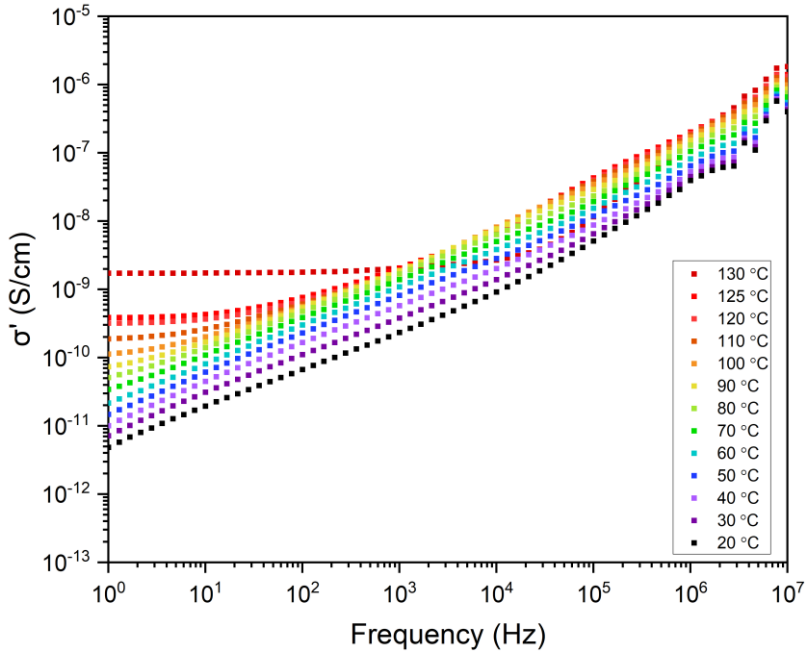

Figure 4.39 Ion conductivity vs. frequency of oDMS-$N(CH_3)_2^{(+)}$-$(CH_2)_3$-$SO_3^{(-)}$ (Cooling process).

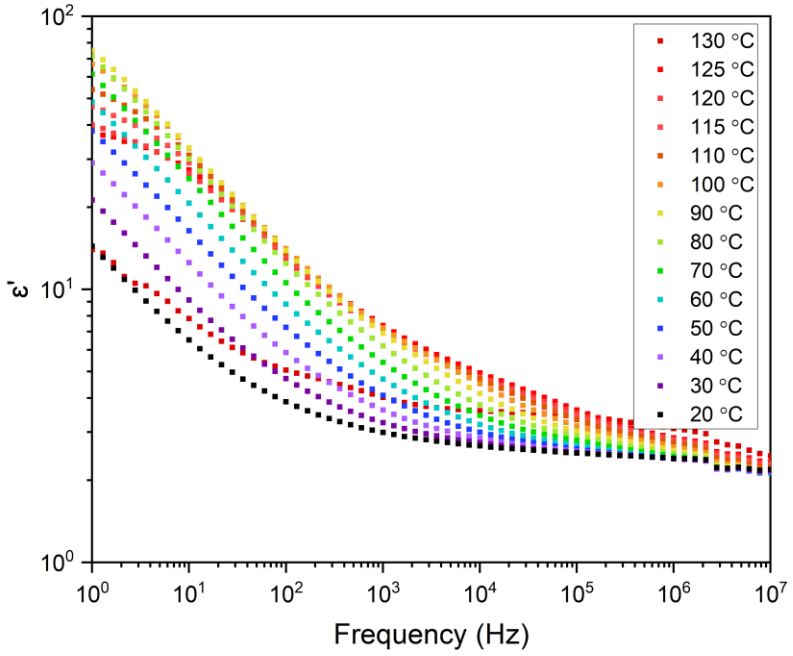

Figure 4.40 Permittivity vs. frequency of oDMS-$N(CH_3)_2^{(+)}$-$(CH_2)_3$-$SO_3^{(-)}$ (Cooling process).

4.3.3 Comparison of Phase Transition Behavior and T_{ODT} Measured by SAXS and DS

Two different techniques, SAXS and DS, were conducted in this work to analyze the phase transition behaviors and T_{ODT}s of amphiphilic oligomers. The results were compared in Table 4.5.

Based on the results in Table 4.5, oDMS-$Py^{(+)}$-$Br^{(-)}$, oDMS-$MIM^{(+)}$-$OMs^{(-)}$ and oDMS-$N(CH_3)_2^{(+)}$-$(CH_2)_3$-$SO_3^{(-)}$ had the similar measured T_{ODT}s. However, there are two different observations: (1) Order-disorder transition for oDMS-$MIM^{(+)}$-$Br^{(-)}$ and oDMS-$MIM^{(+)}$-$OMs^{(-)}$ is irreversible in the time scale of the SAXS measurements, while DS measurements gave the reversible transition. (2) Phase transition at 65 ℃ could not be detected for oDMS-$Py^{(+)}$-$OMs^{(-)}$ and oDMS-$MMP^{(+)}$-$OMs^{(-)}$ from SAXS, while both had a weak transition of structure detected by DS measurements.

The differences are possibly due to the following reasons:

(1) The time of measurement for each technique is different. SAXS applied 5 mins for each temperature while DS equilibrated for at least 5 mins at the new temperature, then started the measurement. Thus, samples in DS measurement had more time to form the stable order structures, and the transition at each temperature will not be overlapped.

(2) Although the macroscopic morphology does not change during the SAXS measurements, the shifts of peaks were observed for oDMS-$Py^{(+)}$-$OMs^{(-)}$ and oDMS-$MMP^{(+)}$-$OMs^{(-)}$. Take oDMS-$Py^{(+)}$-$OMs^{(-)}$ as an example. The location of the primary peak was plotted with the changing temperatures in Figure 4.41. The primary peak shifted by two different tendencies, and a clear transition was shown at around 70 ℃. This transition was captured by DS measurement.

For the zwitterionic chain end, the two measurements gave a close result due to the ultra-low mobility of cation and anion locked by covalent bonds.

Table 4.5 T_{ODT}s of amphiphilic oligomers based on SAXS and DS measurements.

Cation	Anion	T_{ODT} (℃) (SAXS)	T_{ODT} (℃) (DS Heating Cycles)	T_{ODT} (℃) (DS Cooling Cycles)
$Py^{(+)}$	$OMs^{(-)}$	>110	Weak transition ~ 65	Weak transition ~ 65
	$Br^{(-)}$	100~110	95~100	100~105
$MIM^{(+)}$	$OMs^{(-)}$	60~70	60~70	60~70
	$Br^{(-)}$	65~70	50~55	55~60
	$OTs^{(-)}$	/	Not detected	Not detected
	$OTf^{(-)}$	/	Not detected	Not detected
$MMP^{(+)}$	$OMs^{(-)}$	>110	Weak transition ~ 65	Weak transition ~ 65
Zwitterion				
$N(CH_3)_2^{(+)}$-$(CH_2)_3$-$SO_3^{(-)}$		>110	~110	~125

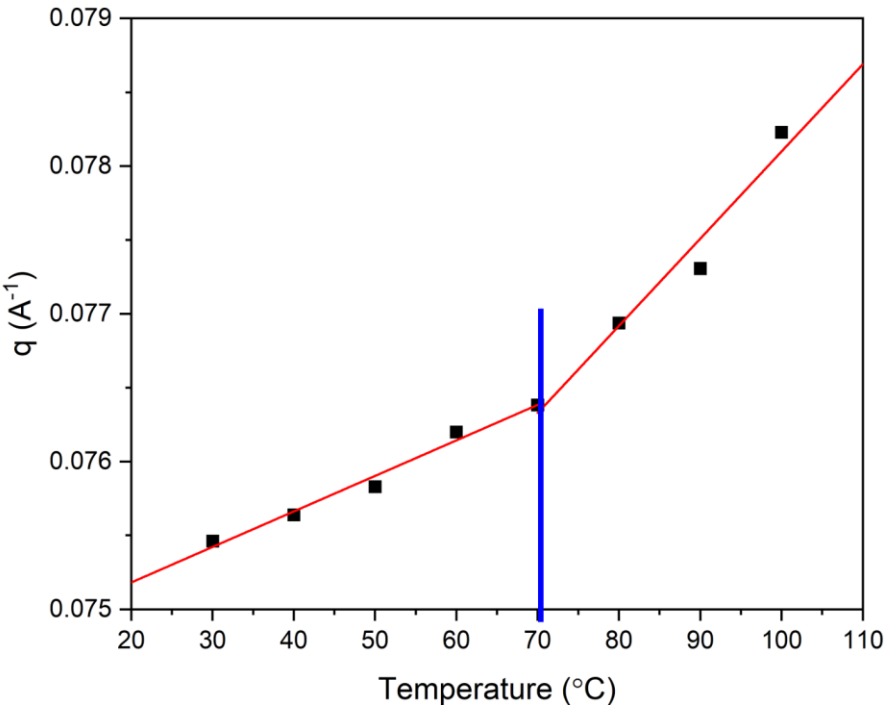

Figure 4.41 Primary peak shifted with temperatures.

4.3.4 Study of Segregation Strength of Ions and Repulsion Between oDMS and End Groups

The incompatibility, represented as segregation strength (χN), gives amphiphilic oligomers the ability to phase separate to form nanostructures. In this section, relative χN between different parameters were estimated based on the resulted phase separation behaviors. In this work, χ was used instead of χN due to $N = 14$ for all oligomers in this system.

When comparing T_{ODT}, oDMS with pyridinium-based chain ends had a higher T_{ODT} than oDMS with imidazolium-based chain ends. Thus, there was a stronger repulsion, the larger χ, between pyridinium-based chain ends and oDMS chains.[11] Considering the effect of cations or anions, the exchange of anions did not change the T_{ODT}.

For the effect of cations, different domain spacings were obtained with the order from large to small as $MMP^{(+)} > Py^{(+)} > MIM^{(+)}$. Based on the morphology of LAM, the χ of cation in terms of $OMs^{(-)}$ followed the order of $MMP^{(+)} > Py^{(+)}$.[12] Furthermore, the lowest T_{ODT} was obtained for $MIM^{(+)}$, thus, the χ of cation in term of $OMs^{(-)}$ followed the order of $MMP^{(+)} > Py^{(+)} > MIM^{(+)}$. Interesting, the same order of cations was obtained for the segregation strength when the anion was $OMs^{(-)}$. Compared with $MMP^{(+)}$, $Py^{(+)}$ and $MIM^{(+)}$ have the conjugated structure. When forming ion pairs with $OMs^{(-)}$, the charges of ion pairs can be distributed within the conjugated structure, which lowers the density of the electron cloud and gives stable ion pairs. Thus, $Py^{(+)}$ and $MIM^{(+)}$ preferred to coordinate with $OMs^{(-)}$, which gave a low segregation strength. Although both $Py^{(+)}$ and $MIM^{(+)}$ have the conjugated structure, the charged position of $MIM^{(+)}$ was towards the opposite direction of oDMS chains. Large anions, such as $OMs^{(-)}$, were able to contact $MIM^{(+)}$ easily. Thus $MIM^{(+)}$ was the lowest in segregation strength of cations.

4.3.5 Evaluation of Ion Conductivity During Heating and Cooling Process

For all oligomers with charged chain ends, the isotherms of σ' vs. f' have lower values of

ion conductivities at low frequencies of electric field and higher values of ion conductivities in the range of high frequencies. For the typical curve of σ' vs. f', such as the red curve in Figure 4.35, three distinct regions can be observed: (1) The low-frequency dispersion region. (2) The frequency-independent plateau region. (3) The high-frequency dispersion region. The lower ion conductivity in the low-frequency dispersion region between 1 to 100 Hz was caused by the electrode polarization phenomenon, which was illustrated in Figure 4.42. At low frequencies of the electric field, ions were moved to the interfaces between sample and electrodes, and ionic double layers were formed at these interfaces. Thus, fewer ions can move and respond to the electric field changes, which leads to low ion conductivities. With the high frequencies, which ranged from 10^5 to 10^7 Hz, local movements of ions were achieved. The higher apparent ion conductivities were observed because ions were moved within a small area and less internal structure was involed.[13, 14]

The ion conductivity was determined by isotherms of σ' vs. $f'$where $f' = 10^4\ Hz$ and the relationship between σ' and temperature (T) was expressed as $\log\sigma'$ vs. $1000/T$. This work focused on the temperature range of 20 to 130 ℃ due to the available phase transition behaviors from SAXS measurements, and the effects of anions on other temperature ranges were listed as future references.

The influence of cations was compared under the same anion. For the anion of $OMs^{(-)}$, curves of $\log\sigma'$ vs. $1000/T$ with different cations were compared in Figure 4.43. When the temperature was higher than -5 ℃, no matter the change of structures, σ' followed the order as $MIM^{(+)} > Py^{(+)} > MMP^{(+)}$. The order of cations followed their segregation strength. Here is our assumption: $MIM^{(+)}$ had the lowest segregation strength, and it preferred to contact with anions.

The overall distance between ions was the shortest. Thus, ions were able to move the longest

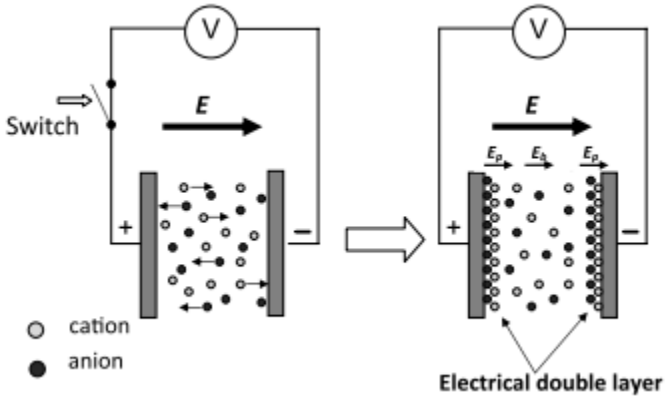

Figure 4.42 Electrode polarization phenomenon. Reprint with permission from Reference [14]. Copyright 2013 IOP Publishing.

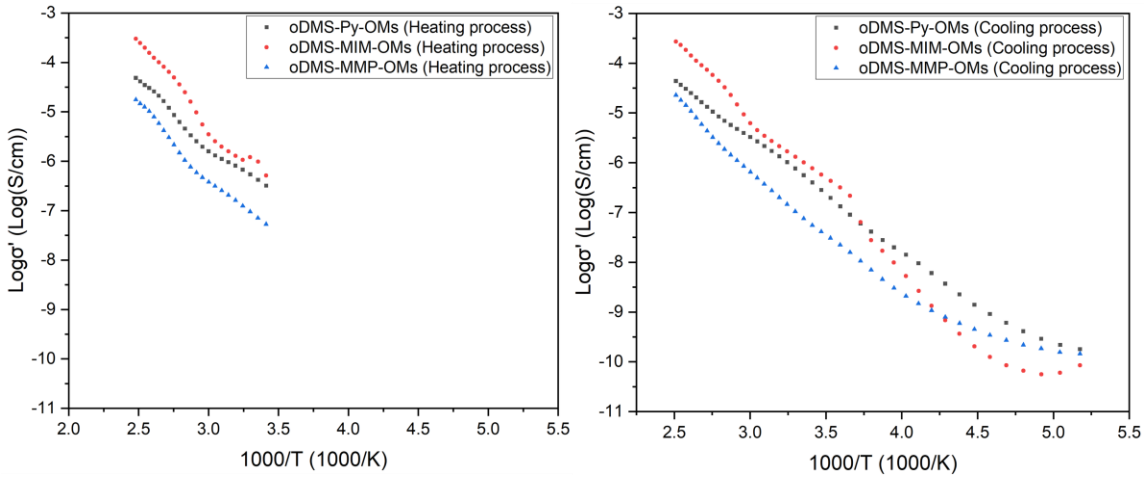

Figure 4.43 $\log \sigma'$ vs. $1000/T$ of oDMS-*Py* $^{(+)}$*OMs* $^{(-)}$, oDMS-*MIM* $^{(+)}$*OMs* $^{(-)}$and oDMS-*MMP* $^{(+)}$*OMs* $^{(-)}$.

distance, giving the highest ion conductivity. In the temperature range of -35 and -5 ℃, σ' followed the order as $Py^{(+)} > MIM^{(+)} > MMP^{(+)}$. Continuing lower the temperature, σ' followed the order as $Py^{(+)} > MMP^{(+)} > MIM^{(+)}$.

The effect of anions was compared under the same cation. For the pyridinium based chain ends, curves of $\log\sigma'$ vs. $1000/T$ with different anions were compared in Figure 4.44. For the heating process, σ' of $OMs^{(-)}$ was higher than $Br^{(-)}$ when the temperature was higher than 85 ℃, while σ' of $OMs^{(-)}$ was lower than $Br^{(-)}$ between 20~85 ℃. In terms of the cooling cycle, the same conclusion was followed before -24 ℃. When the temperature was lower than -24 ℃, the similar values of σ' obtained. When the temperature was higher than 85 ℃, the ion conductivity of $Br^{(-)}$ started to decrease to the lowest value at the disordered state. Although the mobility of $Br^{(-)}$ was increased, the strong coordination ability of $Br^{(-)}$ restricted the movement of ions, which gave a lower ion conductivity at elevated temperatures. When the temperature was lower than 85 ℃, both anions were restricted by internal structures, while the smaller size of $Br^{(-)}$ made it move easier, resulting in a higher σ'. After the temperature was low enough to freeze the ions, the similar mobility of anions gave the close values of σ'.

For oligomers with chain ends of imidazolium-based ILs, four different anions were studied, and the behavior was illustrated in Figure 4.45. When the temperature was higher than 65 ℃, σ' followed the order as $OMs^{(-)} > OTs^{(-)} > OTf^{(-)} > Br^{(-)}$. If the temperatures ranged between 5 ℃ and 65 ℃, σ' followed the order as $OTs^{(-)} > OMs^{(-)} > OTf^{(-)} > Br^{(-)}$. Furthermore, σ' followed the order as $OTs^{(-)} > Br^{(-)} > OTf^{(-)} > OMs^{(-)}$ in the temperature of -5 ~ 5 ℃. When the temperature was lower than -5, σ' followed the order as $OTs^{(-)} > Br^{(-)} > OMs^{(-)} > OTf^{(-)}$ and tends to the same as ultra-low temperature reached. There was no phase transition for $OTs^{(-)}$ and $OTf^{(-)}$. Thus, their ion conductivities increased smoothly with the increase of temperatures. However, $Br^{(-)}$ and $OMs^{(-)}$

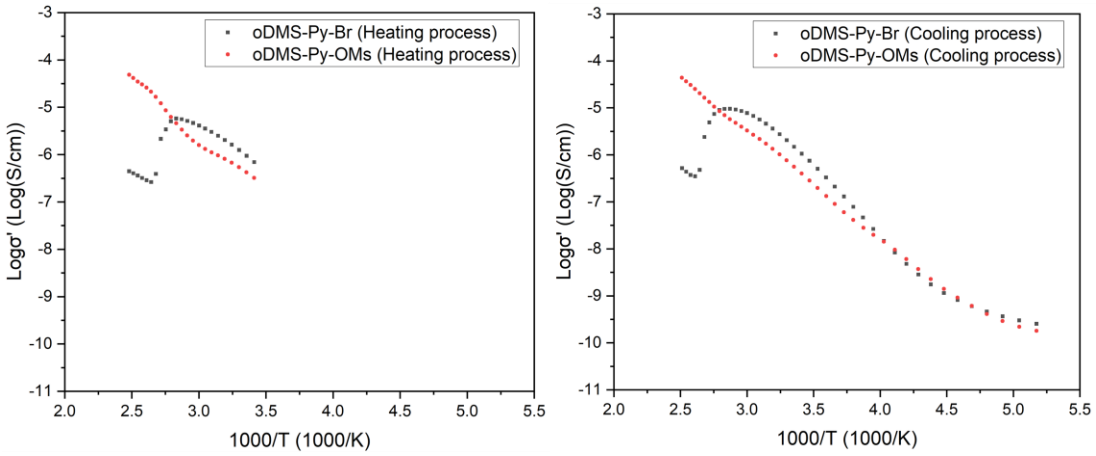

Figure 4.44 $\log \sigma'$ vs. $1000/T$ of oDMS-$Py^{(+)}Br^{(-)}$ and oDMS-$Py^{(+)}OMs^{(-)}$.

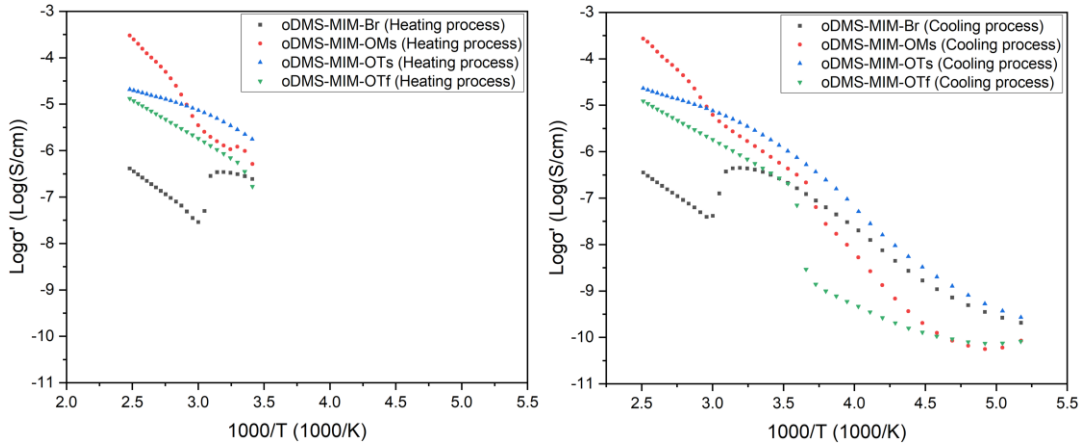

Figure 4.45 $\log \sigma'$ vs. $1000/T$ of oDMS-$MIM^{(+)}Br^{(-)}$, oDMS-$MIM^{(+)}OMs^{(-)}$, oDMS-$MIM^{(+)}OTs^{(-)}$, and oDMS-$MIM^{(+)}OTf^{(-)}$.

reached the disordered state, and there were transition points on the curves of ion conductivities, which suggested the influence of ordered structure on the ion conductivity. $Br^{(-)}$ had the lowest ion conductivity above room temperature due to its strongest coordination ability. There was a jump point on the ion conductivity of $Br^{(-)}$, which indicated the improvement of ion conductivity by the ordered structure, and a similar phenomenon has been reported by Takashi and coworkers. They synthesized ammonium ionic liquids with $BF4^{(-),}$ and these ionic liquids had different morphologies under various temperatures. When the bicontinuous cubic phase was reached, there was a jump point on the curve of ion conductivity which showed the improvement of the ion conductivity with the bicontinuous cubic structure.[15] More details were discussed in the section of the effect of ordered structures on ion conductivity.

For chain ends of zwitterion, curves of $\log \sigma'$ vs. $1000/T$ was shown in Figure 4.46. σ' with zwitterionic chain ends was much lower than all chain ends of ionic liquid due to the low mobility of ions limited by covalent bonds. Similar to chain ends with $Br^{(-)}$, weak jump points were observed on the curves. The first transition point is still the order-disorder transition point, and the second transition point was 100 ℃, where the highest σ' was obtained. Different from ionic chain ends, whose σ' was the same during heating and cooling, σ' of oligomers with zwitterionic chain ends was lower during heating than cooling when the temperature was higher than 100 ℃. This phenomenon may be from the low mobility of ions that a long time of thermal annealing was needed.

The effect of order structures was studied by comparing the ion conductivity of oDMS-$MIM^{(+)}Br^{(-)}$ and oDMS-$MIM^{(+)}OMs^{(-)}$, which was shown in Figure 4.47. Both oligomers had the HEX structure from room temperature to 130 ℃, while $Br^{(-)}$ had a jump point on the curve, which indicated that the effect of ordered structures on ion conductivity might relate to the nature of

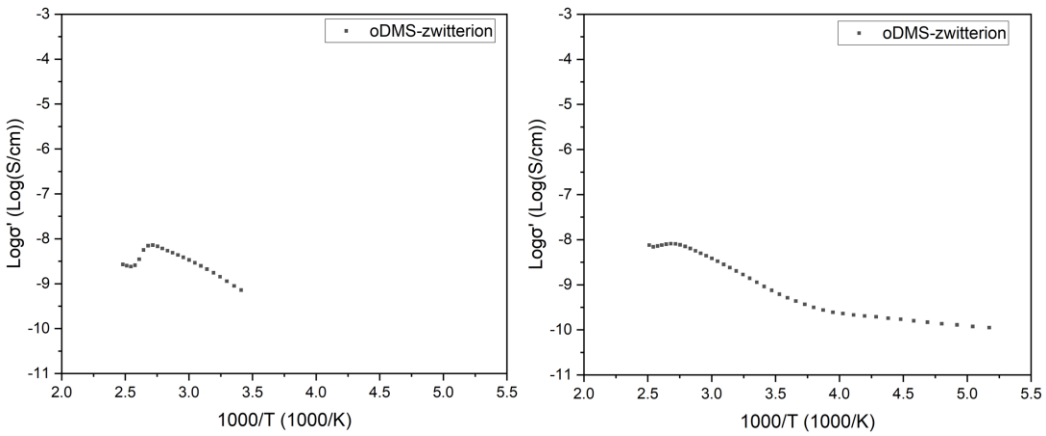

Figure 4.46 $\log \sigma'$ vs. $1000/T$ of oDMS- $N(CH_3)_2^{(+)}$-$(CH_2)_3$-$SO_3^{(-)}$ (Left: Heating process; Right: Cooling process).

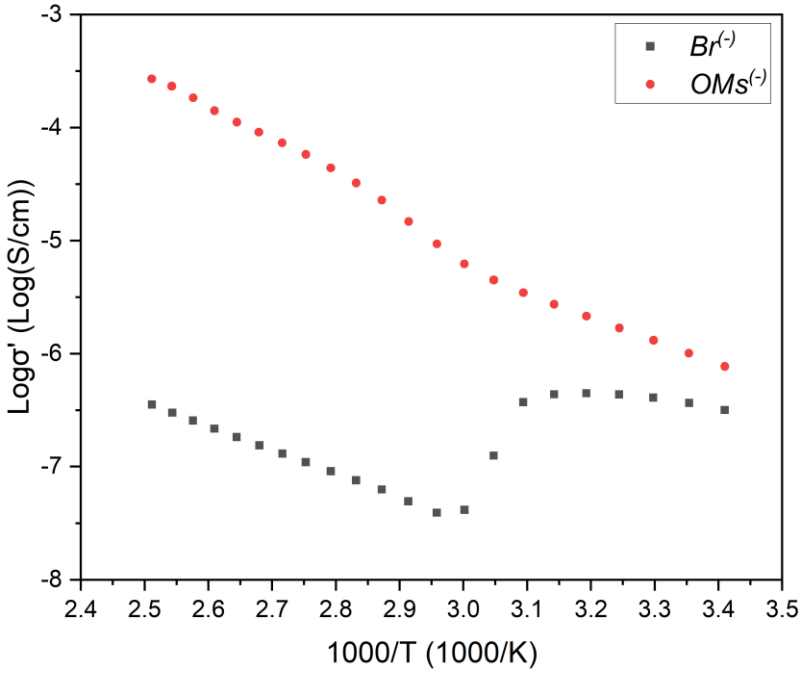

Figure 4.47 $\log \sigma'$ vs. $1000/T$ of oDMS-$MIM^{(+)}OMs^{(-)}$ and oDMS-$MIM^{(+)}Br^{(-)}$.

anions. For $OMs^{(-)}$, it was loosely coordinated, which led to the high ion conductivity. A transition point occurred on the red curve, while the ordered structure did not change the ion conductivity dramatically. However, there were two transition points for $Br^{(-)}$ with significant changes in ion conductivities. The first transition point was the order-disorder transition at 65 ℃. The second transition point was at 40 ℃ with the highest value of σ'. As discussed in section 1.4, the ion conductivity is decided by both characteristics of ions and the degree of order of structure. The highest point of σ' may be contributed by the perfect balance between ion mobility and degree of order of structure. With the increase of temperatures, the lowest conductivity was achieved at the disordered phase. It suggested that the stronger coordination ability of $Br^{(-)}$ lowered its conductivity, but the ordered structure guided the movements of $Br^{(-)}$, which is smaller in size. Thus, the ordered structure improved the ion conductivity for $Br^{(-)}$. To prove the assumption, curves of $\log \sigma'$ vs. $1000/T$ for oligomers with the anion of $Br^{(-)}$ were compared in Figure 4.48, and jump points were observed on all samples.

In summary, the effects of cations, anions, and order structures on the ion conductivity of oligomers with charged chain ends were explored. Furthermore, their effects were closely related to the characteristics of ions.

4.4 Conclusion

In this chapter, phase behaviors of amphiphilic oligomers with different charged chain ends were studied. With the combination of various cations and anions, sub-10 nm structures were obtained for all tested samples. By tuning the cations or anions, phase behaviors of oligomers with charged chain ends, including morphologies, domain spacing, and order-disorder transition temperatures, can be modified based on the requirements.

On the other hand, distinctive characteristics of cation and anions were introduced into

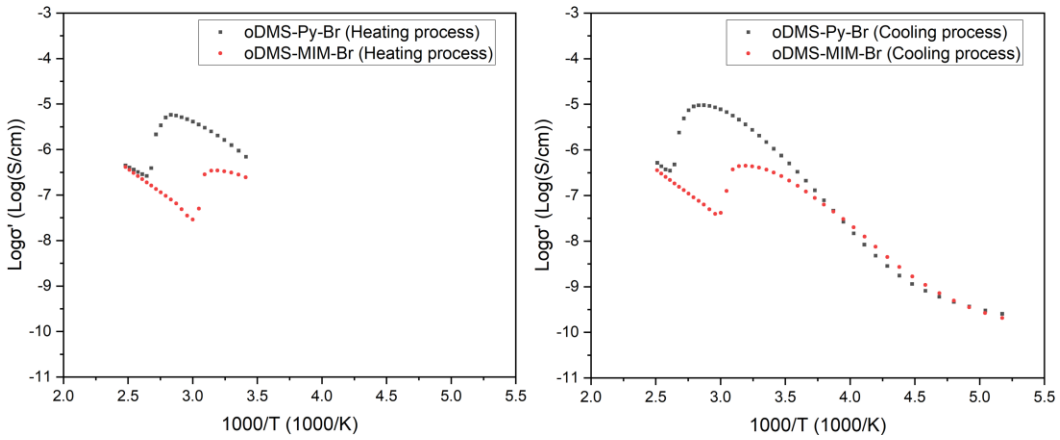

Figure 4.48 $\log \sigma'$ vs. $1000/T$ of oDMS-$Py^{(+)}Br^{(-)}$ and oDMS-$MIM^{(+)}Br^{(-)}$.

amphiphilic oligomers, and the effects of cation and anions on the phase behaviors were explored. Anions had an insignificant effect, while cations played a vital role on order-disorder transition temperatures. Also, repulsions between pyridinium-based chain ends and oDMS chains were stronger than those of imidazolium-based chain ends and oDMS chains. The segregation strength of cations followed the order of $MMP^{(+)} > Py^{(+)} > MIM^{(+)}$, which was correlated to the structures of cations.

On the other hand, the effects of cations and anions on the ion conductivity of oligomers with charged chain ends from room temperature to 130 ℃ were analyzed. Cations influenced the ion conductivity by their segregation strength, while anions affected the ion conductivity by their size and coordination ability. Interestingly, a jump point on the relationship between ion conductivity and the temperature was observed for oligomers with zwitterionic chain ends, or ionic chain ends containing $Br^{(-)}$, which suggested the influence of ordered structure on the ion conductivity. The HEX structure was able to improve the ion conductivity of oligomers with anions that were small but strongly coordinated with cations, such as $Br^{(-)}$.

These results further demonstrated that amphiphilic oligomers are versatile model materials with many potential applications. They could also offer fundamental understand of oligomers.

References

1. Lohse, D. J.; Hadjichristidis, N., Microphase separation in block copolymers. *Current Opinion in Colloid & Interface Science* **1997,** *2* (2), 171-176.

2. Mai, Y.; Eisenberg, A., Self-assembly of block copolymers. *Chemical Society Reviews* **2012,** *41* (18), 5969-5985.

3. Sinturel, C.; Bates, F. S.; Hillmyer, M. A., High χ–low N block polymers: how far can we go? ACS Publications: 2015.

4. van Genabeek, B.; de Waal, B. F.; Gosens, M. M.; Pitet, L. M.; Palmans, A. R.; Meijer, E., Synthesis and self-assembly of discrete dimethylsiloxane–lactic acid diblock co-oligomers: the dononacontamer and its shorter homologues. *Journal of the American Chemical Society* **2016,** *138* (12), 4210-4218.

5. Oschmann, B.; Lawrence, J.; Schulze, M. W.; Ren, J. M.; Anastasaki, A.; Luo, Y.; Nothling, M. D.; Pester, C. W.; Delaney, K. T.; Connal, L. A.; McGrath, A. J.; Clark, P. G.; Bates, C. M.; Hawker, C. J., Effects of Tailored Dispersity on the Self-Assembly of Dimethylsiloxane–Methyl Methacrylate Block Co-Oligomers. *ACS Macro Letters* **2017,** *6* (7), 668-673.

6. Martínez-Rugerio, G.; Arbe, A.; Colmenero, J.; Alegría, A., Supramolecular self-assembly of monocarboxydecyl-terminated dimethylsiloxane oligomer. *Macromolecules* **2017,** *50* (21), 8688-8697.

7. Nickmans, K.; Bögels, G. M.; Sánchez-Somolinos, C.; Murphy, J. N.; Leclère, P.; Voets, I. K.; Schenning, A. P., 3D Orientational Control in Self-Assembled Thin Films with Sub-5 nm Features by Light. *small* **2017,** *13* (33), 1701043.

8. Nickmans, K.; Jansma, S. O.; Hey, D.; Velpula, G.; Teyssandier, J.; De Feyter, S.; Schenning, A. P., Hydrogen-Bonded Siloxane Liquid Crystals for Hybrid Nanomaterials. *Helvetica Chimica Acta* **2018,** *101* (10), e1800130.

9. Zha, R. H.; Vantomme, G.; Berrocal, J. A.; Gosens, R.; de Waal, B.; Meskers, S.; Meijer, E., Photoswitchable nanomaterials based on hierarchically organized siloxane oligomers. *Advanced Functional Materials* **2018,** *28* (1), 1703952.

10. Kim, J.; Jung, H. Y.; Park, M. J., End-group chemistry and junction chemistry in polymer science: Past, present, and future. *Macromolecules* **2020,** *53* (3), 746-763.

11. Zha, W.; Han, C. D.; Lee, D. H.; Han, S. H.; Kim, J. K.; Kang, J. H.; Park, C., Origin of the Difference in Order− Disorder Transition Temperature between Polystyrene-block-poly (2-vinylpyridine) and Polystyrene-block-poly (4-vinylpyridine) Copolymers. *Macromolecules* **2007,** *40* (6), 2109-2119.

12. Patterson, A. L.; Danielsen, S. P. O.; Yu, B.; Davidson, E. C.; Fredrickson, G. H.; Segalman, R. A., Sequence Effects on Block Copolymer Self-Assembly through Tuning Chain Conformation and Segregation Strength Utilizing Sequence-Defined Polypeptoids. *Macromolecules* **2019,** *52* (3), 1277-1286.

13. Abdullah, O. G.; Hanna, R. R.; Ahmed, H. T.; Mohamad, A. H.; Saleem, S. A.; Saeed, M. A., Conductivity and dielectric properties of lithium-ion biopolymer blend electrolyte based film. *Results in Physics* **2021,** *24*, 104135.

14. Ishai, P. B.; Talary, M. S.; Caduff, A.; Levy, E.; Feldman, Y., Electrode polarization in dielectric measurements: a review. *Measurement science and technology* **2013,** *24* (10), 102001.

15. Ichikawa, T.; Yoshio, M.; Hamasaki, A.; Mukai, T.; Ohno, H.; Kato, T., Self-Organization of Room-Temperature Ionic Liquids Exhibiting Liquid-Crystalline Bicontinuous

Cubic Phases: Formation of Nano-Ion Channel Networks. *Journal of the American Chemical Society* **2007,** *129* (35), 10662-10663.

CHAPTER 5 IMPACTS OF CHAIN ENDS ON MOLECULAR ORGANIZATION OF AMPHIPHILIC oDMS ON OIL/AQUEOUS INTERFACE

Abstract

In this chapter, the effect of inherent cations and anions on the chain packing of oDMS at the oil/aqueous interface was explored. The anions with various characteristics and concentrations from the external environment, such as salts in the aqueous phase, were able to change the conformational properties of oDMS chains by forming ion pairs with the cations at the chain ends. However, the influence of anions from the charged chain ends and cations themselves is still unclear.

Although the inherent anions were low in concentrations and diffused in the aqueous solution compared with external anions, certain ion pairs could form and affect the packing of oDMS chains. Furthermore, the locked cations on the chain ends were able to polarize the water molecules at the oil/aqueous interface by the formed static electric field. In the meantime, the ordered packing of water molecules might influence the chain packing of oDMS chains. In this work, sum frequency generation (SFG) measurement was performed to answer the above questions. As the second-order non-linear optical process, the oDMS chains at the oil/aqueous interface were analyzed. By comparing the peaking amplitude and width, the relative chain packing density and symmetry of oDMS tails were extracted. It will guide the future development of materials with desirable properties for broad applications at various interfaces, such as the oil/aqueous interface.

5.1 Introduction

The development of neuromorphic computing systems requires better alternatives than three-terminal transistors, which are currently being used.[1] For emulating biological synapses, complex circuits were needed by three-terminal transistors and thus energy-consuming.[2] In addition, the scale of three-terminal transistors is limited by the approaching end of Moore's Law.[3] Two-terminal memory elements can be a potential candidate due to their unique properties. As a

history-dependent material, the reconfigurations of two-terminal memory elements at the nanoscale can store and process information.[4, 5] Inspired by nature, Sarles, Collier, and coworkers reported the first example of an interfacial biomimetic lipid-based membrane at the oil/aqueous interface between droplets of aqueous solution in the organic solvent as a novel memory storage device. Controlled by voltage, the lipid bilayer had hysteretic and reversible geometrical changes.[6] However, phospholipid bilayer membranes are weak and fragile. To obtain the stable lipid-based bilayers, oDMS oligomer has been used to replace the fatty acid of phospholipid as the hydrophobic tails, and stable bilayers were able to form at the oil/aqueous interface between droplets of aqueous solution with high salts concentrations in oil.[7]

The macroscopic properties can be influenced by conformational properties. Thus, the chain conformation of oDMS has been studied. To simplify the system, instead of using a bilayer between droplets, the interfacial oDMS chain between oil and the aqueous solution was preferred. We have studied (1) the effect of the external environment, including characteristics and concentrations of anions in the aqueous phase, on the conformation of oDMS tails at the liquid/liquid interface.[8] (2) the structural response of the self-assembly process of oDMS chain to compression at the air-aqueous.[9]

However, the influence of inherent ions from the chemical structures of chain-end modified oligomers on the conformation properties is unknown. With the well-characterized oDMS with different charged chain ends, this work can fulfill this area by exchanging cations or anions under the same external environment. To analyze the molecular organization at the interface, SFG was used in this work, and it has been proved as a powerful tool to extract the needed information from the amplitude and width of the characteristic peak of interfacial samples without the influence of the samples in the bulk mediums.

5.2 Experimental Part

5.2.1 Sample Preparation

Hexadecane was filtered by the 0.2 μm polytetrafluoroethylene (PTFE) filter. Then, the 1 mg/mL solution of the amphiphilic oligomer in hexadecane was prepared at least one night before the measurement. 15 mL of 3-(*N*-morpholino)propanesulfonic acid (MOPS) buffer solution (10 mM in Milli-Q water) was added into a PTFE dish. After dispersing 20 μL of oligomer solution dropwise on the surface of the buffer solution, the oil layer was stabilized for at least 30 mins before measurement.

5.2.2 Sum Frequency Generation (SFG) Measurement

An output beam of approximately 6 W with ~ 40 fs pulses with a repetition rate of 1 kHz centered near 800 nm was provided by a regenerative Ti: Sapphire amplifier from Spectra Physics Spitfire Pro. Two paths were split from the output beam. One path was applied to generate midinfrared (IR) light which centered near 2900 cm^{-1}, by directed this path to an optical parametric amplifier with the different frequency mixer from TOPAS-Prime Plus. With a $4f$-pulse shaper equipped with a two-dimensional liquid crystal on silicon spatial light modulator, another beam was passed through to obtain narrowband near-IR (NIR) up-conversion pulses. In a colinear geometry, the two generated beams were combined and then focused on the sample at ~ 30º regarding the surface horizon. The incident angle of the beam after passing through the interface between air and oil was ~37º at the liquid/liquid interface. A wire-grid polarizer and a Glan-Taylor polarizer were applied to purify the polarization of the IR and NIR beams, separately, followed by the rotation of beams with zero-order half-wave plates. The generated SFG signals at the liquid/liquid interface were collected with a reflection geometry and passed through the following parts: an achromatic half-wave plate, a Glan-Taylor polarizer, and a short-pass filter of 750 nm,

then focused into a charge-coupled device camera at the slit of a spectrograph. The exposure time for each sample was 300 s. With a gold reference spectrum, the background subtraction and normalization of SFG signals were achieved.

5.2.3 Spectral Fitting

In the domain of frequency, the intensity of SFG can be expressed as the following equation:

$$I_{SFG} = \left| \chi_{NR}^{(2)} e^{i\phi} + \sum_{q} \frac{A_q}{\omega_{IR} - \omega_q + i\Gamma_q} \right|^2$$

where $\chi_{NR}^{(2)}$ is the mod-square of the surface second-order susceptibility, and the intensity of SFG is proportional to $\chi_{NR}^{(2)}$, which is contributed by the non-resonant background and the resonant vibrational modes. Then, ω_{IR}, ω_q, Γ_q and A_q are the frequency of IR and resonant transition, line width of the qth-mode, and amplitude of intensity, respectively. In addition, the phase angle is ϕ. The values of these parameters can be extracted by properly fitting the spectra to the above equation. The most important parameter in this work is A_q where the surface coverage and orientation of the sample at the interface can be related. By comparing the values of A_q of different interracial samples, the changes in the conformation of oDMS tails at the interface can be tracked.[8, 10]

5.3 Results and Discussion

Adsorptions of the hydrophilic charged end groups and hydrophobic oDMS chains at the hexadecane/aqueous interface were facilitated and evidenced by the SFG spectrum. The effect of cations and anions from the chain ends on the molecular organization of amphiphilic oligomer at the oil/aqueous interface was discussed in the following sections.

The SFG spectra of oDMS- *MIM$^{(+)}$-OMs$^{(-)}$* was shown in Figure 5.1 and used as an example to explain the SFG signals. The peak assignments were based on the literature for probing PDMS

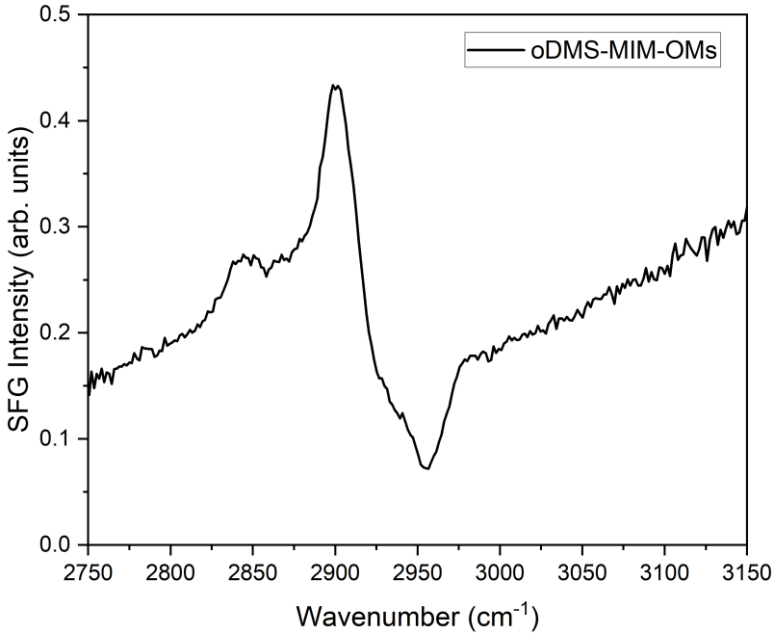

Figure 5.1 SFG spectra (ssp) of oDMS-*MIM*$^{(+)}$*OMs*$^{(-)}$ at hexadecane/buffer solution interfaces.

with SFG.[11] The symmetric stretch of methyl groups on the oDMS chains gave the major peak of the SFG spectrum at around 2910 cm^{-1}. Another peak at around 2880 cm^{-1} represented the stretches of methylene between charged chain ends and oDMS backbones. The broad peak or signal started from around 3000 cm^{-1} was predominantly caused by the stretch of the hydroxyl group of ordered interfacial water molecules, which was polarized and organized by the static electric field created by charged $MIM^{(+)}$. For the charged chain ends, $MIM^{(+)}$ was locked by oDMS backbones and stayed at the interface. However, $OMs^{(-)}$ was free to diffuse in the aqueous phase. Thus, water molecules were polarized and ordered with the $MIM^{(+)}$. To prove the relationship between ordered interfacial water molecules and the broad peak, the presence of high amounts of anions at the interface was introduced to screen the static electric field from charged chain ends. For example, when 1 M of sodium chloride (NaCl) solution was used as the aqueous phase, the SFG spectrum of oDMS- $MIM^{(+)}$-$OMs^{(-)}$ was illustrated in Figure 5.2. After the introduction of $Cl^{(-)}$ at the interface, the broad peak disappeared in Figure 5.2, which indicated the disappearance of ordered water molecules and explained the screen of the interfacial field by forming an electric double layer of $MIM^{(+)}$ and $Cl^{(-)}$. Furthermore, by comparing the amplitudes and widths of the major peaks of different oDMS oligomers, the differences in the oDMS structure were able to distinguish. The fitted parameters were listed in Table 5.1, and the fitted curves were shown in Figure 5.3.

5.3.1 Influences of Cations on Molecular Organization

The effect of cations on charged chain ends was analyzed and shown in Figure 5.4. Based on the results in Table 5.1, the amplitude of the dominant peak of three cations followed the order of $MIM^{(+)} > MMP^{(+)} > Py^{(+)}$. It suggested that $Py^{(+)}$ based charged chain ends gave oDMS tails the lowest packing density, and the conformation of oDMS tails was bent parallel to the interface.

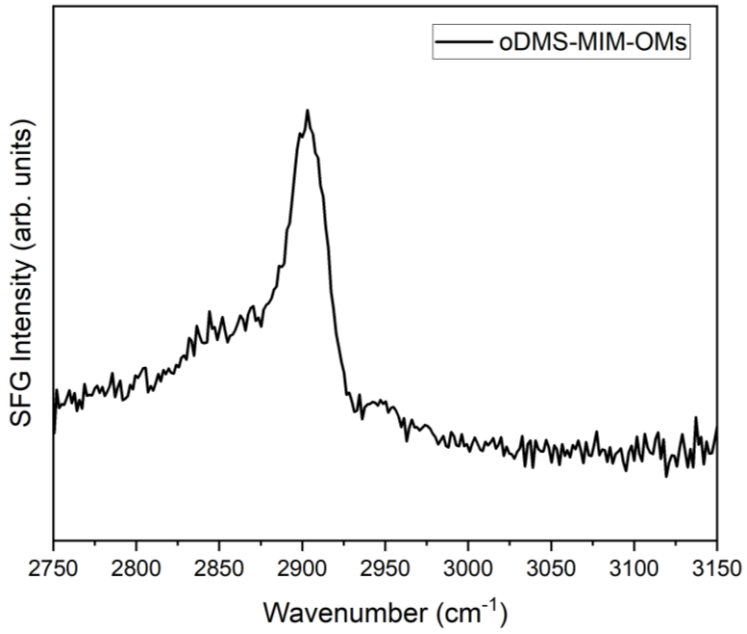

Figure 5.2 SFG spectra (ssp) of oDMS-*MIM* $^{(+)}$*OMs* $^{(-)}$ at hexadecane/NaCl solution (1 M) interfaces.

Table 5.1 Amplitudes and widths of methyl groups obtained by fitting of SFG spectra.

Cation	**Anion**	**Amplitude**	**Width Γ (cm^{-1})**
MIM$^{(+)}$	*OMs*$^{(-)}$	4.2136 ± 0.154	14.342 ± 0.351
	Br$^{(-)}$	3.4513 ± 0.217	14.391 ± 0.735
	OTs$^{(-)}$	3.4608 ± 0.375	13.921 ± 0.852
	OTf$^{(-)}$	3.0605 ± 0.243	13.674 ± 0.746
MMP$^{(+)}$	*OMs*$^{(-)}$	4.1525 ± 0.119	13.668 ± 0.250
Py$^{(+)}$	*OMs*$^{(-)}$	4.1110 ± 0.290	13.507 ± 0.378

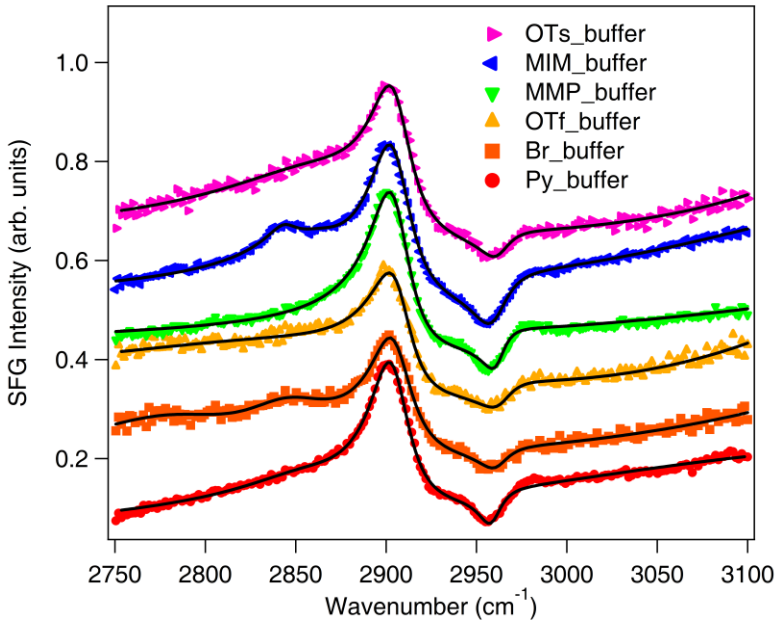

Figure 5.3 SFG spectra (ssp) of amphiphilic oligomers at hexadecane/buffer solution interfaces. The solid points are measured data, and the overlaid curves are the corresponding fitting.

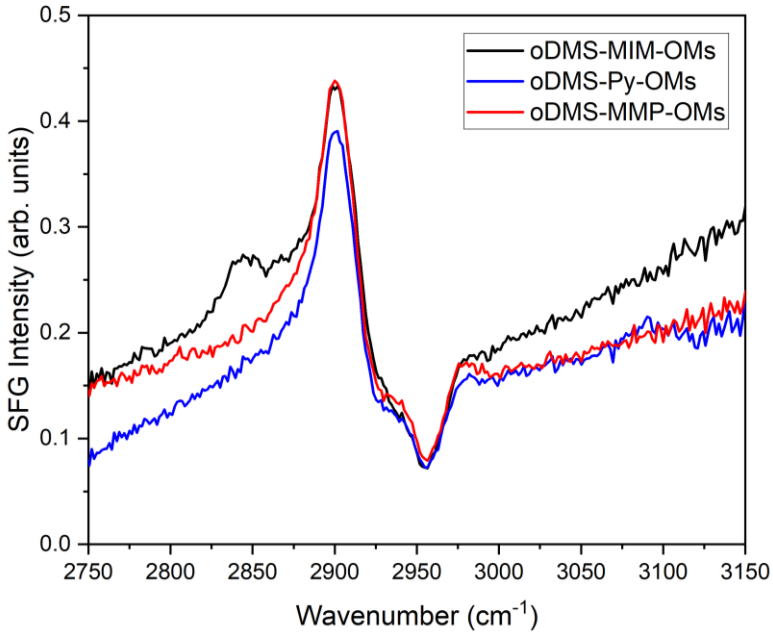

Figure 5.4 SFG spectra (ssp) of oDMS-*MIM* $^{(+)}$*OMs* $^{(-)}$, oDMS-*Py* $^{(+)}$*OMs* $^{(-)}$ and oDMS-*MMP* $^{(+)}$*OMs* $^{(-)}$ at hexadecane/buffer solution interfaces.

$MIM^{(+)}$ based charged chain ends improved the chain packing of oDMS, and the highest packing density was achieved with the oDMS chains were perpendicular to the interface.

When moving to the broad peak for ordered water molecules, $MIM^{(+)}$ had a significantly higher amplitude compared with $MMP^{(+)}$ and $Py^{(+)}$, which might suggest that $MIM^{(+)}$ formed the strongest static electric field among these three cations.

As discussed previously, cations were locked at the interface. But how does cation change the chain packing of oDMS? Our hypothesis was that different degrees of the order of interfacial water molecules, induced by various strengths of the static electric field from cations, affected the chain packing of oDMS as the force between two objects is the same in magnitude but different in direction.

To prove this hypothesis, the static electric field was screened by the introduction of the same anion, $Cl^{(-)}$, and then the SFG spectra of different cations were compared, which was shown in Figure 5.5. After the introduction of $Cl^{(-)}$, the signal of order interfacial water molecules was disappeared. Furthermore, the difference between the amplitude of major peaks was small, and it suggested that the ordered water molecules did influence the oDMS chain packing.

5.3.2 Effects of Inherent Anions on Molecular Organization

Different from the previous research in literature, where the anions were introduced from the aqueous phase, the anions in this work were from the charged end groups, and there were no other anions introduced in the aqueous phase. The anions consisting of charged chain ends were defined as inherent anions in this work to differentiate from the externally introduced anions.

The influence of anions on charged chain ends was studied, and the SFG spectra with different anions were illustrated in Figure 5.6. By exchanging the anions, amplitudes and widths of the major peak were changed. The order of amplitudes was $OMs^{(-)} > OTs^{(-)} > Br^{(-)} > OTf^{(-)}$.

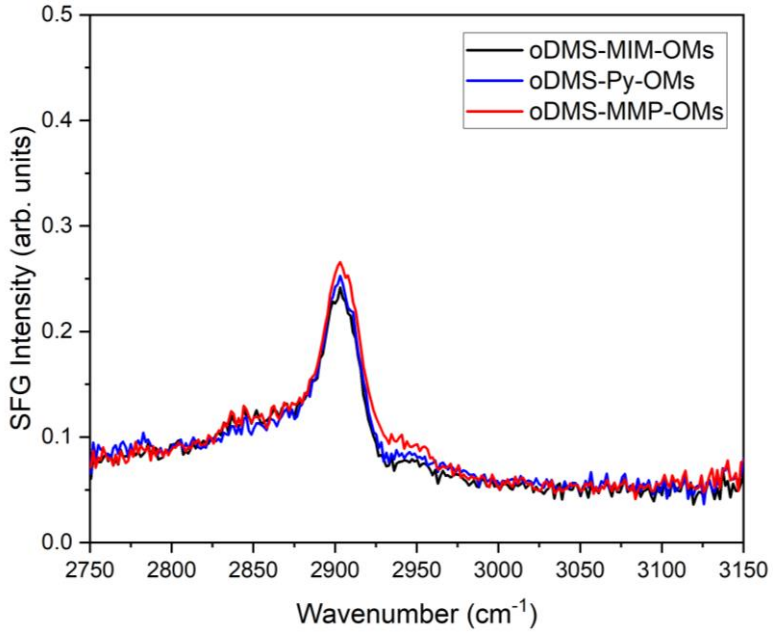

Figure 5.5 SFG spectra (ssp) of oDMS-*MIM* $^{(+)}$*OMs* $^{(-)}$, oDMS-*Py* $^{(+)}$*OMs* $^{(-)}$ and oDMS-*MMP* $^{(+)}$*OMs* $^{(-)}$ at hexadecane/NaCl solution (1 M) interfaces.

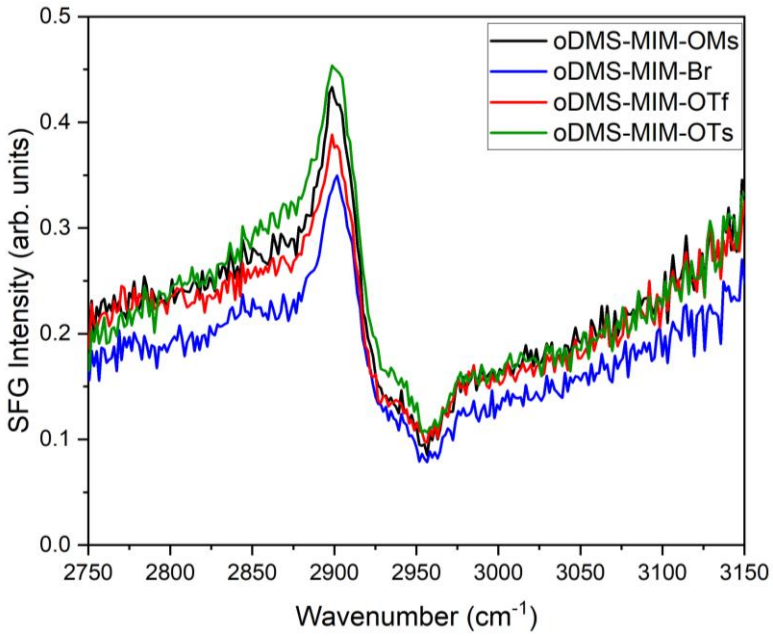

Figure 5.6 SFG spectra (ssp) of oDMS-*MIM* $^{(+)}$*OMs* $^{(-)}$, oDMS-*MIM* $^{(+)}$*Br* $^{(-)}$, oDMS-*MIM* $^{(+)}$*OTf* $^{(-)}$ and oDMS-*MIM* $^{(+)}$*OTs* $^{(-)}$ at hexadecane/buffer solution interfaces.

Thus, $OMs^{(-)}$ offered the best centrosymmetric and tightly packed conformations, while $OTf^{(-)}$ suppressed the centrosymmetry of conformations and loosed the packing of oDMS chains. Based on the results in this work, the inherent anions were able to tune the conformations of oDMS chains, even though the concentrations of inherent anions were extremely low compared with the externally introduced anions. Furthermore, according to the conformation change of oDMS chains, the relative hardness or softness of anions can be sorted that ion pairs formed with soft anions were able to improve the packing of oDMS chains. From relative soft to relative hard anions, the inherent anions had the order of $OMs^{(-)} > OTs^{(-)} > Br^{(-)} > OTf^{(-)}$ for $MIM^{(+)}$ based ion pairs.

5.4 Conclusion

In this chapter, the effects of cations and anions from the charged chain ends on the conformations of oDMS chains were studied. Compared with the external ions, the charged chain ends only provided a low concentration of cations and anions while they were able to tune the chain packing of oDMS significantly. For the cations, $MIM^{(+)}$ based charged chain ends improved the chain packing of oDMS tails at the interface, while $Py^{(+)}$ based charged chain ends lowered the packing density. The cations influenced the chain packing of oDMS by inducing the ordering of interfacial water molecules. In terms of inherent anions, the order of inherent anions was $OMs^{(-)} > OTs^{(-)} > Br^{(-)} > OTf^{(-)}$ from relative soft to hard anions when formed ion pairs with cations of $MIM^{(+)}$. The charged chain ends were once again demonstrated to able to tune the packing of oligomers chains at the interface.

References

1. Mead, C., Neuromorphic electronic systems. *Proceedings of the IEEE* **1990,** *78* (10), 1629-1636.

2. Williams, R. S., How We Found The Missing Memristor. *IEEE Spectrum* **2008,** *45* (12), 28-35.

3. Williams, R. S., What's Next?[The end of Moore's law]. *Computing in Science & Engineering* **2017,** *19* (2), 7-13.

4. Di Ventra, M.; Pershin, Y. V., The parallel approach. *Nature Physics* **2013,** *9* (4), 200-202.

5. Chua, L. O., Nonlinear circuit foundations for nanodevices. I. The four-element torus. *Proceedings of the IEEE* **2003,** *91* (11), 1830-1859.

6. Najem, J. S.; Hasan, M. S.; Williams, R. S.; Weiss, R. J.; Rose, G. S.; Taylor, G. J.; Sarles, S. A.; Collier, C. P., Dynamical nonlinear memory capacitance in biomimetic membranes. *Nature Communications* **2019,** *10* (1), 3239.

7. Taylor, G. J.; Luo, Y.; Hong, K.; Sarles, S. A.; Sacci, R. L.; Doughty, B.; Collier, C. P., Self-Assembly of Charged Oligomeric Bilayers at the Aqueous/Organic Interface Regulated by Ion-Pair Associations. **2020**.

8. Lin, L.; Chowdhury, A. U.; Ma, Y.-Z.; Sacci, R. L.; Katsaras, J.; Hong, K.; Collier, C. P.; Carrillo, J.-M. Y.; Doughty, B., Ion Pairing Mediates Molecular Organization Across Liquid/Liquid Interfaces. *ACS Applied Materials & Interfaces* **2021,** *13* (28), 33734-33743.

9. Liu, Z.; Lin, L.; Li, T.; Kinnun, J.; Hong, K.; Ma, Y.-Z.; Sacci, R. L.; Katsaras, J.; Carrillo, J.-M.; Doughty, B.; Collier, C. P., Squeezing Out Interfacial Solvation: The Role of Hydrogen-Bonding in the Structural and Orientational Freedom of Molecular Self-Assembly. *The Journal of Physical Chemistry Letters* **2022**, 2273-2280.

10. Ohno, P. E.; Saslow, S. A.; Wang, H.-f.; Geiger, F. M.; Eisenthal, K. B., Phase-referenced nonlinear spectroscopy of the α-quartz/water interface. *Nature Communications* **2016,** *7* (1), 13587.

11. Kim, C.; Gurau, M. C.; Cremer, P. S.; Yu, H., Chain conformation of poly (dimethyl siloxane) at the air/water interface by sum frequency generation. *Langmuir* **2008,** *24* (18), 10155-10160.

CHAPTER 6 CONCLUSION, FUTURE WORK, AND PERSPECTIVE

6.1 Conclusions

In summary, this dissertation was aimed at developing charged chain-end modified oligodimethylsiloxanes (oDMS) and studying their properties: (1) Improved thermal properties; (2) Tunable sub-10 nm structures with various morphologies, domain spacings, and order-disorder transition temperatures by exchanging of ions; (3) Stable absorption at the oil/aqueous interface with different pack densities and symmetries of oDMS chains.

A library of oDMS with ionic and zwitterionic chain ends was synthesized by chain end modification of the terminated mono-hydroxyl groups of oDMS. Different synthetic approaches were explored and compared to improve the conversions and efficiency of reactions. In the dissertation, the synthetic routes without involving any metals (metal-free) and scalable methods with high conversions were used. The purity of obtained materials was confirmed by ^{1}H NMR with the chemical shifts of characteristic signals from end groups. Furthermore, molecular weights, dispersities, and end groups were analyzed by MALDI-TOF MS with the matching of the calculated and theoretical numbers, which indicated the quality of the samples.

The effect of charged chain ends on different properties was then investigated. The thermal stability of these amphiphilic oligomers, which has profound implications in their applications, was first studied. Most charged chain ends improved the thermal stability except $MIM^{(+)}Br^{(-)}$ degraded the oDMS backbones. A complicated thermal degradation mechanism was suggested by the broader temperature range for weight loss compared with molecular ionic liquids and the higher weight loss compared with the unfunctionalized oligomer.

As two incompatible elements, hydrophilic charged chain ends and hydrophobic oDMS chains offered amphiphilic oligomers the ability of phase separation as block co-oligomers or copolymers. Revealing be SAXS, sub-10 nm structures were formed with various morphologies,

domain spacings, and order-disorder transition temperatures dictated by the characteristics of cations, anions, or zwitterion. The order-disorder transition was further examined by dielectric spectroscopy (DS). Compared with anions, cations significantly changed the phase behaviors with the order of $MMP^{(+)} > Py^{(+)} > MIM^{(+)}$ for the anion of $OMs^{(-)}$, which may be related to the conjugated structure of cations and size of anions. Regarding incompatibility between oDMS chains and charged chain ends, repulsions from pyridinium-based chain ends were stronger than imidazolium-based chain ends. Furthermore, as the ion conductive oligomers, both characteristics of charged chain ends and ordered structures influence the ion conductivity. Cations affected the ion conductivity based on their segregation strengths, and anions tuned the ion conductivity with their size and coordination ability. For the ordered structure, hexagonally-packed cylinders were able to improve the ion conductivity of amphiphilic oligomers with anions that were small but strongly coordinated.

These amphiphilic oligomers, which mimic the structures of lipids, were able to absorb at the oil/aqueous interface. To understand the effect of inherent chemical structure on the chain packing of oDMS, interfacial amphiphilic oligomers under the same environment were analyzed by sum-frequency generation (SFG). For the impact of cations from the chain ends, $MIM^{(+)}$ improved the oDMS chain packing while $Py^{(+)}$ lowered the packing density by the interfacial ordered water molecules caused by static electric fields from cations. In terms of anions on charged chain ends, although their low concentrations compared with external anions from aqueous solutions, the formed ion pairs still affected the chain packing of the oDMS tail with the order from soft to hard anions as $OMs^{(-)} > OTs^{(-)} > Br^{(-)} > OTf^{(-)}$.

These amphiphilic oligomers were good model materials for understanding the charged materials. Furthermore, the stable structures of lipid-similar amphiphilic oligomers at the

oil/aqueous interface provided a suitable platform for the study of medium transfer between interfaces and the potential lipid-based memcapacitor for neuromorphic computing.

6.2 Future Work and Perspectives

The following future work will be finished to tell a comprehensive story of this work:

(1) Synthesis of oligodimethylsiloxane tertiary amino 1-propanesulfonic acid (oDMS-$NH(CH_3)_2^{(+)}CH_3(CH_2)_2SO_3^{(-)}$). Most chain ends were successfully introduced to oDMS backbone. However, the end group of tertiary amino methanesulfonic acid was not obtained because it degraded the oDMS chain at room temperature. This end group was designed as the counterpart of zwitterion, sulfobetaine, to compare the differences in properties caused by the covalent bonds at end groups. Although other ionic chain ends can be used for this purpose, the cation and anion in these ionic chain ends are different from zwitterion, and it will influence the results, especially chain packing of oDMS at the oil/aqueous interface due to the different characteristics of $SO_3^{(-)}$ with other anions in this work. Based on our previous experiments, the degradation of oDMS chains was reduced by inducing more methyl groups on $SO_3^{(-)}$. Sulfuric acid, $SO_4^{(-)}$, damaged the oDMS chains in hours, while methanesulfonic acid, $CH_3SO_3^{(-)}$, needed three days. Obviously, the low acidity of anion reduced the damage of -Si-O- bonds. Thus, 1-propanesulfonic acid, $CH_3(CH_2)_2SO_3^{(-)}$, is expected to obtain a stable sample at room temperature. Due to delayed shipment (1 year) of chemicals caused by the pandemic, we do not receive it yet. The synthesis work of oDMS-$NH(CH_3)_2^{(+)}CH_3(CH_2)_2SO_3^{(-)}$ will be finished soon once we receive the chemical. Then, the chain ends of zwitterion and ionic liquid can be compared with the only difference in the connection method of ions.

(2) Characterization of obtained morphologies with image techniques. The sample macroscopic morphologies have been analyzed by SAXS, while the image of the local area on the

sample will give a direct insight of the morphology. Based on the previous trials on TEM imaging, the morphology was not clear due to the low contrast between oDMS chains and charged chain ends. Elemental mapping with TEM may solve this problem. The morphology can be analyzed by the distributions of elements of Si and N. Furthermore, the changes in local morphology can be imaged at various temperatures to monitor the order-disorder transitions.

For the perspectives, this work explored the bulk and interfacial properties of amphiphilic oligomers. Other intriguing topics are still worth further investigation: (1) Solution properties of amphiphilic oligomers. (2) Properties of amphiphilic oligomers with branching tails and different types of tails.

Due to the incompatibility between hydrophobic oDMS chains and hydrophilic charged chain ends, the self-assembly of amphiphilic oligomers is also expected to occur in solutions. The effect of charged chain ends, and other parameters on self-assembly behavior needs more exploration.

We studied the effect of charged chain end and good solvents, and preliminary results were discussed next. A stock solution of amphiphilic oligomers in good solvents was prepared and added into a mixture of good solvent and water to make the final concentration of oligomers as 1.8 mg/mL. After equilibrium for three days, the formed structures were analyzed by dynamic light scattering. Reverse vesicles were observed with various sizes and distributions resulting from different charged chain ends and types of good solvents. The effect of the solvent was shown in Figure 7.1. Based on previous studies, tetrahydrofuran (THF) is a better solvent for PDMS than acetone.[1, 2] Thus, the better solvent for oDMS gave the improved distributions that three distributions in acetone/water mixture while single distribution in THF/water mixture. For the charged chain ends, the charged density of charged chain ends affects the self-assembly of

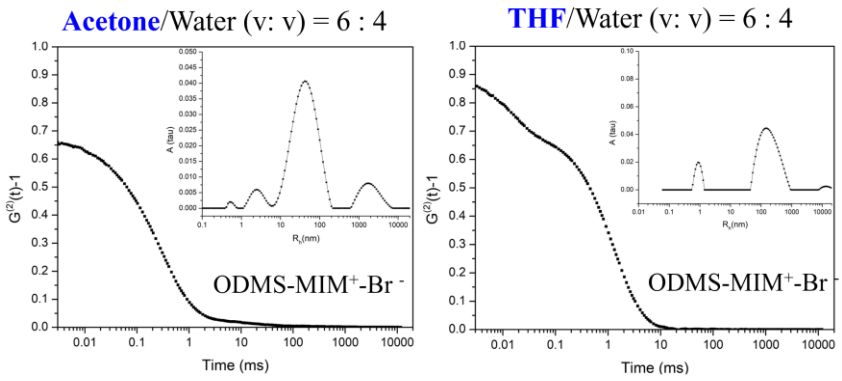

Figure 7.1 Effect of good solvent on the distributions of vesicles.

amphiphilic oligomers, which was illustrated in Figure 7.2. All charged chain ends have the same number of charges, while the size of counterions/zwitterion is different. The order of size of charged chain ends is zwitterion > $MIM^{(+)}OMs^{(-)}$ > $MIM^{(+)}Br^{(-)}$, thus, the order of charge density followed the opposite direction as $MIM^{(+)}Br^{(-)}$> $MIM^{(+)}OMs^{(-)}$ > zwitterion. According to the distribution of vesicles, lower charged density improved the distributions and increased the size of vesicles. Although the single distribution of certain oligomers with charged chain ends was achieved, other important variables are largely unexplored, including concentrations of oligomers,[3] types and strengths of external anions,[4, 5] pH values,[6, 7] and temperatures.[8, 9] Furthermore, the formed structures are assumed as vesicles. Cryogenic-TEM (cryo-TEM) can be applied to examine the assembled structure.[10] Novel structures in solution might be created by the charged chain ends.

This work studied the linear amphiphilic oligomers while the natural lipids have two hydrophobic tails and one charged chain ends. There are several parameters for hydrophobic tails that can tune the properties of amphiphilic oligomers: (1) Architecture of oDMS. Xue and coworkers compared linear and branched $MIM^{(+)}NTf_2^{(-)}$ with n-alkyl chains, and the viscosity of branched ILs was higher than that of linear ILs at room temperature to 50 °C.[11] Thus, with branching on the oDMS tails, the viscosity of oligomers will increase, and it may also increase the mobility of charged chain ends, which will improve the ion conductivity of amphiphilic oligomers. (2) Molecular weight (MW) of oDMS. The lower the MW of tails, the higher weight fraction of charged chain ends. So, a more significant effect of charged chain ends on the properties of amphiphilic oligomers is excepted. For example, the higher ratio of order phase may obtain, and the degree of the internal order of structure can be improved. (3) Types of backbones. Different backbones will significantly change the properties of oligomers. If oligostyrene, whose glass

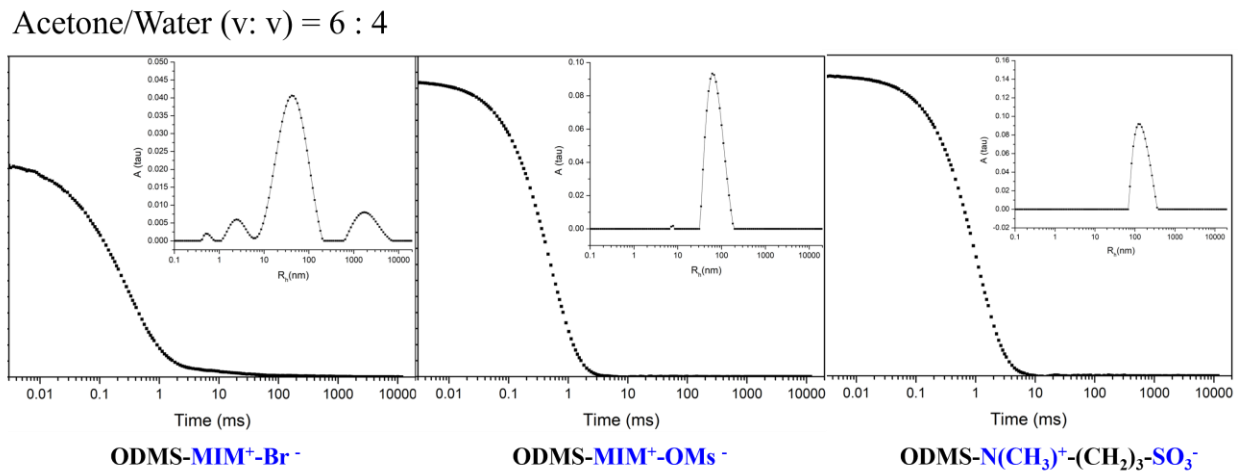

Figure 7.2 Effect of charged chain ends on the self-assembly of vesicles.

transition temperature is 15 °C for MW of 1 kg/mol,[12] was applied as the tail, the solid or strong gel-like amphiphilic oligomers may be developed to fabricate membranes for various applications without the mechanical support of matrix. Furthermore, specific inherent distinctive properties can be introduced by the characteristics of backbones. For example, when oligo(lactic acid) or oligocaprolactone was used as the backbone of amphiphilic oligomers, the biocompatible and biodegradable materials may be developed to meet the requirements of *in vivo* applications. We believe there are many new structures, properties, and functionalities based on charged oligomers to be discovered.

References

1. Lee, J. N.; Park, C.; Whitesides, G. M., Solvent compatibility of poly (dimethylsiloxane)-based microfluidic devices. *Analytical chemistry* **2003,** *75* (23), 6544-6554.

2. Kleiman, M.; Ryu, K. A.; Esser-Kahn, A. P., Determination of Factors Influencing the Wet Etching of Polydimethylsiloxane Using Tetra-n-butylammonium Fluoride. *Macromolecular Chemistry and Physics* **2016,** *217* (2), 284-291.

3. Rudra, J. S.; Collier, J. H., 2.205 - Self-Assembling Biomaterials. In *Comprehensive Biomaterials*, Ducheyne, P., Ed. Elsevier: Oxford, 2011; pp 77-94.

4. Kim, H. J.; Wang, W.; Bu, W.; Hossen, M. M.; Londoño-Calderon, A.; Hillier, A. C.; Prozorov, T.; Mallapragada, S.; Vaknin, D., Salt Mediated Self-Assembly of Poly(ethylene glycol)-Functionalized Gold Nanorods. *Scientific Reports* **2019,** *9* (1), 20349.

5. Borisov, O. V.; Zhulina, E. B., Effect of Salt on Self-Assembly in Charged Block Copolymer Micelles. *Macromolecules* **2002,** *35* (11), 4472-4480.

6. Karayianni, M.; Pispas, S., Block copolymer solution self-assembly: Recent advances, emerging trends, and applications. *Journal of Polymer Science* **2021,** *59* (17), 1874-1898.

7. Ghosh, A.; Haverick, M.; Stump, K.; Yang, X.; Tweedle, M. F.; Goldberger, J. E., Fine-Tuning the pH Trigger of Self-Assembly. *Journal of the American Chemical Society* **2012,** *134* (8), 3647-3650.

8. Wolf, T.; Rheinberger, T.; Simon, J.; Wurm, F. R., Reversible Self-Assembly of Degradable Polymersomes with Upper Critical Solution Temperature in Water. *Journal of the American Chemical Society* **2017,** *139* (32), 11064-11072.

9. Lan, X.; Ma, X.; Wang, L.; Shi, Y.; Gu, Q.; Wu, L.; Gu, X.; Luo, Z., Self-Assembly of Diblock Copolymers Containing Thermo- and Photoresponsive Lower Critical Solution

Temperature Phase Behavior Polymer with Tunable Assembly Temperature in an Ionic Liquid Mixture. *ACS Omega* **2019,** *4* (6), 11229-11236.

10. Sternhagen, G. L.; Gupta, S.; Zhang, Y.; John, V.; Schneider, G. J.; Zhang, D., Solution Self-Assemblies of Sequence-Defined Ionic Peptoid Block Copolymers. *Journal of the American Chemical Society* **2018,** *140* (11), 4100-4109.

11. Xue, L.; Gurung, E.; Tamas, G.; Koh, Y. P.; Shadeck, M.; Simon, S. L.; Maroncelli, M.; Quitevis, E. L., Effect of Alkyl Chain Branching on Physicochemical Properties of Imidazolium-Based Ionic Liquids. *Journal of Chemical & Engineering Data* **2016,** *61* (3), 1078-1091.

12. Hatakeyama, T.; Serizawa, M., Glass Transition of Oligostyrene with Different End Groups. *Polymer Journal* **1982,** *14* (1), 51-57.

Appendix

Summary of Ph. D. Projects

This dissertation focused on the effects of charged chain ends on the properties of amphiphilic oligomers to present a coherent story. Other projects have been done during the Ph. D. study but not included in this dissertation are briefly summarized in the Appendix.

(1) Chain flexibility and glass transition temperatures of poly(n-alkyl (meth)acrylate)s: implications of tacticity and chain dynamics. In this work, the relationship between the microstructure of poly(n-alkyl methacrylate)s and poly(n-alkyl acrylate)s and their properties were explored, including solution properties, chain conformation indicated by Flory's characteristic ratio, persistence length, and chain diameters, and glass transition temperatures. More details can be found in the published paper: *Polymer* **2021**, 213, 123207.

(2) Decoupling of side-chain and backbone conformation of bottlebrush polymers by selective deuteration and neutron scattering. In this work, the effect of side-chain lengths and concentrations of bottlebrush polymers on their conformation properties were studied. Compared with previous works in literature, instead of treating bottlebrush polymers as the cylinders formed by side chains and backbones, the side chain and backbones were decoupled and analyzed separately. Thus, the conformation information of backbones was not shielded by the signals from side chains, and accurate results were able to obtain. The norbornene-based bottlebrush polymers with side chains of poly(methyl methacrylate) were synthesized by ring-opening metathesis polymerization of functionalized macroinitiators with 3^{rd} generation of Grubbs catalyst, which was illustrated in Scheme S1. In addition, the deuterated side chains were introduced by a similar procedure. Distinguishing of scattering from the backbone or side chains was achieved by contrast-variation (CV) experiments. By replacing hydrogen with deuterium, the scattering length density

(SLD) of polymers can be significantly enhanced. Then the partially deuterated polymers were placed in mixtures of various ratios of deuterated and hydrogenated solvents, and the contrast factors of different parts of the polymer were changed. Thus, the chain conformation of the backbone and side chains were decoupled.

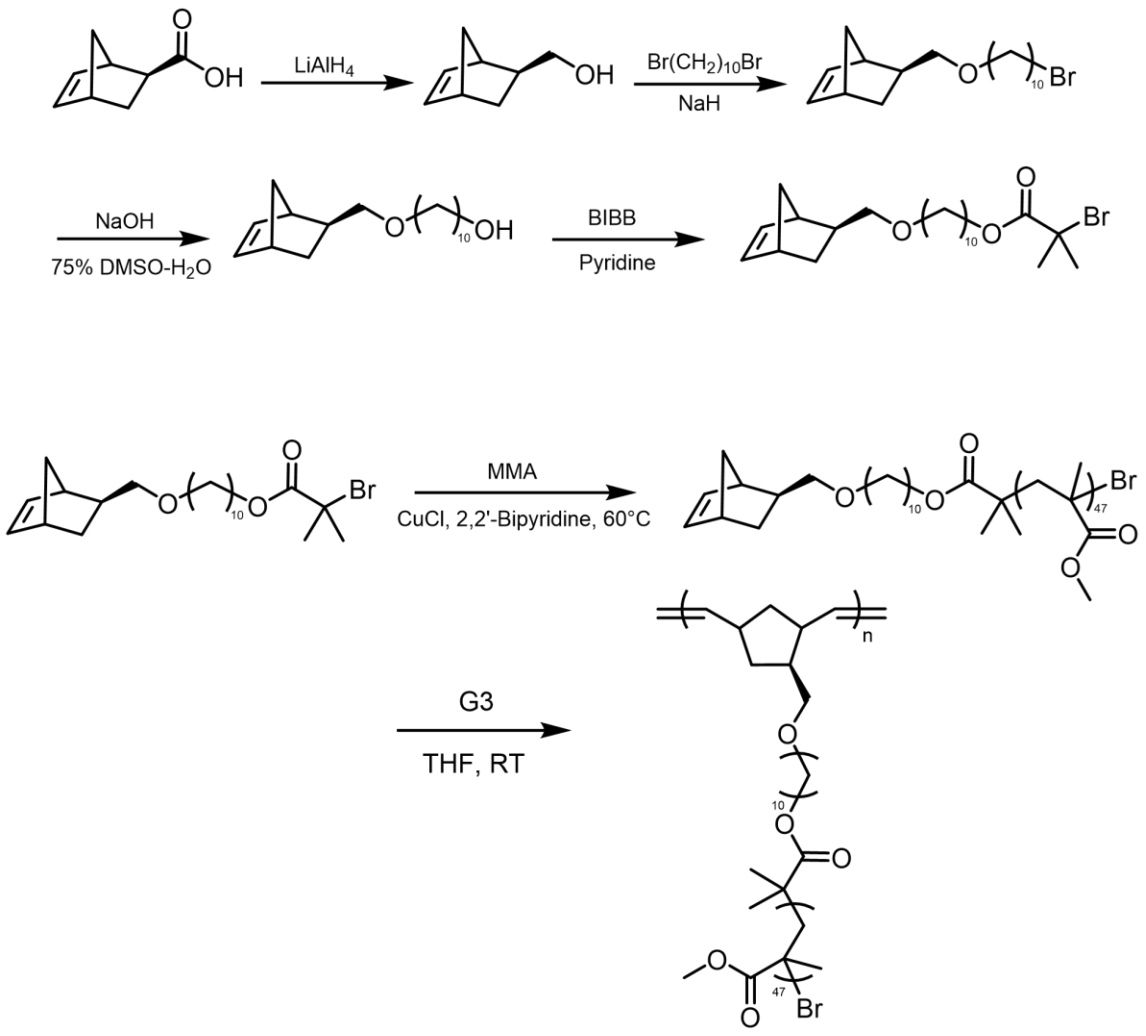

Scheme S1. Synthesis of bottlebrush polymers.

(3) Effects of charged chain ends on bulk properties of amphiphilic block polymeric ionic

liquids. Block copolymers containing ionic moieties are attractive materials because they combine benefits from both ionic liquids and block copolymers, where the ionic liquids exhibit unique physicochemical properties and block copolymers self-assemble into the various nanostructures. A set of well-defined block copolymers of ionic liquids was developed by the described methods in Chapter 2, which proves the universality of the synthetic method and the synthetic routes were shown in Scheme S2. Starting from the reversible addition−fragmentation chain-transfer (RAFT) agent, chain extensions with ethyl methacrylate then 2-hydroxyethyl methacrylate were achieved to produce the parent block copolymer with controlled molecular weights and narrow dispersity, followed by pendant group modifications of hydroxyl groups to obtain the final block copolymers of ionic liquids as the solids instead of weak gel. Thus, the free-standing films can be fabricated without the support of a matrix, which will be convenient for further studies and applications. With the materials developed in this work, the simple exchange of cations and anions can lead to different morphologies without influencing molecular weight, dispersity, and block compositions. The materials can be a potential platform for the topic area of the morphology/domain spacing-property relationship.

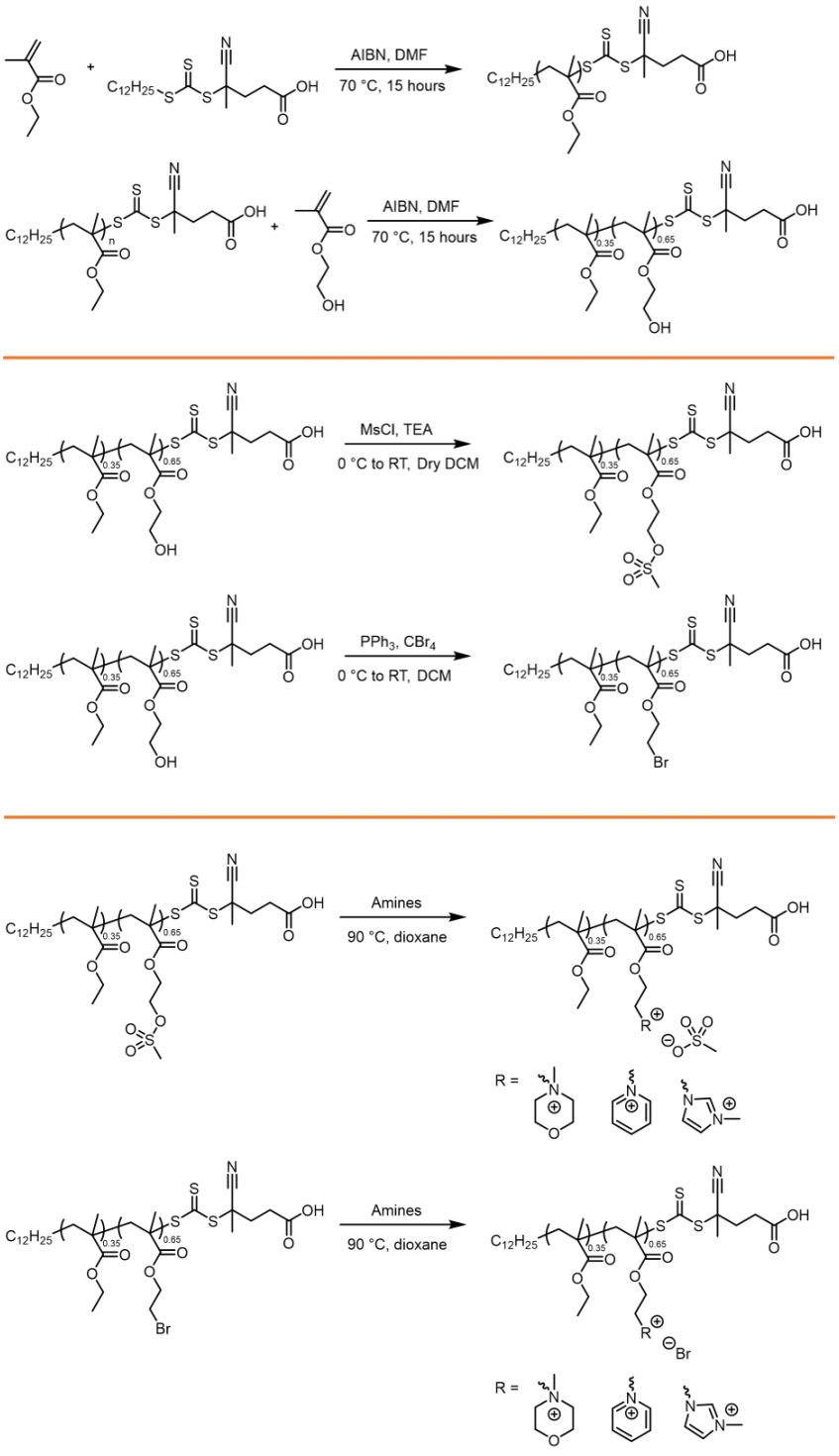

Scheme S2. Synthesis of block copolymers containing ionic moieties

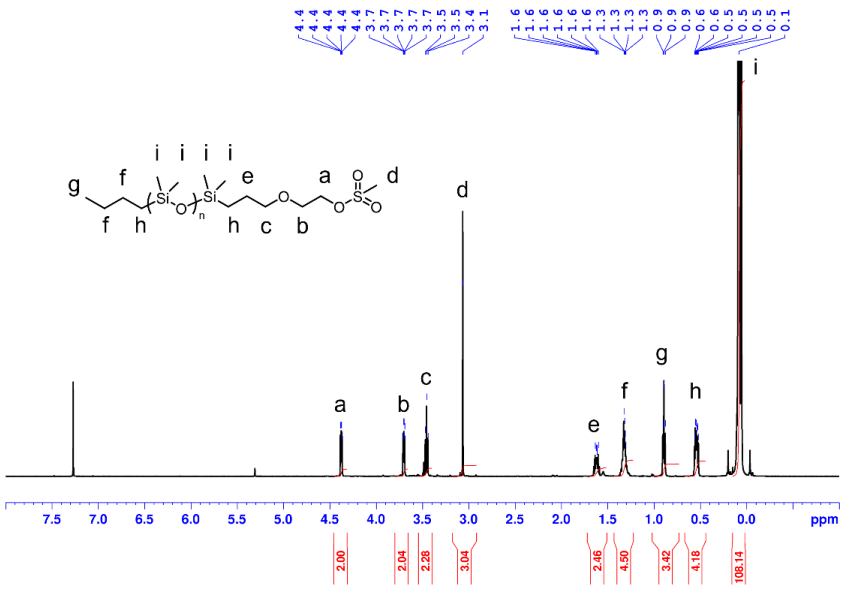

Figure S1 ^{1}H NMR spectrum of oDMS-*OMs*.

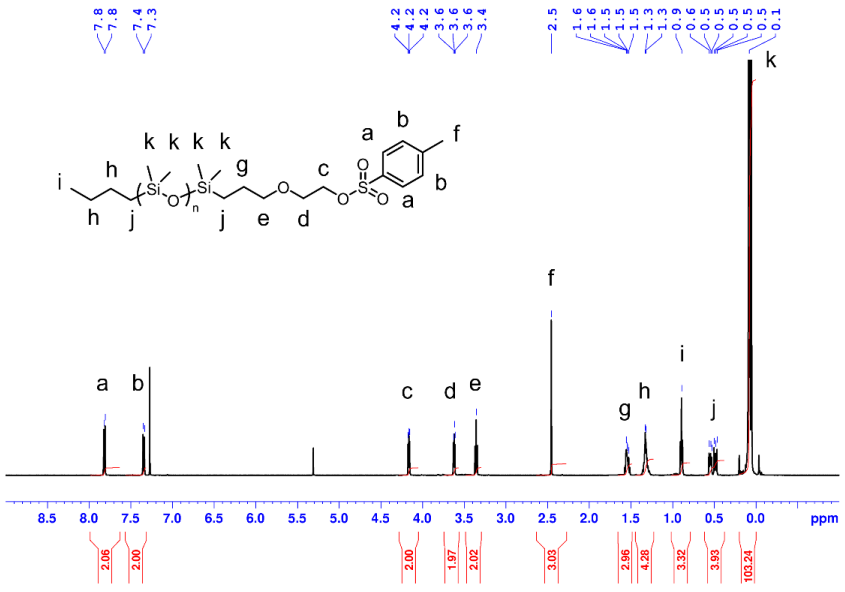

Figure S2 ^{1}H NMR spectrum of oDMS-*OTs*.

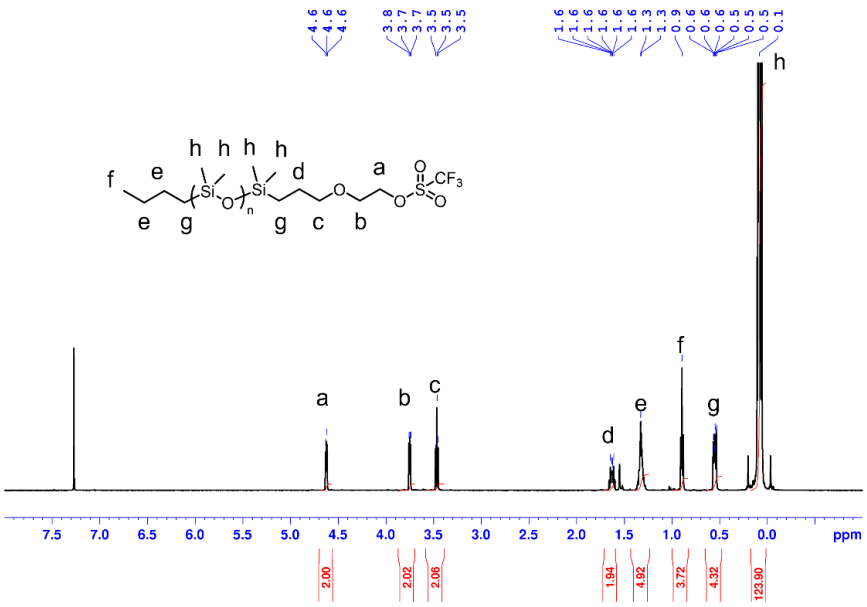

Figure S3 [1]H NMR spectrum of oDMS-*OTf*.

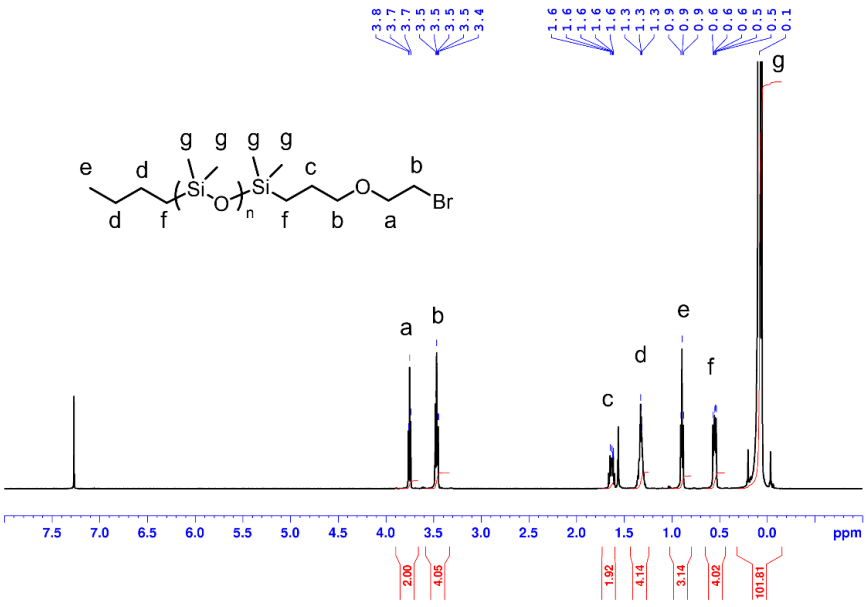

Figure S4 [1]H NMR spectrum of oDMS-*Br*.

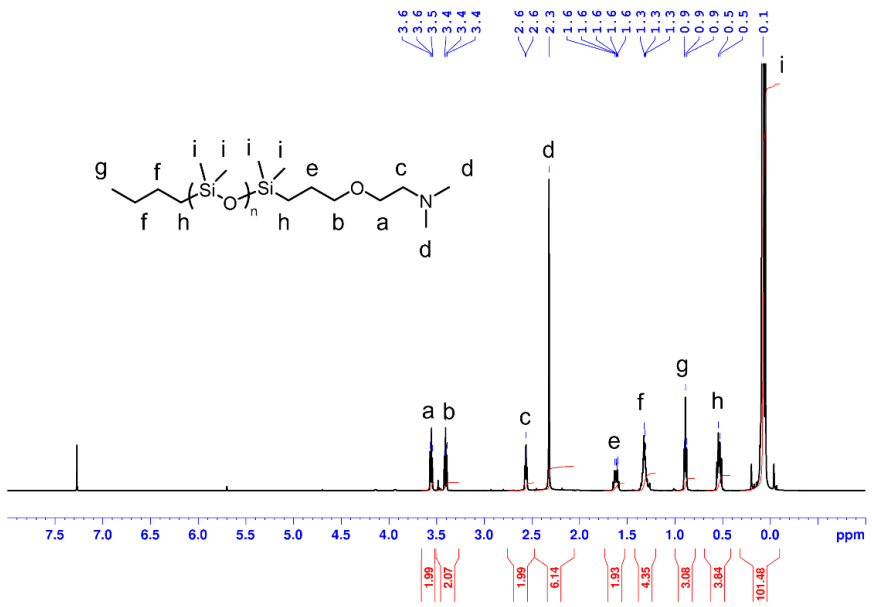

Figure S5 ^{1}H NMR spectrum of oDMS-*N(CH$_3$)$_2$*.

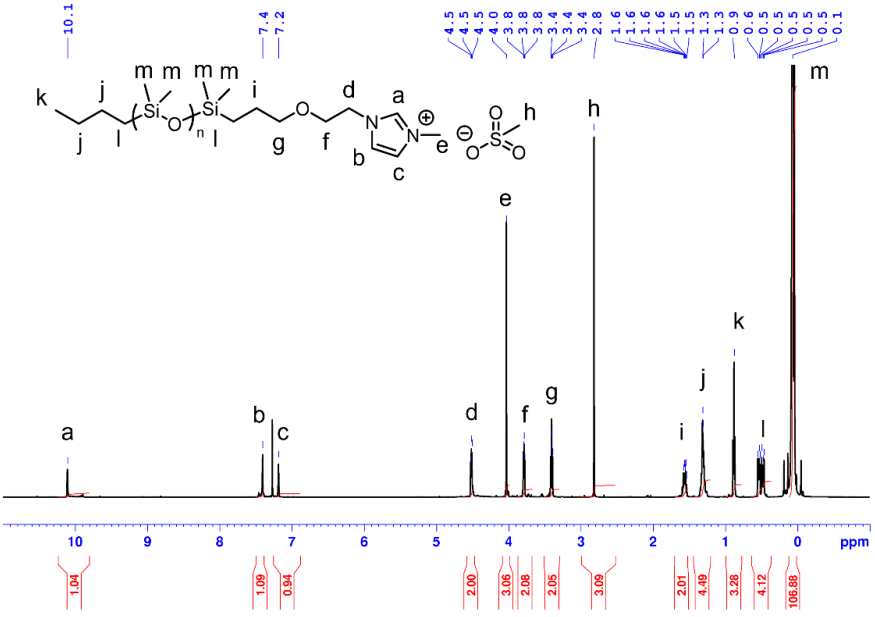

Figure S6 ^{1}H NMR spectrum of oDMS-*MIM$^{(+)}$OMs$^{(-)}$*.

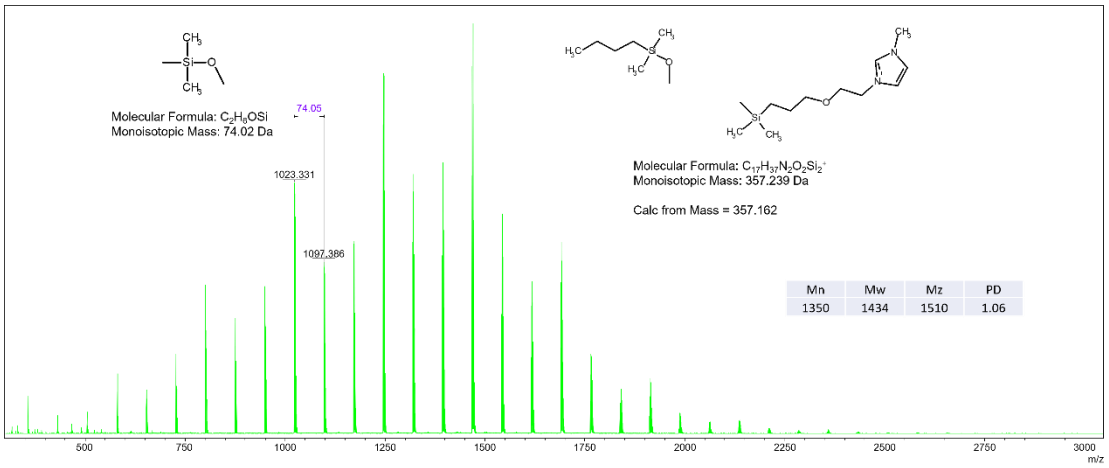

Figure S7 MS spectrum of oDMS-*MIM*$^{(+)}$*OMs*$^{(-)}$.

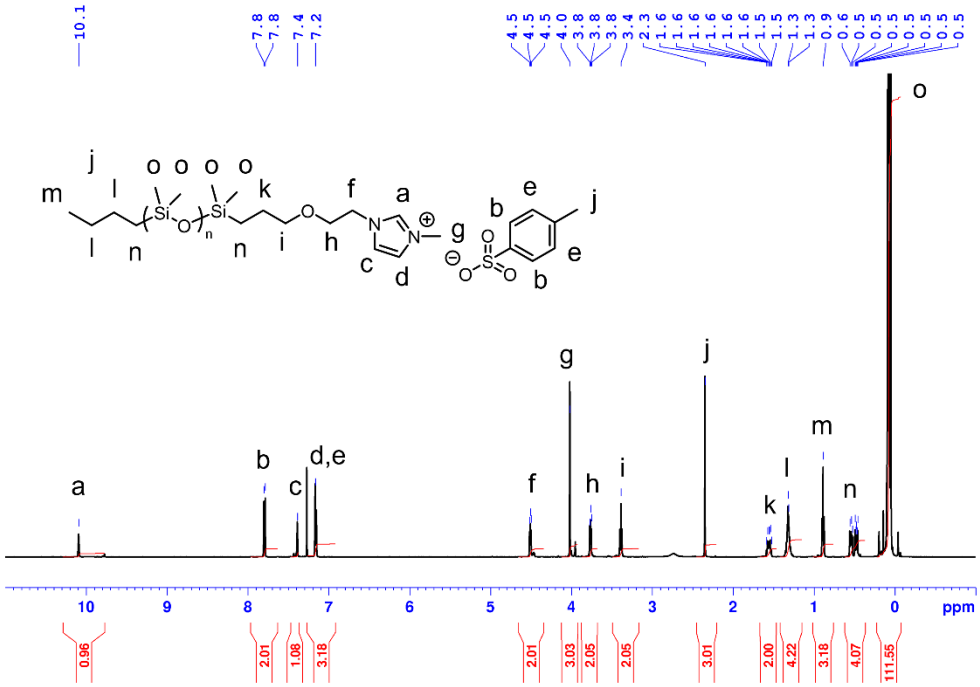

Figure S8 ^{1}H NMR spectrum of oDMS-*MIM*$^{(+)}$*OTs*$^{(-)}$.

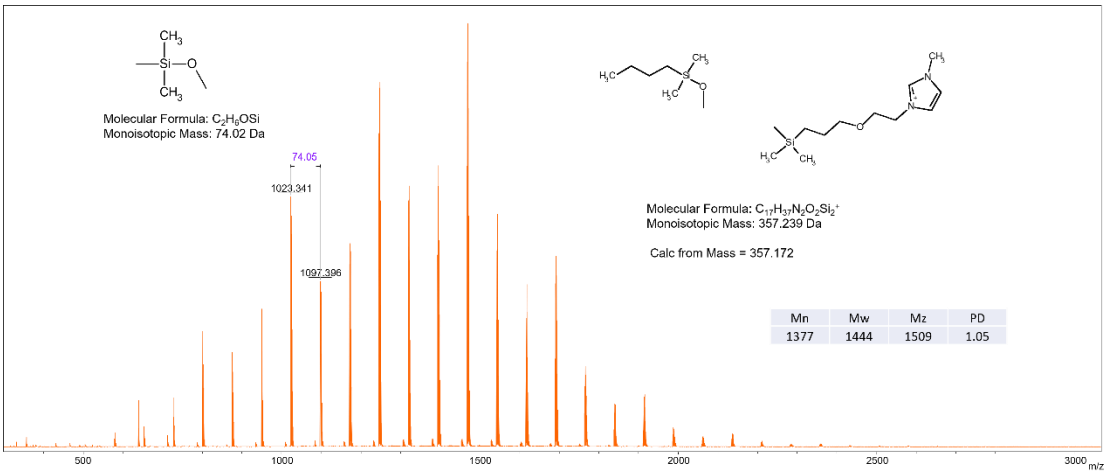

Figure S9 MS spectrum of oDMS-*MIM*$^{(+)}$*OTs*$^{(-)}$.

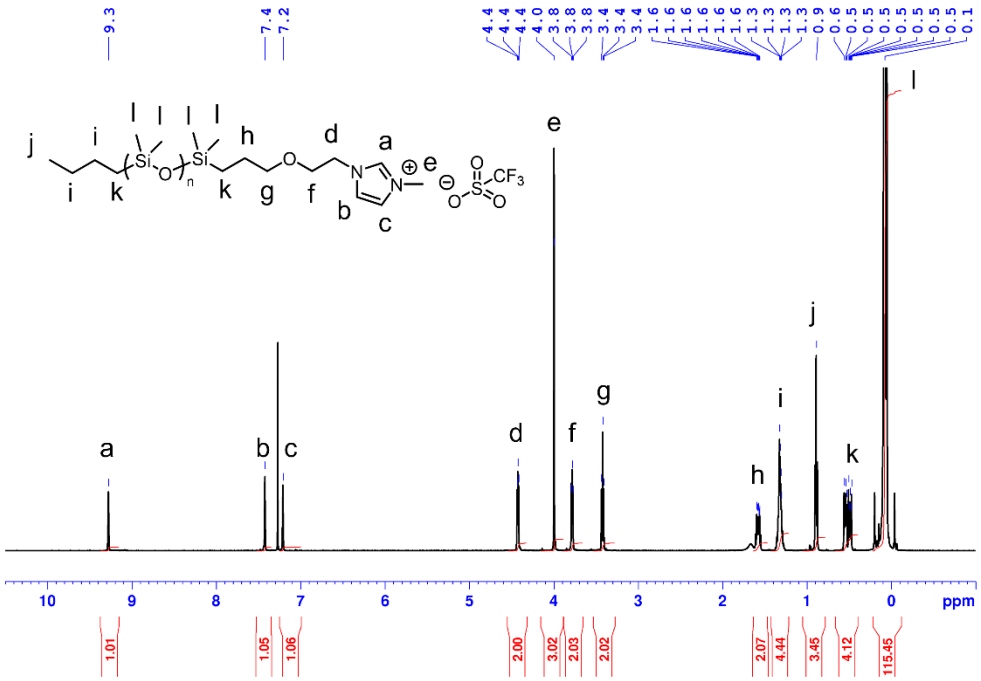

Figure S10 ^{1}H NMR spectrum of oDMS-*MIM*$^{(+)}$*OTf*$^{(-)}$.

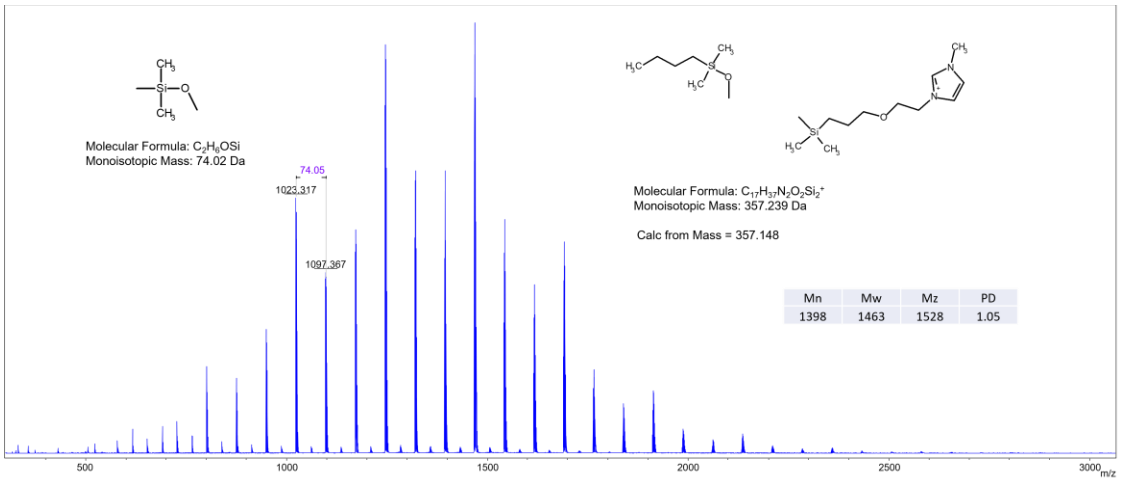

Figure S11 MS spectrum of oDMS-*MIM*$^{(+)}$*OTf*$^{(-)}$.

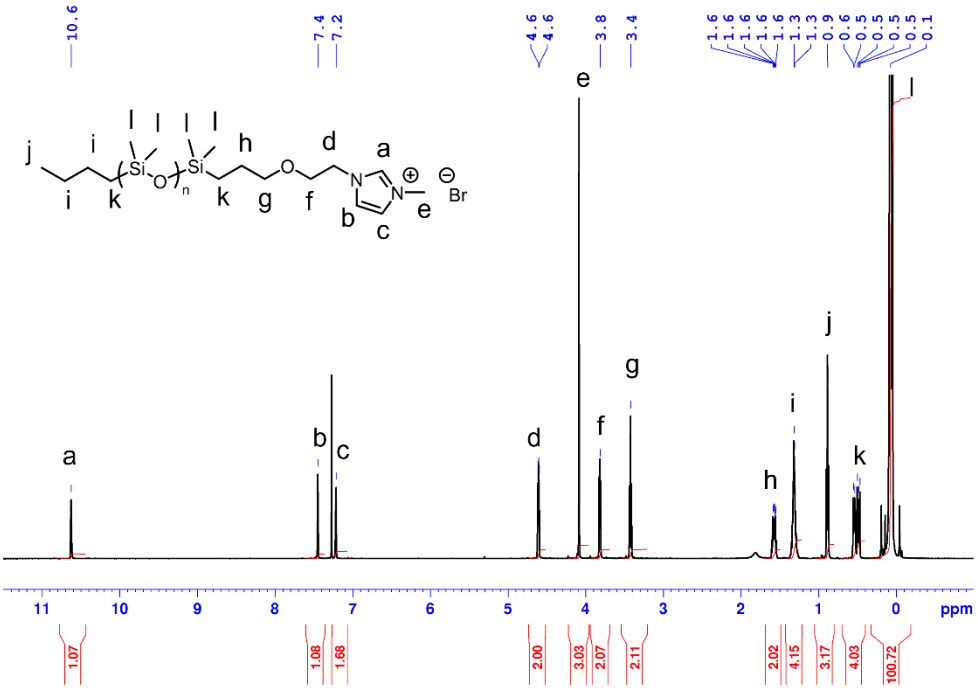

Figure S12 ^{1}H NMR spectrum of oDMS-*MIM*$^{(+)}$*Br*$^{(-)}$.

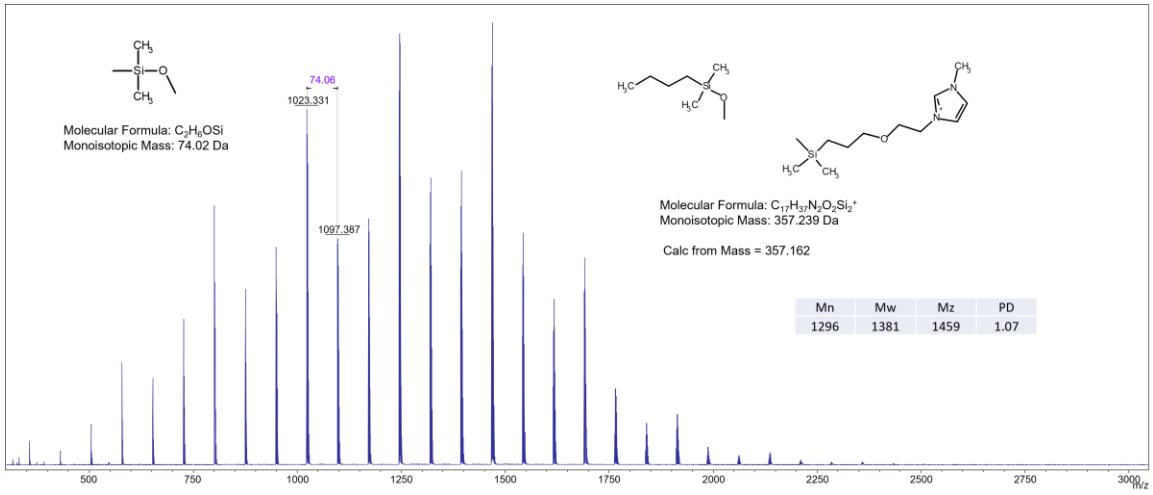

Figure S13 MS spectrum of oDMS-*MIM*$^{(+)}$*Br*$^{(-)}$.

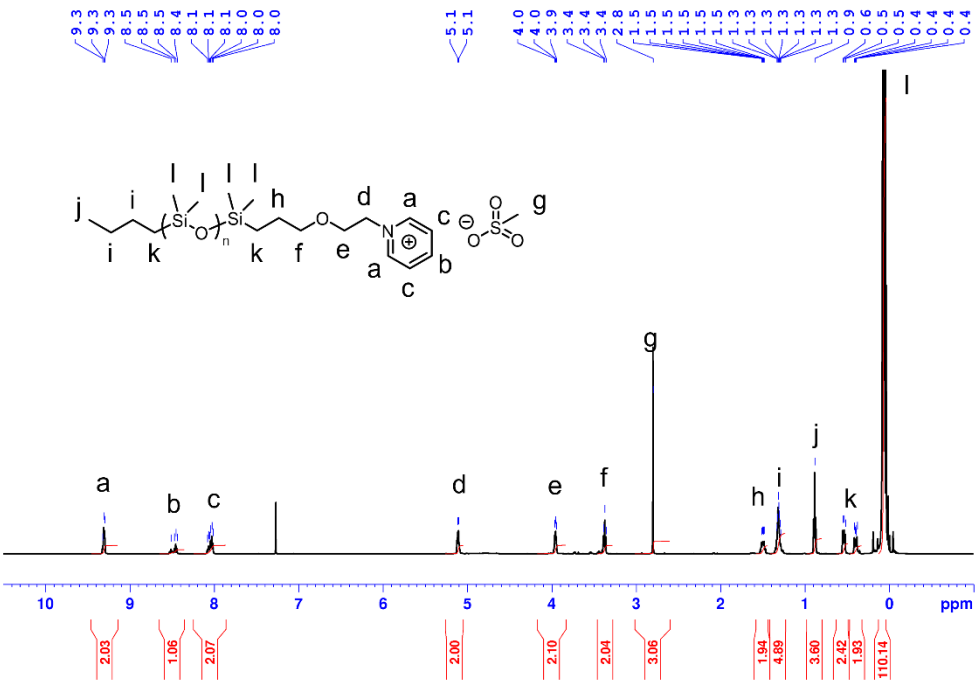

Figure S14 ^{1}H NMR spectrum of oDMS-*Py*$^{(+)}$*OMs*$^{(-)}$.

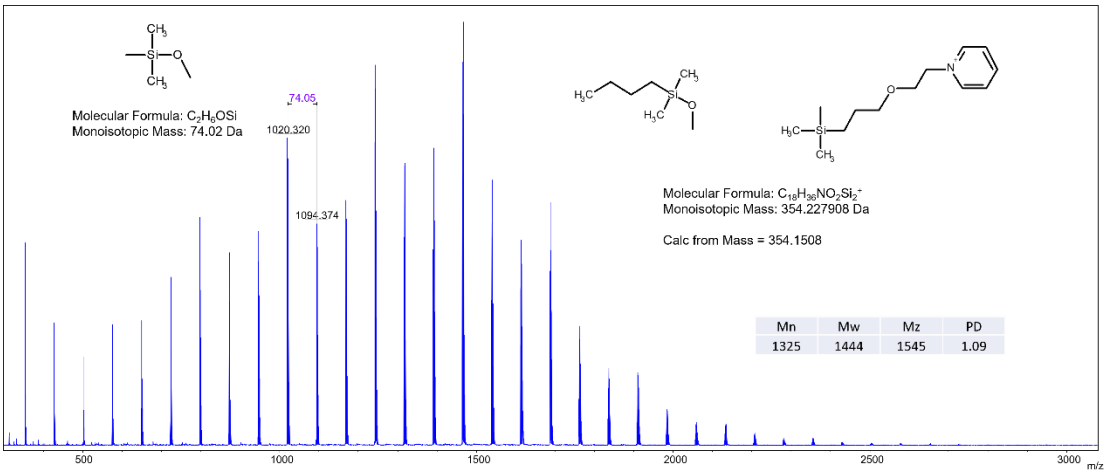

Figure S15 MS spectrum of oDMS-*Py*$^{(+)}$*OMs*$^{(-)}$.

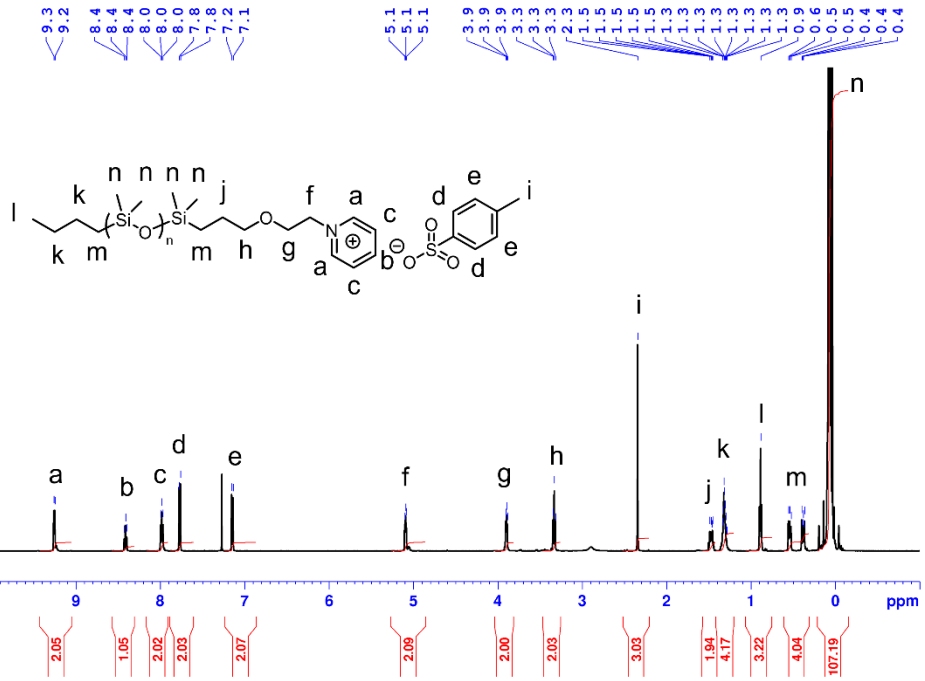

Figure S16 ^{1}H NMR spectrum of oDMS-*Py*$^{(+)}$*OTs*$^{(-)}$.

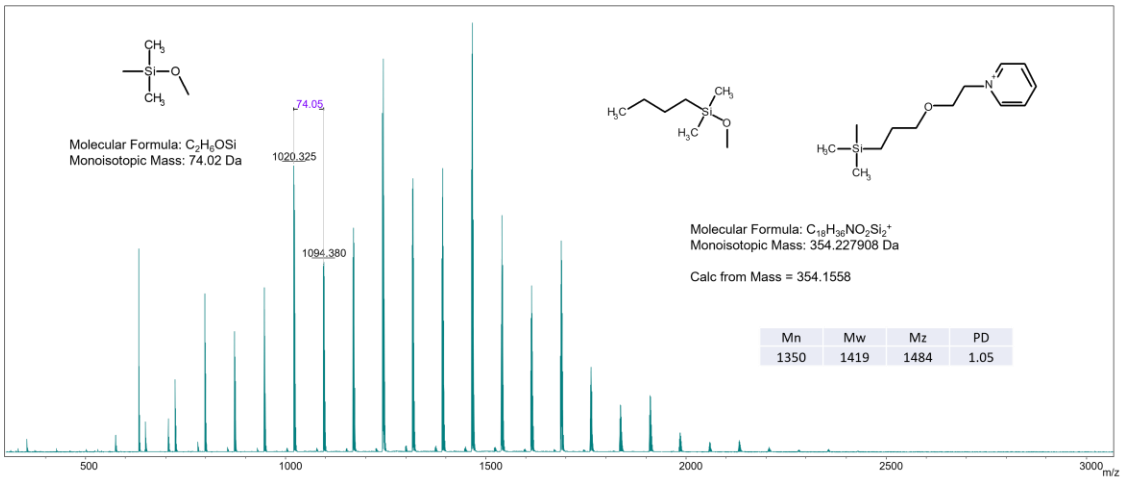

Figure S17 MS spectrum of oDMS-*Py*$^{(+)}$*OTs*$^{(-)}$.

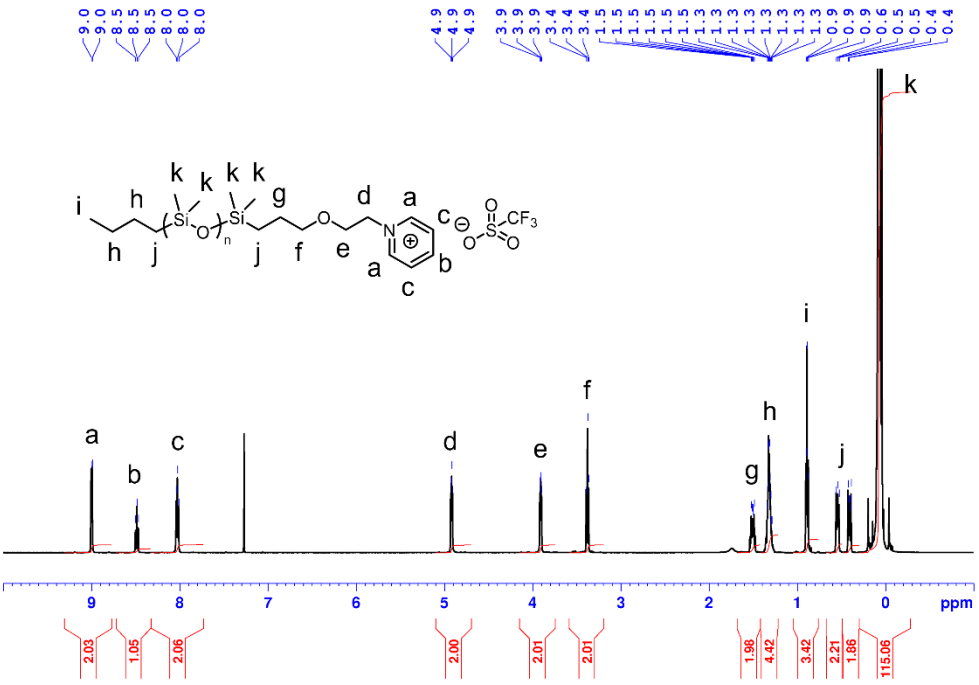

Figure S18 ^{1}H NMR spectrum of oDMS-*Py*$^{(+)}$*OTf*$^{(-)}$.

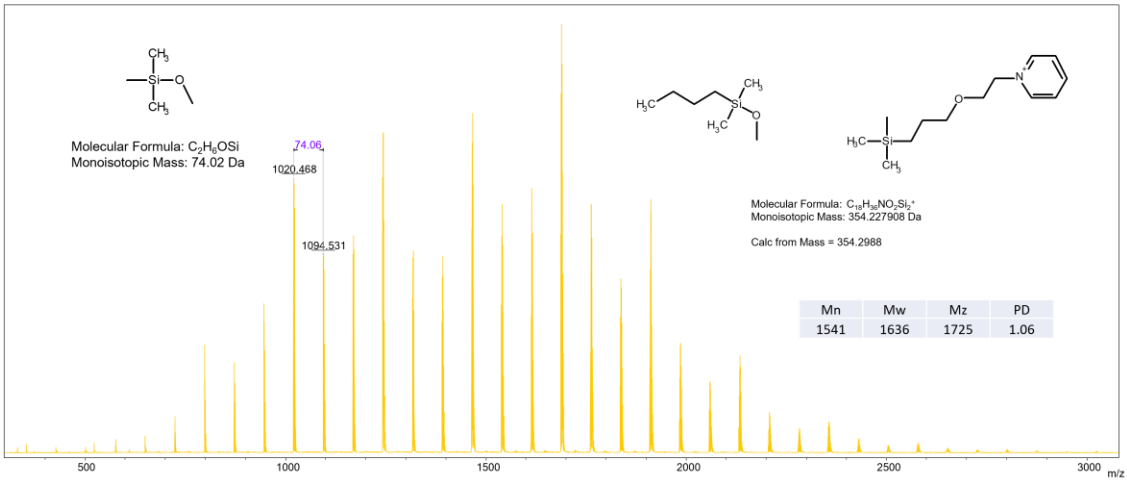

Figure S19 MS spectrum of oDMS-*Py*$^{(+)}$*OTf*$^{(-)}$.

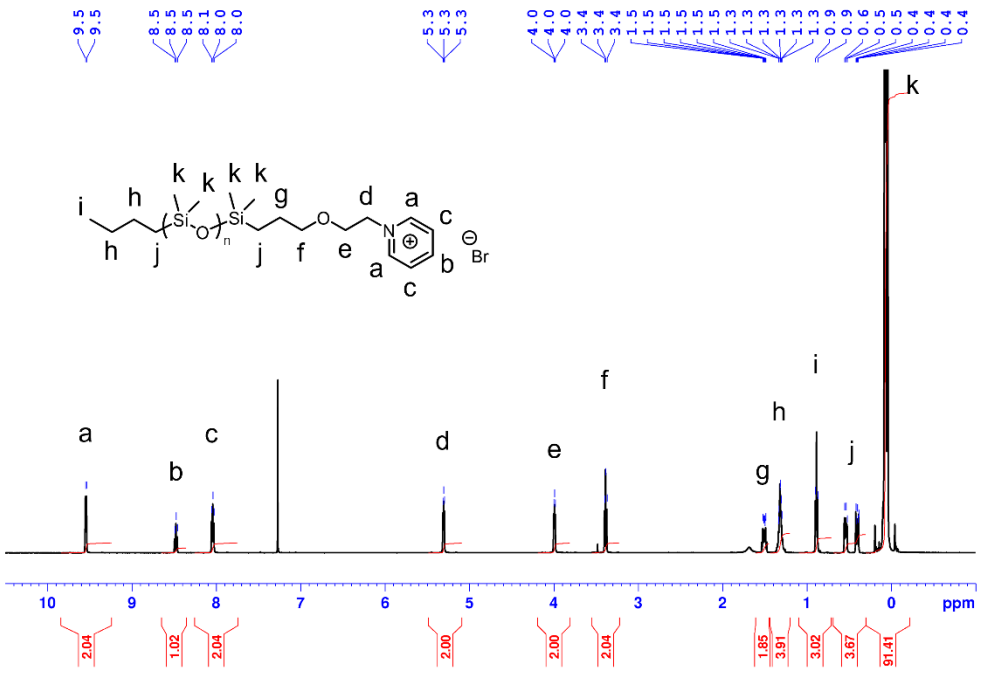

Figure S20 ^{1}H NMR spectrum of oDMS-*Py*$^{(+)}$*Br*$^{(-)}$.

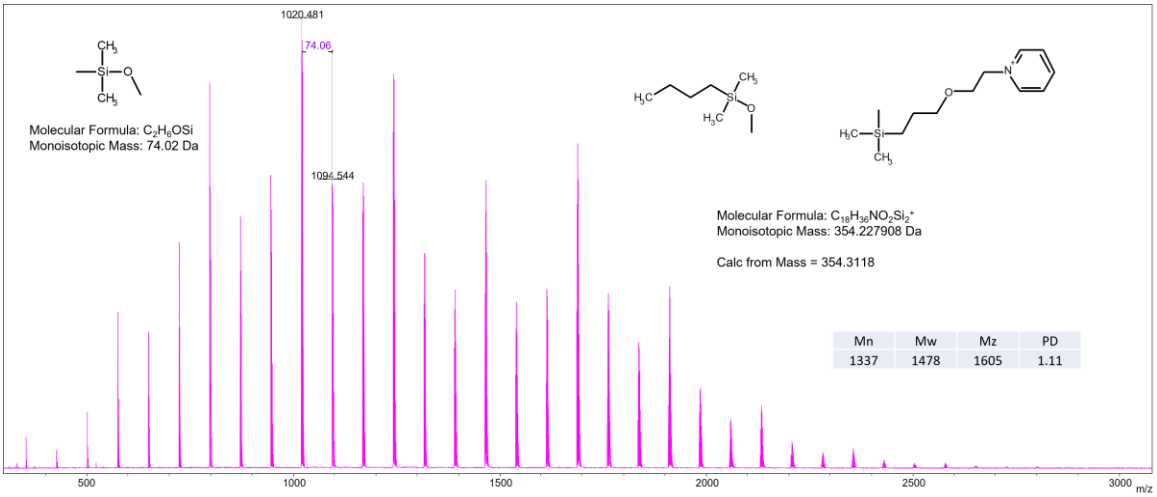

Figure S21 MS spectrum of oDMS-*Py*$^{(+)}$*Br*$^{(-)}$.

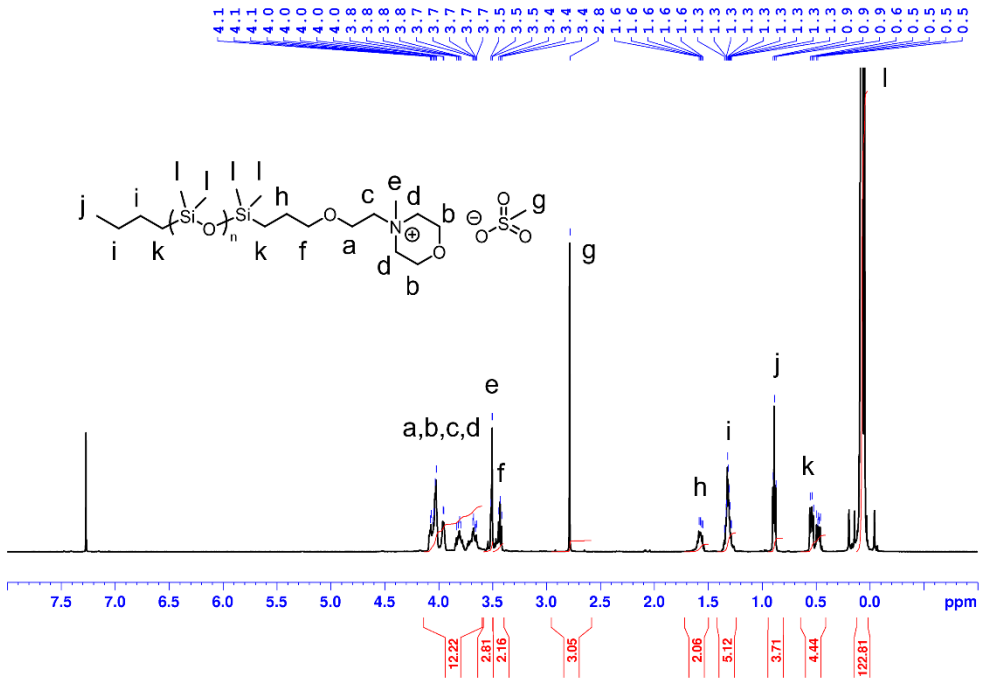

Figure S22 ^{1}H NMR spectrum of oDMS-*MMP*$^{(+)}$*OMs*$^{(-)}$.

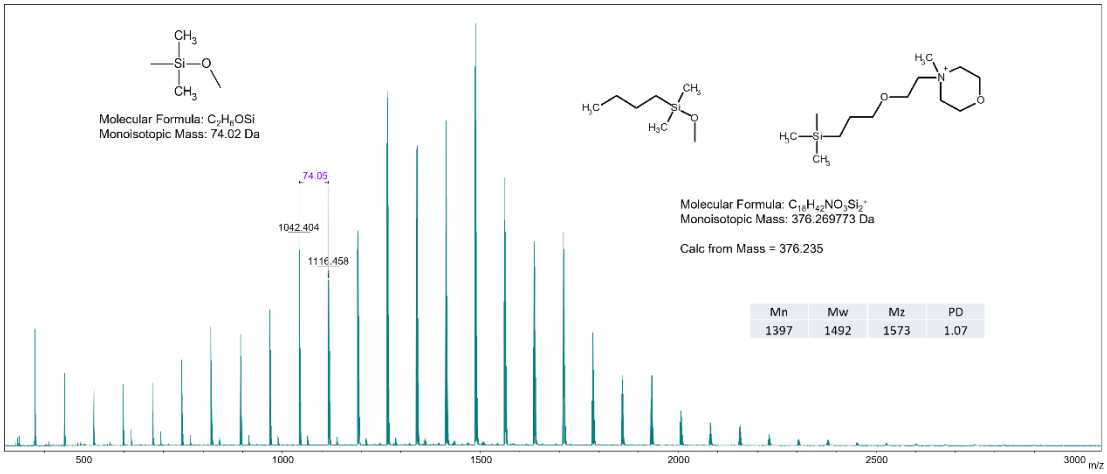

Figure S23 MS spectrum of oDMS-*MMP*$^{(+)}$*OMs*$^{(-)}$.

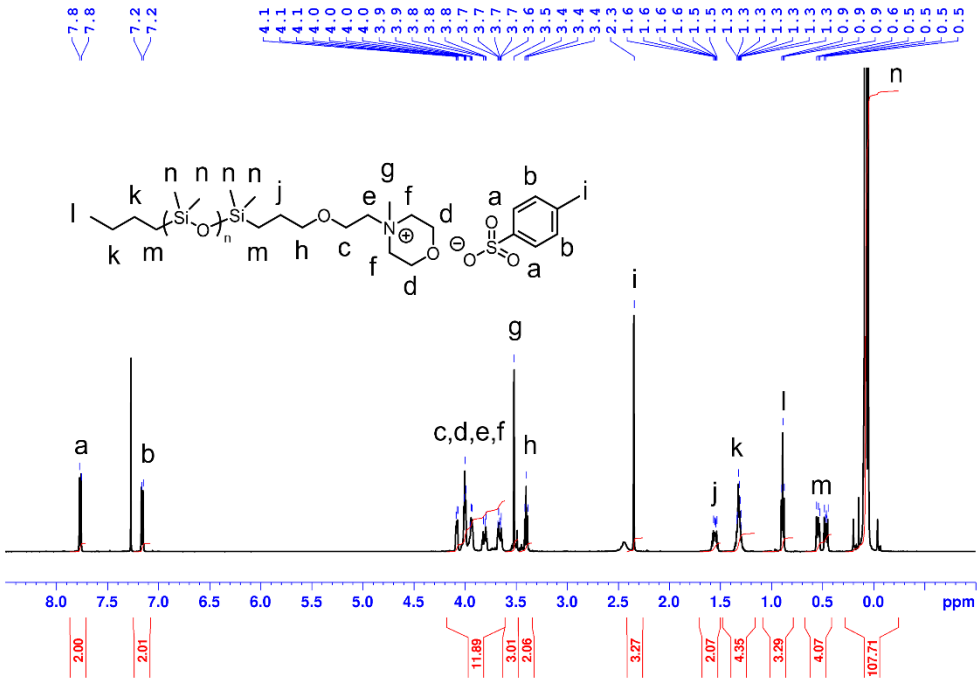

Figure S24 ^{1}H NMR spectrum of oDMS-*MMP*$^{(+)}$*OTs*$^{(-)}$.

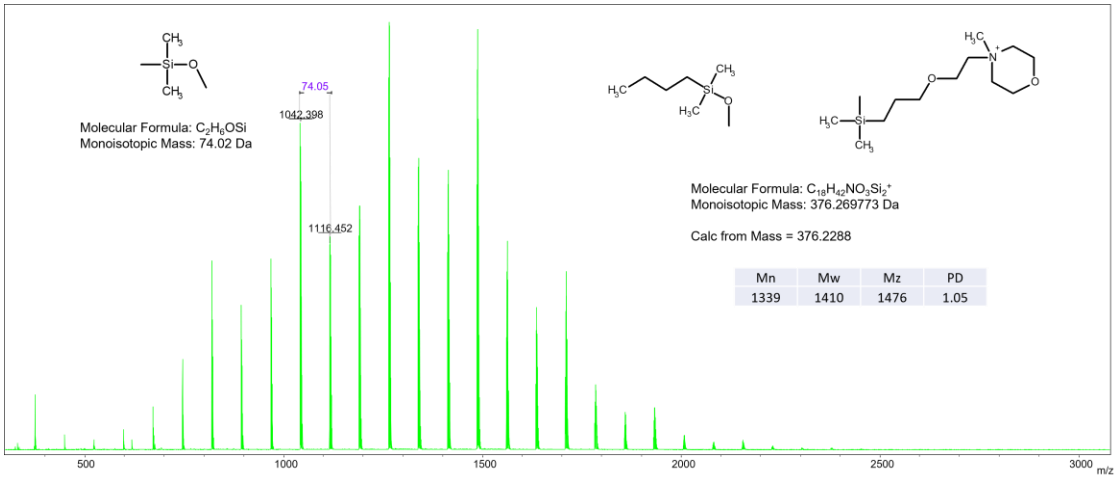

Figure S25 MS spectrum of oDMS-*MMP*$^{(+)}$*OTs*$^{(-)}$.

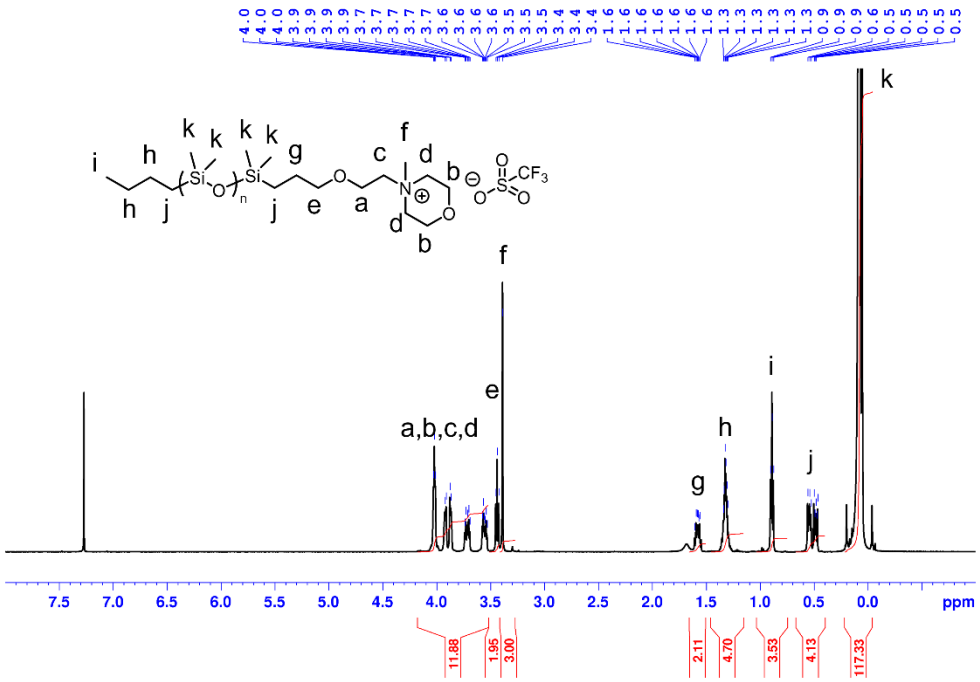

Figure S26 ^{1}H NMR spectrum of oDMS-*MMP*$^{(+)}$*OTf*$^{(-)}$.

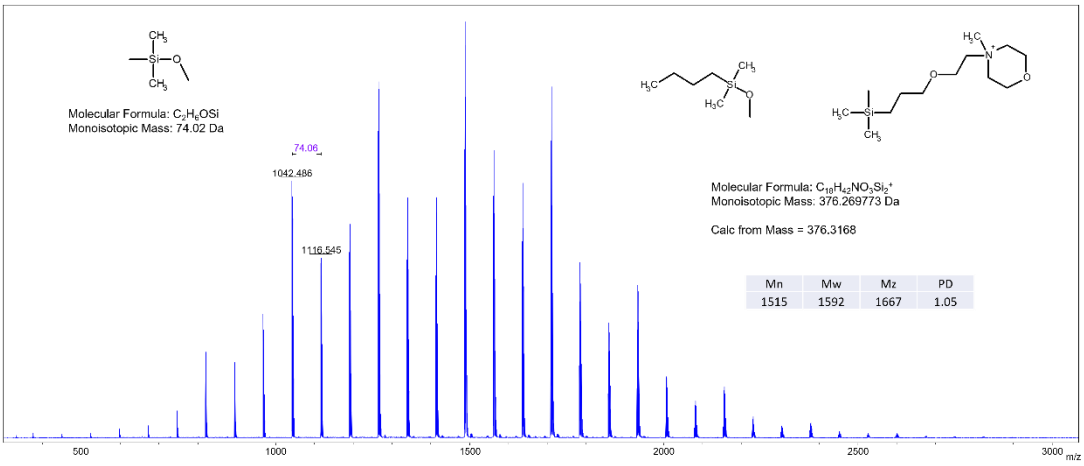

Figure S27 MS spectrum of oDMS-*MMP*$^{(+)}$*OTf*$^{(-)}$.

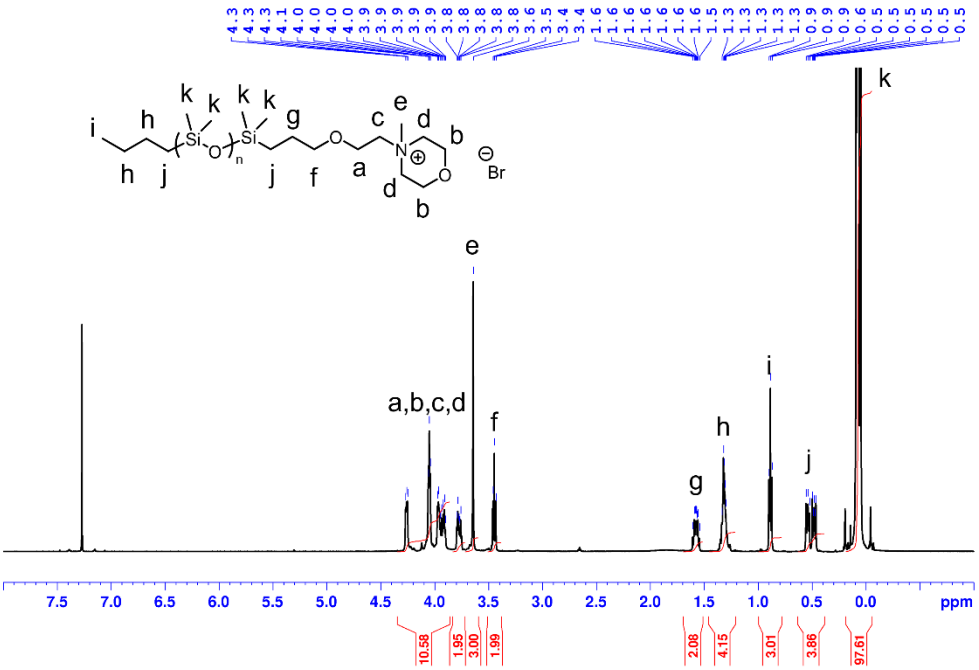

Figure S28 ^{1}H NMR spectrum of oDMS-*MMP*$^{(+)}$*Br*$^{(-)}$.

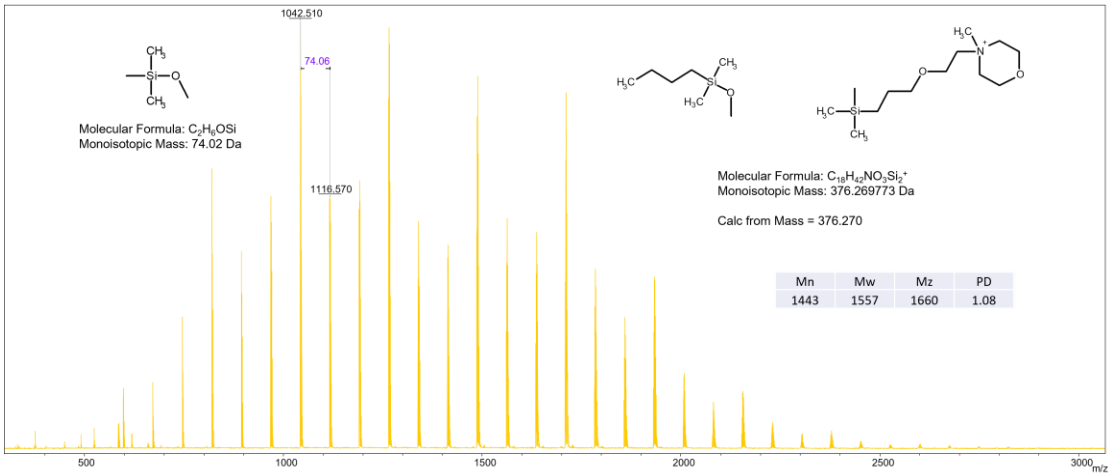

Figure S29 MS spectrum of oDMS-*MMP*$^{(+)}$*Br*$^{(-)}$.

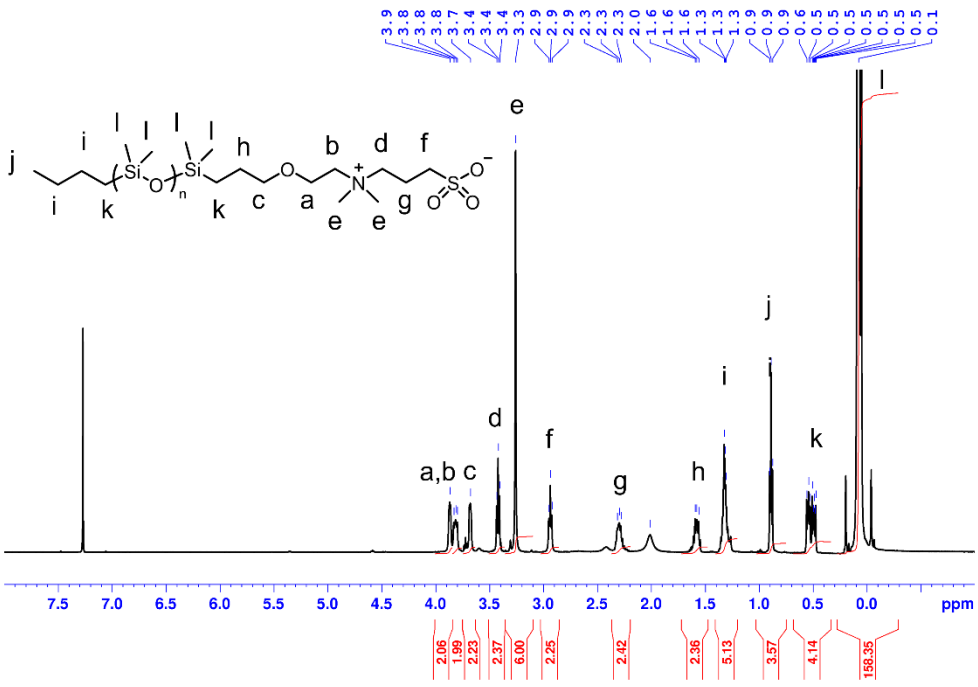

Figure S30 ^{1}H NMR spectrum of oDMS-*N*$(CH_3)_2^{(+)}$-$(CH_2)_3$-$SO_3^{(-)}$.

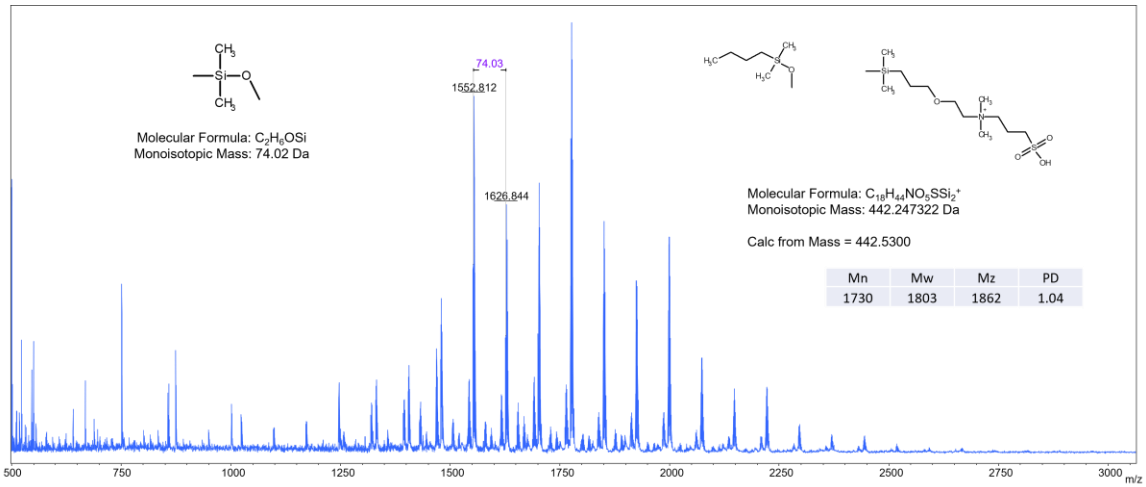

Figure S31 MS spectrum of oDMS-$N(CH_3)_2^{(+)}$-$(CH_2)_3$-$SO_3^{(-)}$.

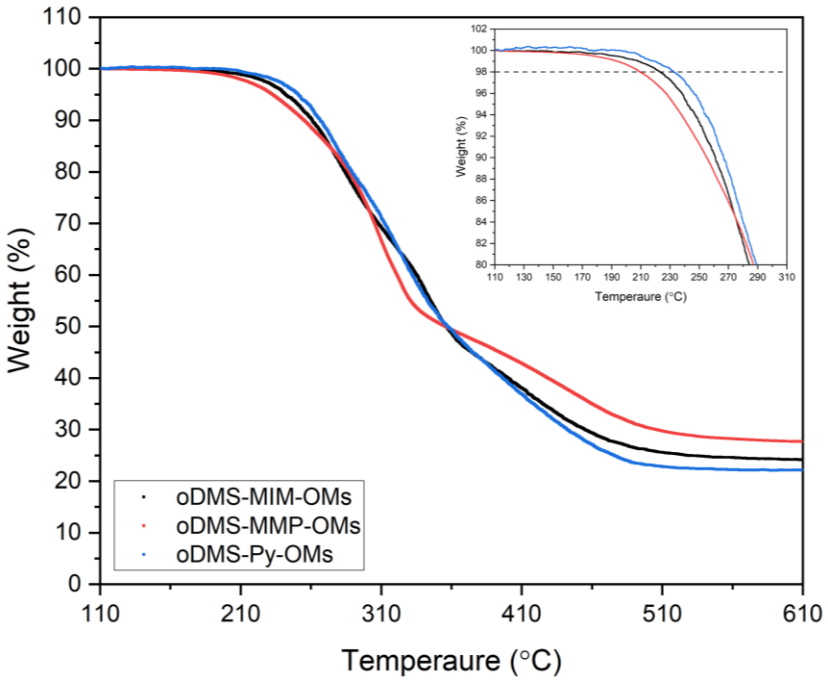

Figure S32 Comparison of TGA curves with anions of $OMs^{(-)}$.

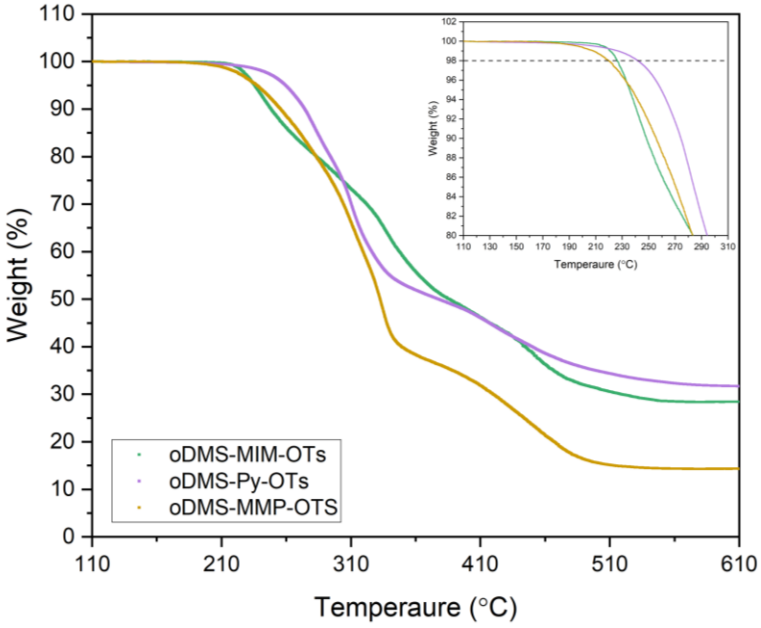

Figure S33 Comparison of TGA curves with anions of $OTs^{(-)}$.

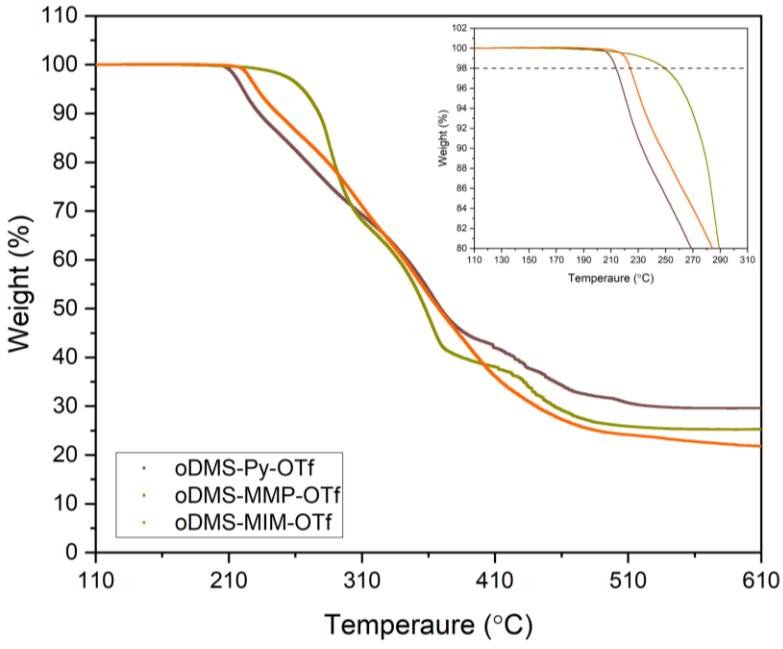

Figure S34 Comparison of TGA curves with anions of $OTf^{(-)}$.

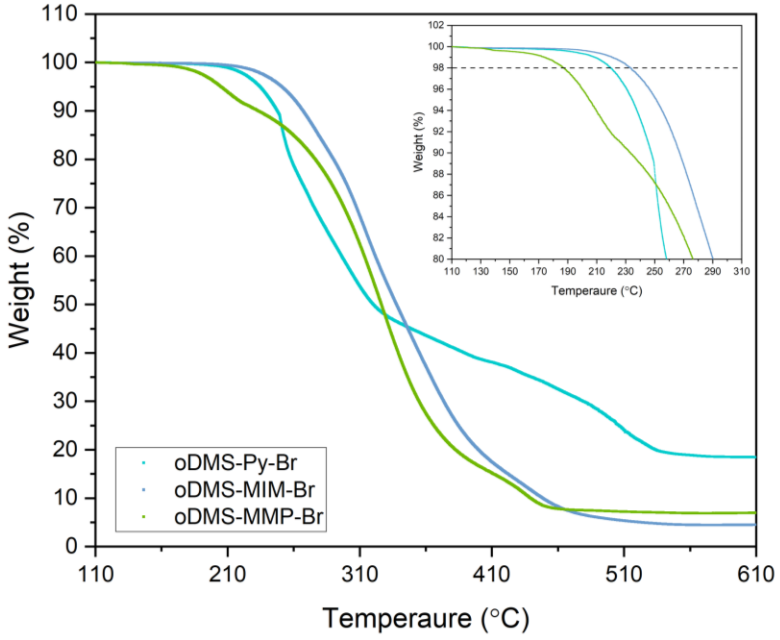

Figure S35 Comparison of TGA curves with anions of $Br^{(-)}$.

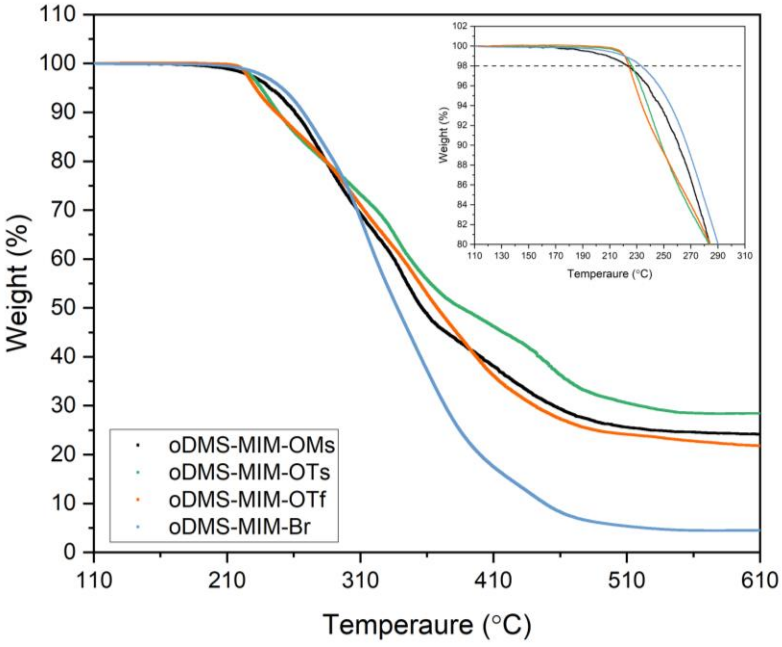

Figure S36 Comparison of TGA curves with cations of $MIM^{(-)}$.

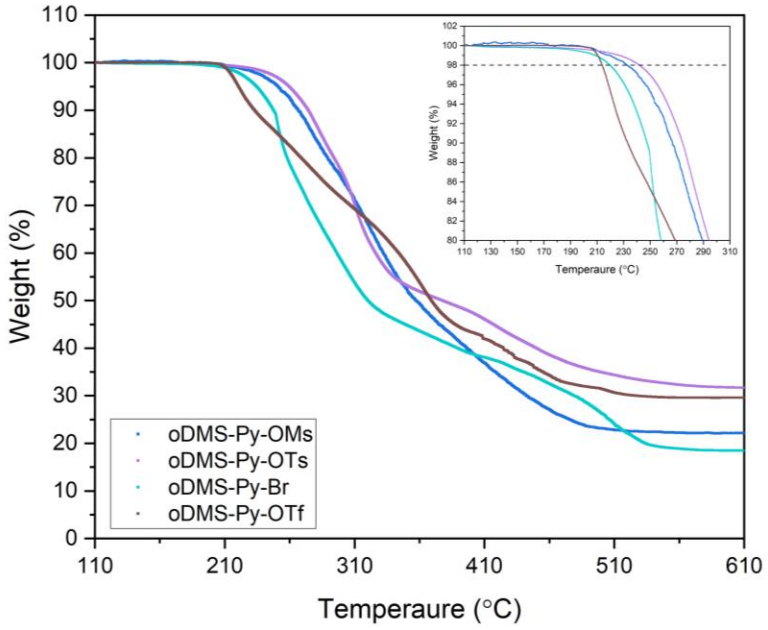

Figure S37 Comparison of TGA curves with cations of $Py^{(-)}$.

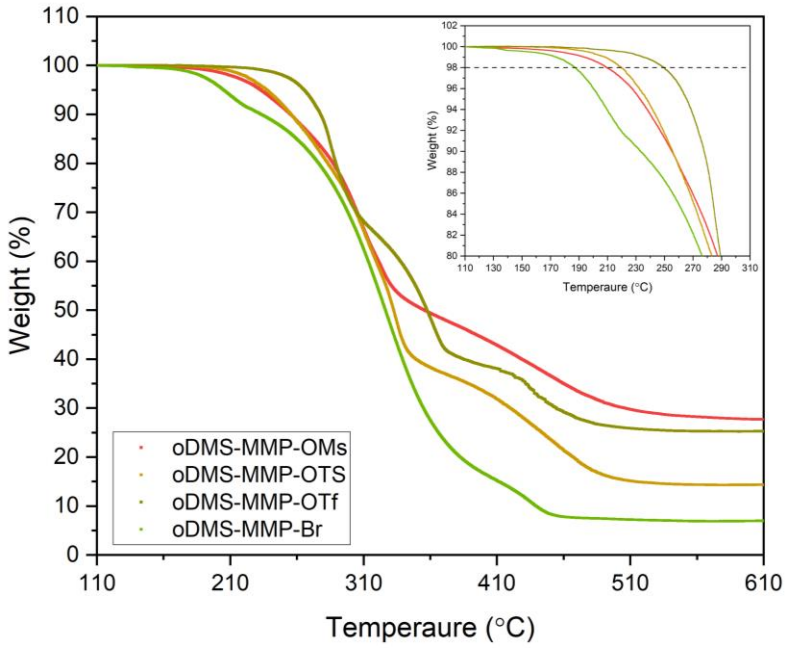

Figure S38 Comparison of TGA curves with cations of $MMP^{(-)}$

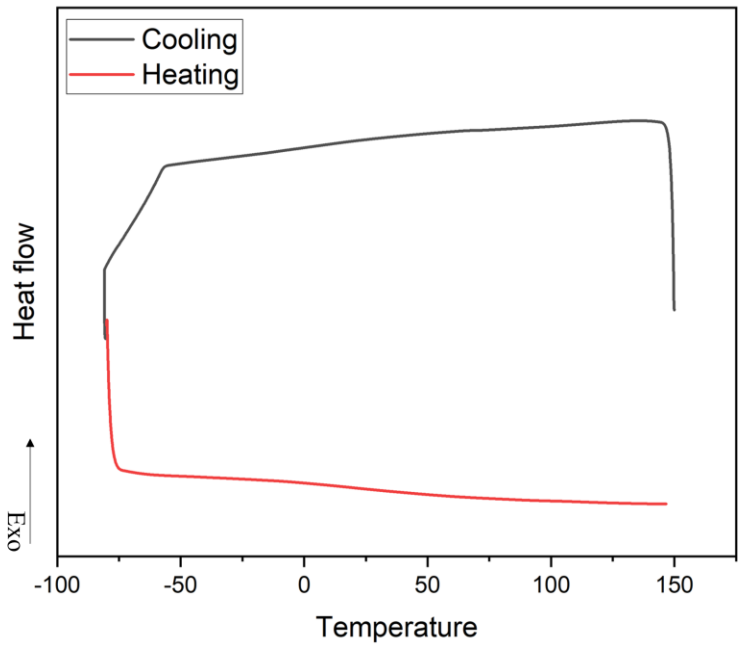

Figure S39 DSC curves of oDMS-*OH* (No peak detected as amorphous material).

VITA

Tianyu Li was born in Gansu, China. He obtained the Bachelor of Engineering Degree in Composite Materials and Engineering in July 2015 from East China University of Science and Technology and the Master of Science Degree in Polymer Science in May 2016 from The University of Akron, joined the research group of Dr. Kunlun Hong in May 2017, and graduated in May 2022 with a Ph.D. Degree in Materials Science and Engineering focused on developing oligodimethylsiloxanes with charged ionic and zwitterion chain ends with unique properties, including tunable thermal stability, sub-10 nm structures with various morphologies and order-disorder transition temperatures, and interfacial structures at the oil/aqueous interface.

During his six years of study and research at the University of Tennessee, Knoxville, he worked on various research projects and user projects in Oak Ridge National Laboratory (ORNL), including lipid-based materials: oligomers with charged chain ends, structure-property relationships in poly(n-alkyl (meth)acrylate)s, selective deuteration of target materials, chain conformations of bottlebrush polymers and conjugated polymers, and synthesis of required materials for users and characterizations of materials with different techniques for users. He published one first-authored paper and thirteen co-authored papers. He presented his research on different occasions, including one ACS national meeting and two user meetings of Center for Nanophase Materials Sciences in ORNL.